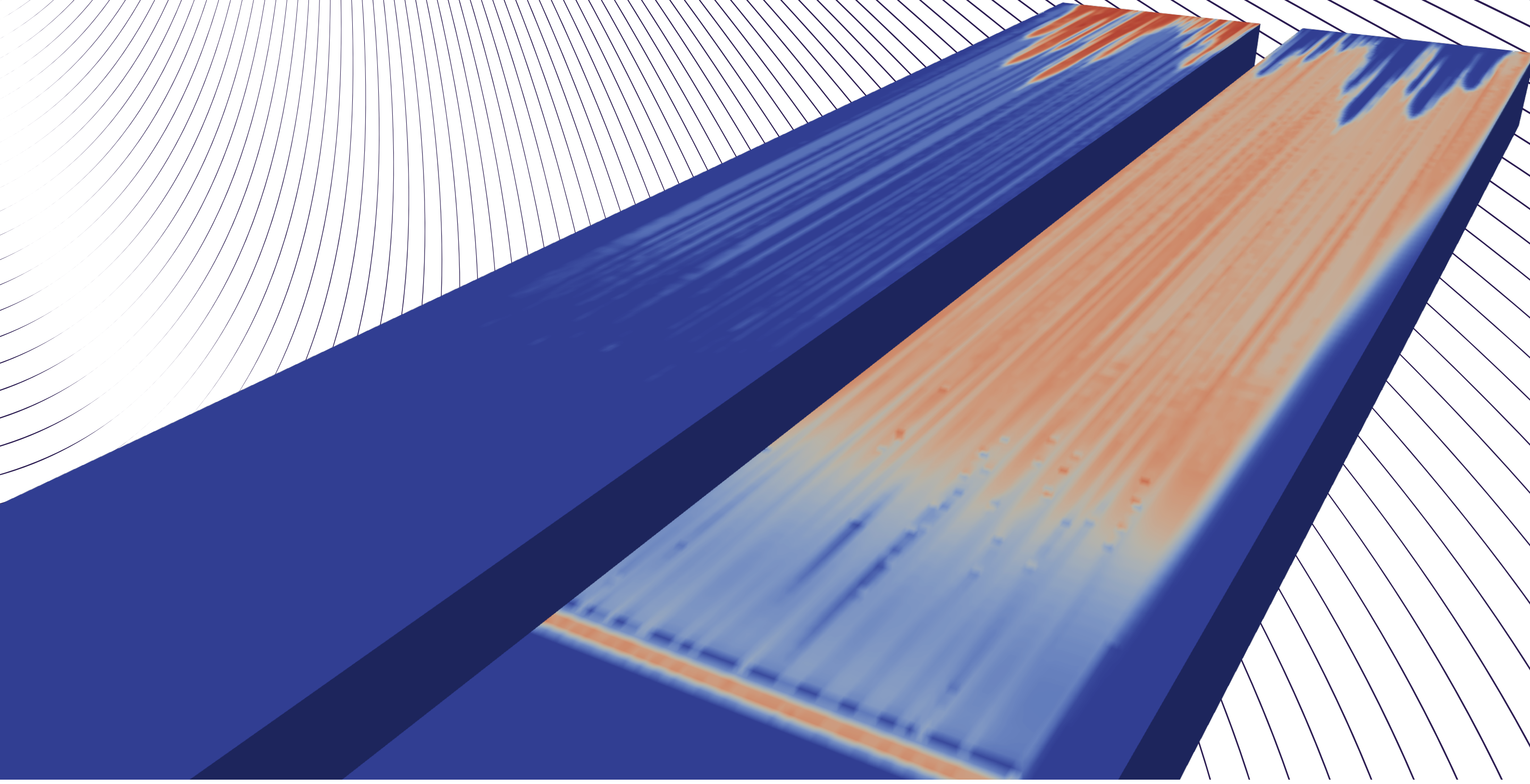

Numerical Modelling of Air-Induced Drag Reduction for Marine Vessels with a Multifield Two-Fluid Model

Christian Kringel & Victor Hvass Mølbak

Thermal Energy and Process Engineering, TEPE4-1009a, 2024-05
Master's Thesis

STUDENT REPORT
AALBORG UNIVERSITY

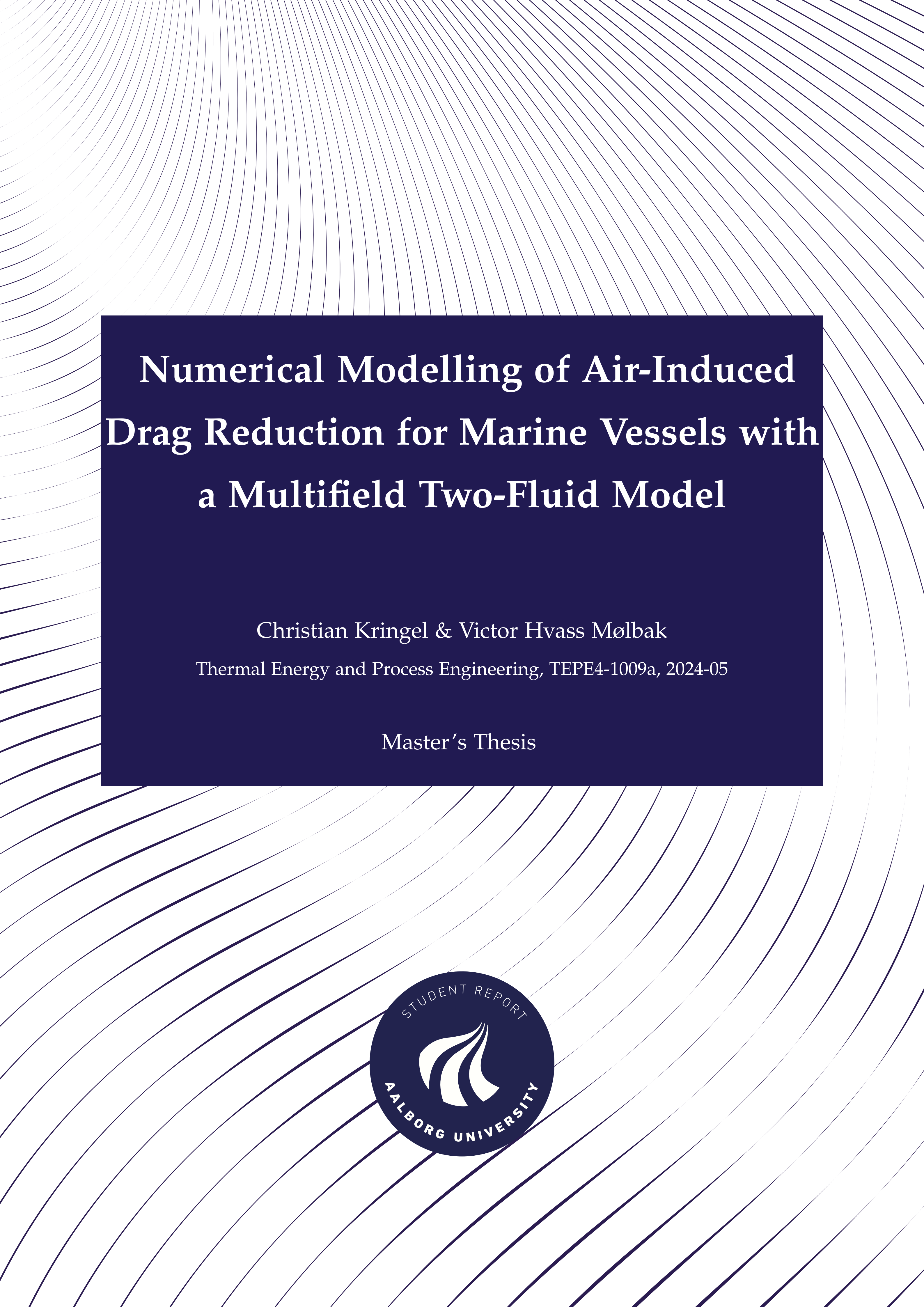

Numerical Modelling of Air-Induced Drag Reduction for Marine Vessels with a Multifield Two-Fluid Model

Christian Kringel & Victor Hvass Mølbak

Thermal Energy and Process Engineering, TEPE4-1009a, 2024-05

Master's Thesis

STUDENT REPORT
AALBORG UNIVERSITY

This thesis is written in LaTeX. Numerical simulations are performed in the open-source CFD tools OpenFOAM.com version 2312 and OpenFOAM.org version 11. Paraview and Python are used to analyse and post-process numerical results.

AAU Energy
Aalborg University
http://www.aau.dk

AALBORG UNIVERSITY
STUDENT REPORT

Title:
Numerical Modelling of Air-Induced Drag Reduction for Marine Vessels with a Multifield Two-Fluid Model

Theme:
Master's Thesis

Project Period:
Spring Semester 2024

Project Group:
TEPE4-1009a

Participants:
Christian Kringel
Victor Hvass Mølbak

Supervisor:
Jakob Hærvig

Page Numbers: 84

Date of Completion:
May 30, 2024

Abstract:

With the increasing focus in recent years on limiting fossil fuel usage in the maritime industry, many new and innovative technologies have emerged to decrease pollution and fuel cost. One of these technologies is air lubrication, which aims to reduce frictional resistance between the ship hull and the water. This thesis analyses how the multifield two-fluid framework, MultiMorph, can be used to model the air lubrication phenomenon. The MultiMorph model is studied and validated upon a two-dimensional domain, finding that the model is accurately able to capture the various air lubrication regimes, observed by the experimental studies. Further analysis was done on how multiple air injectors would impact the bubbly air layer, concluding that a sustained continuous air layer, with a drag reduction of roughly 90%, is possible with a small enough injector spacing. A more in-depth Volume of Fluid large eddy simulation is done on a domain around the air injector, where it was found that the air bubbles are generated as a slug-like structure with a diameter in the range of 1 mm to 3 mm. This study also observed that the air slugs did not come into contact with the above surface, instead a thin water layer was present between the slugs and the near wall, which was not captured in the MultiMorph framework.

Preface

This master's thesis project, written in collaboration with Alfa Laval Aalborg, is written in the 4th semester of the master program *Thermal Energy and Process Engineering* at Aalborg University at the Faculty of Engineering and Science. The thesis is written from the 1st of February to the 31st of May 2024.

Reading Instructions

Throughout the project, relevant literature is referenced with the Harvard method where the source is listed in the text as (Author Year). For multiple authors, (Author et.al Year) is used. A list of references is placed at the end of the report.

Tables, equations and figures are numbered according to the chapter and section they appear in. In this way, the first figure in Chapter 5 has the number 5.1 the next is 5.2, etc. Explanatory text is given in captions above tables and below figures. References to the appendix are addressed with letters.

The appendix located at the end of the report is denoted Appendix A. The appendix contains information relevant to the report, and references to the different parts of the appendix are made throughout the report.

In equations, vectors are indicated in bold and italic as $\boldsymbol{u}$, for example. Square parentheses, $\langle u \rangle$ and overlines, $\overline{u}$ denote time-averaged and space-averaged values, respectively.

Acknowledgements

The authors would like to thank supervisor Jakob Hærvig of Aalborg University and collaborator Kasper Gram Bilde of Alfa Laval Aalborg for their helpful guidance and discussion throughout the project period.
Additionally, we would like to thank Alfa Laval Aalborg for providing facilities and workstations allowing for close collaboration and knowledge-sharing.

Victor

Christian Kringel
<ckring19@student.aau.dk>

Victor Hvass Mølbak
<vmalba19@student.aau.dk>

Summary

To comply with global climate goals, steps must be taken to reduce greenhouse gas emissions in all sectors. An area of great potential is the maritime sector, which has seen a 20% yearly increase in emissions. A promising technology for improving energy efficiency in maritime transport is air lubrication on ship hulls, which aims to reduce frictional resistance.

The challenge in modelling air lubrication is that air bubbles in the order of mm to μm are to be resolved under ship hulls in the order of 200-400 m resulting in exponentially increasing computational time. In this thesis, the adaptive multifield two-fluid model MultiMorph is used. The adaptive model works, by switching between an Euler-Euler (E-E) and a Volume of Fluid (VOF) model based on grid refinement and air concentration, greatly reducing computational time. The modelling strategy is presented in Figure 1.

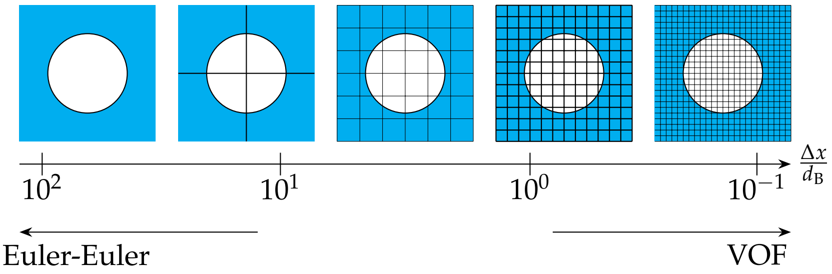

Figure 1: Modelling strategy of the MultiMorph model for an arbitrary bubble. Bubbles smaller than grid-scale are modelled with E-E and bubbles larger than grid-scale are resolved with the VOF model.

The MultiMorph model solves the phase-averaged Navier-Stokes equations. The mass and momentum conservation equations for a phase r are given as

$$\frac{\partial \alpha_\mathrm{r}\rho_\mathrm{r}}{\partial t} + \nabla \cdot (\boldsymbol{u}_\mathrm{r}\alpha_\mathrm{r}\rho_\mathrm{r}) = \Gamma_\mathrm{r} \tag{1}$$

$$\frac{\partial(\alpha_\mathrm{r}\rho_\mathrm{r}\boldsymbol{u}_\mathrm{r})}{\partial t} + \nabla \cdot (\alpha_\mathrm{r}\rho_\mathrm{r}\boldsymbol{u}_\mathrm{r}\boldsymbol{u}_\mathrm{r}) = \nabla \cdot (2\alpha_\mathrm{r}\mu_\mathrm{r}\boldsymbol{S}_\mathrm{r}) - \alpha_\mathrm{r}\nabla p + \alpha_\mathrm{r}\rho_\mathrm{r}\boldsymbol{g} + \boldsymbol{f}_\mathrm{r} + \boldsymbol{\Gamma}^*_\mathrm{r} \tag{2}$$

The MultiMorph model is validated with experimental data of Elbing et al. (2008) who conducted various air lubrication experiments on a flat plate. As the three-dimensional effects are expected to be negligible in the experiment, the computational model is simplified as a two-dimensional plate, upon which the validation is done. A comparison between the drag reduction along the plate for the model and experimental data is shown in Figure 2.

Figure 2 implies that the MultiMorph model can accurately predict the air-induced drag reduction in air lubrication.

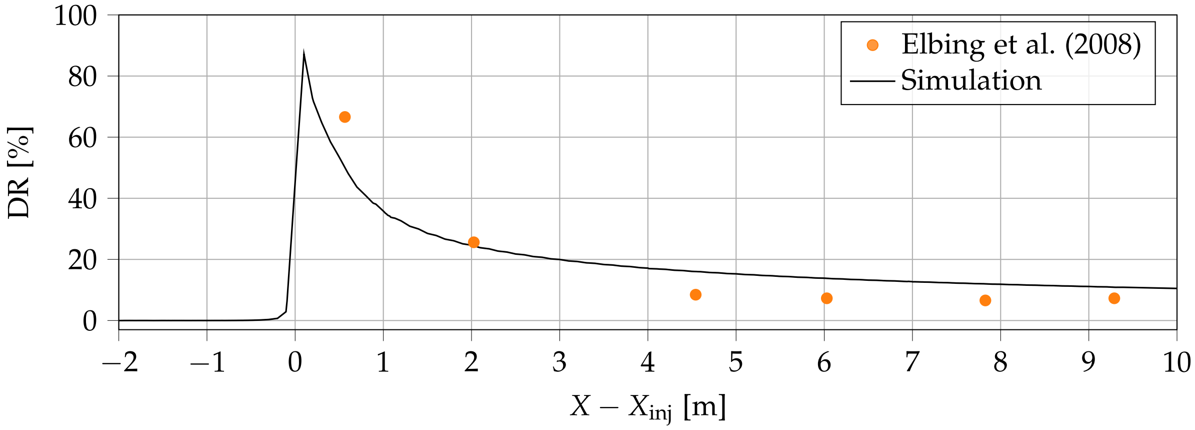

Figure 2: Comparison of drag reduction along the plate for the MultiMorph model, and experimental data of Elbing et al. (2008).

To analyse the dissipation of the air layer, an analysis is done where an additional air injector is implemented at 2 m, 4 m and 6 m downstream of the first injector. Figure 3 presents the results of the additional injector implemented at $X - X_{\text{inj}} = 2\,\text{m}$. The figure shows, that as the second injector is implemented, a continuous air layer forms, as the continuous air volume fraction increases drastically. This results in a greatly increased, and constant, drag reduction. The analysis also showed, that injectors implemented further downstream than $X - X_{\text{inj}} = 2\,\text{m}$ would not form a continuous air layer and the drag reduction would reduce rapidly.

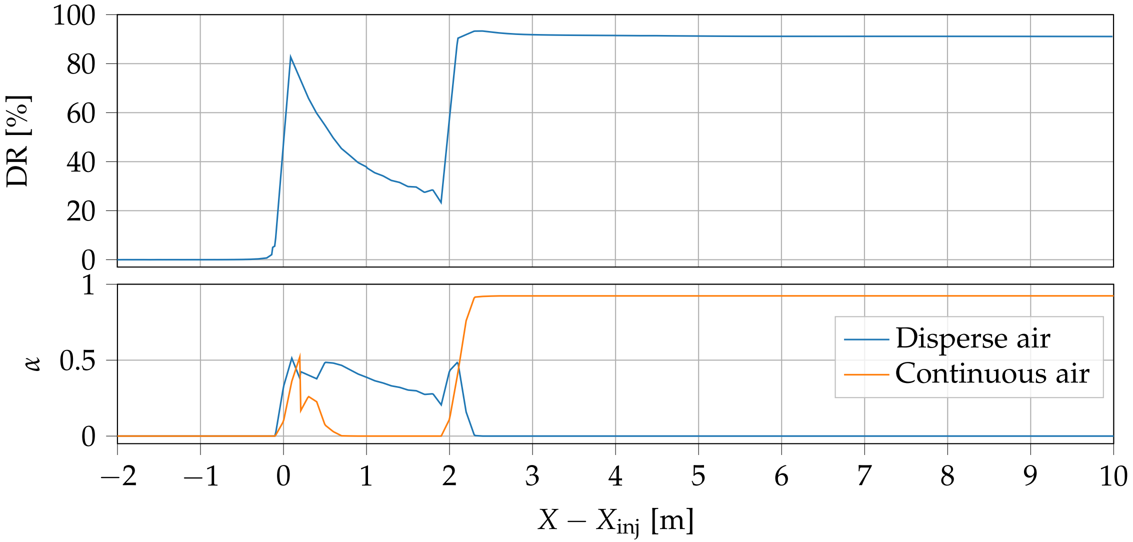

Figure 3: Drag reduction and air volume fraction versus downstream distance of the first injector location. A second air injector is implemented at $X - X_{\text{inj}} = 2\,\text{m}$.

In all previous analyses, the plate was assumed to be perfectly smooth. An analysis is thereby done, where surface roughness is compared with the results of a smooth wall. The analysis showed, that a surface roughness of just $R_{\text{a}} = 100\ \mu\text{m}$ resulted in roughly 4%pt. less drag reduction compared with the smooth wall. This is because the surface roughness induces more turbulence in the near-wall region, increasing air transportation away from the wall. Therefore, surface roughness is an important parameter, when modelling air lubrication for real-world applications.

Abbreviations and Subscripts

Abbreviation	**Definition**
ALDR	Air layer drag reduction
BDR	Bubble drag reduction
BIT	Bubble-induced turbulence
CFD	Computational fluid dynamics
CSF	Continuum surface force
DFSEM	Divergence free synthetic eddie method
DNS	Direct numerical simulation
DR	Drag reduction
IMO	International Maritime Organisation
LES	Large eddy simulation
PCDR	Partial cavity drag reduction
PLIC	Piecewise linear interface calculations
RANS	Reynolds-averaged Navier-Stokes
SST	Shear stress transport
TD	Turbulent dispersion
URANS	Unsteady Reynolds-averaged Navier-Stokes
VOF	Volume of fluid

Subscripts	**Definition**
g	Gas
i	i'th entry
l	Liquid
r	Phase
x	x-direction
y	y-direction
z	z-direction

Nomenclature

Symbol	Definition	Unit
A	Surface area	m^2
A_I	Interface indicater field	-
B	Log-law constant	-
B_{11}^norm	Normalised two-point correlation	-
C	Closure model coefficient	-
C_f	Filter diffusion term	-
C_s	Roughness constant	-
C_μ	k-ω SST model coefficient	-
Co	CFL number	-
d_B	Bubble diameter	m
D	Diameter	m
Eo	Eötvös number	-
$\mathrm{Eo}_\perp$	Modified Eötvös number	-
f_r	Interfacial momentum exchange	$\mathrm{kg \cdot m/s^2}$
$\boldsymbol{F}$	Force	$\mathrm{kg \cdot m/s^2}$
g	Gravitational acceleration	$\mathrm{m/s^2}$
h	Cell width	m
I	Turbulence intensity	%
k	Turbulence kinetic energy	$\mathrm{m^2/s^2}$
K	Coefficient	-
l	Characteristic length scale	m
L	Length	m
$\hat{\boldsymbol{n}}$	Interface normal vector	-
p	Pressure	$\mathrm{kg/(m \cdot s^2)}$
q	Flow rate	$\mathrm{m^2/s}$
r_0	Initial bubble radius	m
R_am	Arithmetic mean roughness	m
R_z	Peak-to-valley roughness	m
Re	Reynolds number	-
S	Source term	-
Sr	Dimensionless shear rate	-
t	Time	s
t^*	Dimensionless time	-
$\boldsymbol{T}$	Stress tensor	-
u	Velocity	m/s
u_g	Gravitational velocity	m/s
u_I	Interfacial velocity	m/s
u_t	Bubble terminal velocity	m/s
u_∞	Free-stream velocity	m/s
u^+	Dimensionless velocity	-
u_τ	Frictional velocity	m/s
V	Volume	m^3
X_inj	Location of air injector	m
y	Wall distance	m

$\hat{y}$	Wall normal vector	-
y^+	Dimensionless wall distance	-
α	Volume fraction	-
β	k-ω SST model coefficient	-
β	Contact angle	$\circ$
γ	Shear rate	$1/\mathrm{s}$
γ^*	Correction function	-
Γ	Interfacial mass exchange	$\mathrm{kg} \cdot \mathrm{s}/\mathrm{m}^3$
δ	Boundary layer thickness	m
δ_r	Damping length scale	-
ϵ	Sand-grain roughness	m
ζ	Under-resolution indicator	-
κ	von Kármán constant	-
κ_I	Interface curvature	-
μ	Dynamic viscosity	$\mathrm{kg}/(\mathrm{m} \cdot \mathrm{s})$
μ^T	Eddy viscosity	$\mathrm{kg}/(\mathrm{m} \cdot \mathrm{s})$
ν	Kinematic viscosity	kg^2/s
ρ	Density	kg/m^3
σ	Surface tension	kg/s^2
σ_f	Filter parameter	-
σ_TD	Turbulent Prandtl number	-
τ	Timescale	s
τ_r	Relaxation time	s
τ_w	Wall shear stress	$\mathrm{kg}/(\mathrm{m} \cdot \mathrm{s}^2)$
ω	Specific turbulence dissipation	$1/\mathrm{s}$

Table of Contents

1 Introduction 1
- 1.1 Air Lubrication . . . 1

2 Modelling of Multiphase Flows 4
- 2.1 Discrete Phase Model . . . 4
- 2.2 Phasic Volume Models . . . 5
- 2.3 Hybrid Multi-Fluid Adaptive Models . . . 7

3 Problem Statement 10
- 3.1 Overview of the Report . . . 10

4 Fluid Dynamics Theory 12
- 4.1 Boundary Layer . . . 12
- 4.2 Wall Shear Stress . . . 16
- 4.3 Surface Roughness Modelling . . . 18

5 System Description 20

6 Numerical Approach 21
- 6.1 Governing Equations . . . 22
- 6.2 Dispersed Mode . . . 23
- 6.3 Resolved Mode . . . 32
- 6.4 Transition Region Methodology . . . 34
- 6.5 Numerical Model Setup . . . 36

7 Validation of MultiMorph Model on a Two-Dimensional Plate 38
- 7.1 Experimental Study by Elbing et al. (2008) . . . 38
- 7.2 Model Parameters for Sensitivity Study . . . 40
- 7.3 Sensitivity Study of Air Slot Injector . . . 43
- 7.4 Sensitivity Study of Mass Source Air Injection . . . 44
- 7.5 Concluding Remarks of Sensitivity Study . . . 46
- 7.6 Validation of Two-Dimensional MultiMorph Model . . . 46

8 Analysis of Air Lubrication Under Varying Conditions 50
- 8.1 Analysis of Boundary Layer in the BDR and ALDR Regimes . . . 50
- 8.2 Surface Roughness . . . 53
- 8.3 Additional Air Injectors . . . 56

9 Numerical Modelling of Air Lubrication with VOF LES 59
- 9.1 Geometry and Computational Domain . . . 59
- 9.2 Numerical Method . . . 60
- 9.3 Results and Discussion . . . 63

10 Conclusion 69

References **71**

A Appendix **79**
A.1 Two-Dimensional Bubble Dynamics Using the MultiMorph Model 79
A.2 MultiMorph Numerical Settings 81
A.3 Experimental Setup for Validation 83
A.4 VOF LES Two-Point Correlation 83
A.5 Boundary Conditions for VOF LES Model 84

1 Introduction

In 2015 the Paris Agreement was adopted by over 190 countries during the COP21 in Paris, France. The overarching goal of the agreement is to keep the global increase in temperature well below 2°C compared to pre-industrial levels. Although world leaders have, in recent years, proclaimed that the aim should be to limit temperature increase of no more than 1.5°C. As a result, the global greenhouse gas emission must peak in 2025 and be reduced by at least 43% by 2030 (Nations 2016).

The transport sector has a large potential for reducing greenhouse gas emissions, as it accounts for 30% of all emissions globally. Among these, is the maritime sector, which has seen a 20% increase in annual emissions in the last decade, resulting in the sector accounting for 3% of global emissions annually (UNCTAD 2023). Although the maritime industry is excluded from the Paris Agreement, the UN's International Maritime Organisation (IMO) has agreed on similar goals for reducing greenhouse gas emissions with participating countries (Fenhann 2017). To reach the goals, much research has gone into the possibility of decarbonization of the industry by using alternative green fuels such as ammonia or methanol. However, the technology and adoption are still in the early stages, with 98.8% of ships sailing on fossil fuels. Estimations show that decarbonization of the sector could result in doubling yearly fuel costs by 2050, presenting further challenges (UNCTAD 2023). Alternative solutions for reducing emissions in the industry are therefore of interest. To comply with existing regulations by IMO, Fenhann (2017) suggests various solutions such as slow steaming, delaying ship-building, new ship designs or solar cells, kites or batteries. Another possibility is air lubrication, where the frictional resistance on the ship hull is reduced by air bubble injection, thereby reducing fuel consumption.

1.1 Air Lubrication

There are generally three different forms of resistance for ships moving in water. Form resistance, which is described by the shape of the vessel and hull, wave resistance which is the energy required to push water out of the way of the hull and frictional resistance, which is the resistance between a vessel's hull and the sea water. Air lubrication can reduce frictional resistance, which dominates in slow-moving ships, accounting for approximately 60-80% of the total resistance. The general concept of air lubrication for ships is to reduce the frictional resistance between water and the ship hull, which means reducing the wetted surface area by releasing air bubbles and covering parts of the bottom of the hull (Kim and Steen 2023).

Air lubrication for ships can be implemented in various ways. There are generally three different categories for air lubrication systems as classified by Mäkiharju et al. (2012): Bubble Drag Reduction (BDR), Air Layer Drag Reduction (ALDR) and Partial Cavity Drag Reduction (PCDR).

1.1.1 Bubble Drag Reduction

In BDR systems, air is injected at the bottom of the hull into the boundary layer through a porous material or similar. The air, which is separated in the form of bubbles, resides in the boundary layer and travels downstream of the hull. The bubbles reduce the local density of the air-water mixture thereby reducing the Reynolds stress. Additionally, the viscosity is reduced due to the change in void fraction, also reducing the skin friction (Kim and Steen 2023). A sketch of BDR implementation is seen in Figure 1.1. A drawback of BDR is the need for excessive gas injection and high power usage, as the bubbles tend to migrate from the near-wall region, reducing the effectiveness.

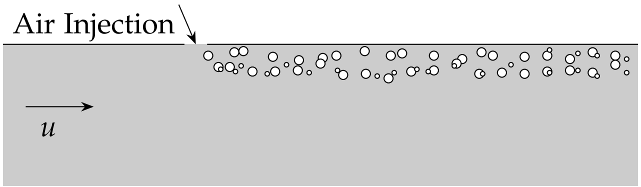

Figure 1.1: Sketch of implementation of BDR.

1.1.2 Air Layer Drag Reduction

Much research has found that when increasing the flux of the injected air, a transition from a bubbly flow of BDR to a continuous gas layer takes place. This phenomenon is referred to as ALDR. In ALDR air is injected as seen in Figure 1.2 to form a continuous gas layer, thereby reducing the frictional resistance. In papers by Ceccio (2010) and Elbing et al. (2013), the authors found that when a fully developed gas layer forms, a significant frictional drag reduction by up to 80% occurs. The gas flux required to transition from BDR to ALDR depends on several factors, such as free stream velocity, roughness of the hull surface and the hull shape.

Figure 1.2: Sketch of implementation of ALDR.

1.1.3 Partial Cavity Drag Reduction

In PCDR a gap is formed on the bottom of the hull which captures gas and creates a cavity between the hull and the free stream. It is typically designed as seen in Figure 1.3, with a backwards-facing step at the air injection point and a sloping closure downstream. The design of PCDR can help form the continuous air layer more easily when compared with ALDR. Continuous air injection is required to maintain the cavity, as some air is lost at the cavity closure. Generally, the gas flux needed to establish, and maintain a PCDR design is less than the ALDR. However, implementing PCDR on ships requires more drastic design alterations and current research is, as a result, more focused on the BDR and ALDR implementations.

Figure 1.3: Sketch of implementation of PCDR.

1.1.4 Air Lubrication Research and Modelling

Although air lubrication in the marine industry has been a known technology for many years, its implementation on full-scale ships is still in the early stages. Experimental sea trials using the ALDR design have been performed by Mizokami et al. (2010) and Hoang et al. (2009) and reported 10% and 7% net energy savings respectively. Fotopoulos and Margaris (2020) also performed numerical simulations on air lubrication systems to quantify fuel consumption and savings, and found that fuel savings of up to 8% can be reached. This illustrates the great potential for reducing frictional resistance in ships using air lubrication, and why additional research and modelling are of interest to utilise the technologies' full potential. Furthermore, accurate modelling frameworks such as computational fluid dynamics (CFD) models to help predict drag reduction and energy savings are also in the early stages. A thorough overview of the current air lubrication research is given in An et al. (2022). For modelling the multiphase phenomena of air lubrication, there are several approaches. Some of these will be introduced in the following chapter.

2 Modelling of Multiphase Flows

For numerical modelling of air lubrication, the presence of two different phases, in this case, gas and liquid, necessitates the need for multiphase modelling. When working within the field of multiphase flows, it is important to choose an appropriate model for the stated analysis. The difficulty of modelling air lubrication is the fact, that accurate simulation of individual air bubbles, in most models, requires computational cells in the order of mm to µm on a domain in the order of several hundred meters due to the size of commercial tankers and ships. This combination, results in the number of computational cells being in the order of billions, making such solutions improbable. Therefore, a tradeoff between accuracy and computational time is necessary to facilitate numerical modelling of air lubrication. The following sections describe various multiphase models and their use cases.

2.1 Discrete Phase Model

When using the discrete phase model, also known as the Euler-Lagrangian (E-L) approach, the liquid phase is computed as a continuous phase, meaning it is modelled using an Eulerian approach. The particles in the domain are however viewed as discrete phases, meaning they are tracked by an individual force balance analysis, thereby also giving the possibility of viewing all of the fluid dynamic forces acting upon said particle (Farzpourmachiani et al. 2011).

An E-L simulation is therefore based on tracking particles through a previously calculated flow field. Each particle is modelled and treated as a point mass. As the particles are tracked individually, the reference frame moves with the particles, and the particle position can be considered as a function of the starting position and time elapsed. Meanwhile, the Eulerian reference frame is stationary and the particles pass through fixed control volumes. Through coupling, particles can interact with the surrounding fluid or each other, which is important if a dense particle flow is simulated. One-way coupling occurs when the fluid affects the particle phase, two-way coupling is where the particle phase also affects the fluid phase, and four-way coupling mostly appears in dense particle flow where the particles interact with each other. The coupling is based on the Stokes number and particle volume fraction of the simulation in question (Michaelides et al. 2016). However, already at particle volume fractions above 1.5% particle-particle interactions have an important impact on the flow behaviour (Vreman et al. 2009).

2.1.1 State of the Art

The E-L approach proved beneficial for Muttenthaler and Manhartsgruber (2020) who studied solid contamination particles in a hydraulic reservoir for oil storage purposes. The method proved accurate for particle accumulation at different particle sizes and fluid velocities, which was further validated experimentally. The study of particles is also widely done in the chemical industry, where accurate mixing of chemicals is important in product quality. Haringa et al. (2016) and Dapelo et al. (2015) applied the E-L method to understand particle mixing in chemical reactors. The latter provided accurate validated results of a gas mixing process where the E-L approach was used to track the mixing of bubbles throughout the stirring tank. For a similar case of a 2D bubble column, Weber and Bart (2017) compared the computational time of the E-L method to an Euler-Euler (E-E) model. It was found that the E-L method has a linear correlation between injected particles and computational time, whereas the E-E method showed no significant increase in computational time with added particles. Weber and Bart (2017) further verified that above a certain particle quantity, the E-E method was less computationally demanding. This threshold can however be increased by the use of advanced search algorithms for particle tracking (Breuer et al. 2006).

2.2 Phasic Volume Models

Within a phasic volume model, every phase is treated as a continuum, also known as the Euler-Euler model. The method introduces a volume fraction, α, which describes the fraction of each phase within each control volume. Thus for a system of two phases, $\alpha = 1$ denotes a control volume filled with only the tracked phase, while $\alpha = 0$ denotes a cell where the tracked phase is not present. In cells where $0 \leq \alpha \leq 1$ the interface between the two phases is present. The volume fraction always equals one and is used when calculating the continuity and momentum equation within a control volume (Gopala and van Wachem 2008). This model proves to be a solid basis for multiple supplementary methods which are described in the following subsections.

2.2.1 Volume of Fluid Model

The volume of fluid (VOF) method is a surface-tracking approach designed for multiple immiscible fluids on a fixed computational grid. The VOF method gives the advantage that only a single set of momentum equations are to be solved, as a function of the volume fraction, greatly reducing the differential equations to be solved within each control volume. Additional interface tracking is necessary for cells where the volume fraction is between 0 and 1, and the interface is present (Hirt and Nichols 1981).

The VOF method generally uses one of two methods for interface tracking, geometric or algebraic schemes. Geometric schemes approximate the fluid interface geometrically by interpolating the computational cell volume fraction. Commonly used is the piecewise linear interface calculations (PLIC) by Rider and Kothe (1998), which produces a geometric interface using a linear approximation based on the cell volume fraction. Geometric schemes such as PLIC are more accurate than algebraic schemes, albeit at significantly higher code complexity and computational cost (Pirozzoli et al. 2019) (Xiao et al. 2005).

Algebraic schemes, which interpolate the surface from the volume fraction in a computational cell, using high-order differencing schemes, are therefore also used as computationally cheaper alternatives to geometric schemes. However, algebraic schemes are likely to cause numerical diffusion, thereby decreasing the accuracy of the model (Pirozzoli et al. 2019) (Comminal and Spangenberg 2021). VOF is therefore a useful tool when an accurate interface between phases is desired.

2.2.2 Mixture Model

The mixture model can compute multiple phases as a mixture, meaning that only a single mixture momentum equation needs to be solved, albeit an additional term for the drift velocity is introduced. This technique allows for calculating multiple interpenetrating phases at differing velocities while assuming a local equilibrium at short-length scales. The model can also be used for phases at the same velocity, representing a homogeneous multiphase flow. Unlike the VOF model, mixture models allow for the phases to be interpenetrating (Michaelides et al. 2016) (Mikko et al. 1996).

2.2.3 Eulerian Model

The Eulerian model is usually seen as a more complex version of the mixture model, where a set of momentum and continuity equations, with the volume fraction included, are solved for each phase in a control volume. The momentum coupling between different phases is achieved by interfacial momentum transfer modelled through a set of closure models describing forces such as drag, lift, virtual mass, etc. The computed phases are modelled as interpenetrating continua with a shared pressure field across phases (Liu et al. 2022) (Sattar et al. 2013a) (Sattar et al. 2013b).

2.2.4 State of the Art

The phasic volume models are valuable assets when researching multiphase flows in many industrial sectors. Within the transportation industry, research using the VOF method has been intensively used to research the sloshing effect in fuel tanks under acceleration (Zhu et al. 2023) (Godderidge et al. 2009). Kartuzova and Kassemi (2018) validated a VOF model on a vertical cylinder fuel tank undergoing a sudden lateral acceleration. The author found that the VOF model correctly captured the interface of the sloshing fuel. When comparing Reynolds-Averaged Navier-Stokes (RANS) and Large Eddy Simulation (LES) turbulence models, RANS produced adequate results, however, LES produced slightly more accurate results when compared with experimental data.

The E-E methods are also commonly used within spray atomisation simulations where analyses of each phase are desired. Pađen et al. (2021) studied the atomisation of secondary bubble breakup using the Eulerian model finding agreement between simulation and experimental results. Similar studies of the Eulerian and VOF models find that both techniques can accurately simulate the experimental results when considering bubbly flows in water (Edelbauer 2017) (Piña et al. 2022). In the maritime industry, multiphase models also play a significant role because any improvement in efficiency can lead to a significant economic benefit (Chiroșcă and Rusu 2021). Like Shin and Andersen (2019) who studied the thrust and cavitation of a maritime vessel propeller, to further understand the destructive phenomenon that cavitation can be.

The VOF model was also used with the Detached Eddy Simulation (DES) model which is an adaptive model switching between RANS and LES depending on the mesh refinement (Spalart et al. 1997). The use of the DES method shows that the authors considered one of the main dilemmas using the E-E method, namely the computational cost for larger geometries. Multiple works discuss how for bubbly flow, mesh sizing in the scale of µm for the commonly used VOF model is often needed to resolve the smallest bubbles and produce accurate results (Lloyd et al. 2017) (Yujie et al. 2012) (Ghiji et al. 2014). One reason for this is the bubble breakup phenomenon where one bubble can break up into many smaller bubbles frequently in the scale of mm and µm (Levitsky et al. 2005) (Solsvik and Jakobsen 2015) (Lima Neto et al. 2008). This means that simulating geometries on the scale of meters or larger where an accurate computation of the bubbles is important, quickly becomes impractical.

2.3 Hybrid Multi-Fluid Adaptive Models

As illustrated in previous sections, many approaches for modelling multiphase flow structures exist. As multiphase flows tend to be highly dynamic and governed by complex physics over a large range of length scales, selecting the appropriate model for a given case is important. The selection depends mainly on the interface shape and form. As described, multiphase models can generally simulate either dispersed structures at a smaller-than-grid scale such as Euler-Euler or Euler-Lagrange or resolved interfaces such as the VOF model at a larger-than-grid scale. In many modelling applications, the nature of the flow structure and morphology is unknown in advance, so selecting the appropriate approach can be challenging. Due to this, morphology-adapting models have recently gained increasing interest for complex gas-liquid flows as such models can adapt dynamically to local flow morphology changes. Yan and Che (2010) presented a two-fluid approach by combining a disperse Euler-Euler model with VOF interface reconstruction. Meanwhile, in the methods presented by Mathur et al. (2019) and Shonibare and Wardle (2015), the modelling is restricted to disperse flows of two fields, such as a gas and a liquid phase, without interface reconstruction. The models are benchmarked on several test cases showing good prediction of dispersed phases and large-scale interfaces.

Another such model is the Morphology-adaptive Multifield Two-fluid Model (MultiMorph) by HZDR described in Meller et al. (2021). This model is based on a 4-field approach, as the model distinguishes between two phases, eg. gas and liquid in both dispersed and continuous morphology. As is illustrated in Figure 2.1, structures which exist at a smaller than grid-scale, eg. the disperse phase, can not be resolved, and are therefore modelled with a statistical Euler-Euler approach. Meanwhile, structures above the grid scale can be resolved on the grid, and a Volume of Fluid approach is used.

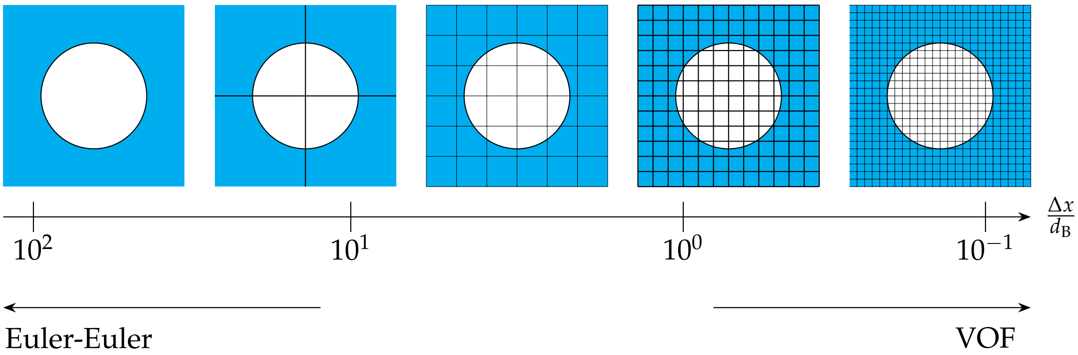

Figure 2.1: General modelling strategy of the MultiMorph model for an arbitrary bubble. Bubbles smaller than grid-scale can not be resolved, and Euler-Euler is used. Comparatively bubbles larger than grid-scale are resolved with the VOF model. Figure inspired by Meller et al. (2023).

In the range between these edge cases, a mixed approach is used. The main advantage of this model is the ability to model complex flow structures over a large range of spatial resolutions. Thereby obtaining high precision on fine grids and reasonable results on more coarse grids, reducing the computational requirements (Meller et al. 2023). In this way, individual air bubbles can be modelled on insufficient grid refinements with reasonable accuracy using an Eulerian approach, while a continuous air layer, as seen in ALDR, can be modelled with a VOF approach.

The MultiMorph model was verified by Meller et al. (2021), where velocity and sphericity results for a two- and three-dimensional rising bubble at various spatial grid resolutions were compared with the performance of a level-set method and experimental data. The results showed a maximum of approximately 3% deviation for the bubble rising velocity, while no difference in bubble shape is observed. Validation of the model was done by Tekavčič et al. (2021) on counter-current stratified flow for various implementation methods of turbulence damping. In general, the model showed good results for predicting the stratified flow phenomena in the tested case, when corrected values for turbulence damping were implemented as a result of a parametric study. The present work shows promising results for the MultiMorph modelling framework, however, validation of the model framework for air lubrication applications is lacking.

3 Problem Statement

Based on the multiphase models described in Section 2, the MultiMorph model is chosen for the air lubrication application. The MultiMorph model allows for the modelling of air bubbles on coarse grid refinements, while also allowing for accurate continuous air layer modelling on high grid refinement by switching between Euler-Euler and Volume of Fluid models. This work aims to extensively test and validate the MultiMorph model for air lubrication, by analysing whether both the BDR and ALDR regimes and the transition between them, can be predicted. This leads to the following problem statement:

Can the multifield two-fluid model MultiMorph accurately model the air-induced drag reduction in an air lubrication system?

- How can air lubrication be modelled by utilising the MultiMorph model?
- How can the MultiMorph model be validated with experimental data for air lubrication on a two-dimensional plate?
- How will surface roughness and multiple air injectors affect the air layer?
- How can a VOF LES air lubrication simulation help understand the MultiMorph framework's shortcomings, and the formation of air bubbles in the injector?

3.1 Overview of the Report

To assist the reader, an overview of the report structure and the contents of each chapter is given below.

- Chapter 4 gives a short description of relevant fluid dynamic theory and concepts, to provide an understanding of the phenomena and results throughout the report.
- Chapter 5 briefly describes the two-dimensional plate considered for analysis and validation. The geometry and several relevant parameters are listed.
- Chapter 6 describes the numerical modelling approach. This includes a description of the MultiMorph model and the numerical model setup. The following approach is used:
    - MultiMorph governing equations
    - Modelling in Euler-Euler mode

  - Modelling in Volume of Fluid mode
  - Modelling in the transition region
  - Numerical model setup

- Chapter 7 aims to validate the MultiMorph model for air lubrication on a two-dimensional plate, with experimental data. First, the chapter presents a sensitivity study of relevant model parameters, before a validation of the numerical model is done.

- Chapter 8 aims to analyse how the presence of air affects the boundary layer, and how surface roughness and several air injectors affect how the air layer forms and dissipates.

- Chapter 9 presents a VOF LES air lubrication simulation to analyse possible shortcomings of the MultiMorph model and to understand the air bubble generation better. The VOF LES model will consider a small domain around an air injector, with a very refined numerical mesh. Chapter 9 presents both the computational domain, numerical setup, model considerations and results of the VOF LES simulation.

4 Fluid Dynamics Theory

This chapter gives the reader a fundamental understanding of the fluid dynamics theory relevant to this project. The theory will be based on a flow over a flat plate, with additional information provided on how a multi-phase bubbly flow might affect each phenomenon. Firstly, the development of a boundary layer is described, as well as how numerical modelling of a boundary layer is done in Section 4.1. Afterwards, wall shear stress is described, which is used to define how the drag reduction is computed, in Section 4.2. Finally, a description of surface roughness, and how it is modelled, is given in Section 4.3.

4.1 Boundary Layer

A boundary layer emerges upon any flat plate with a fluid flowing with a relative velocity to said plate. Within the boundary layer, the fluid velocity develops from the free stream velocity to zero at the plate surface, known as the no-slip condition. As the boundary layer develops downstream, a transition from a laminar boundary layer to a turbulent boundary layer occurs at some critical Reynolds number ($\mathrm{Re}_{x,\mathrm{crit}}$). The governing laminar to turbulent transition parameter is the Reynolds number, Re_x, based on the distance from the plate's leading edge

$$\mathrm{Re}_x = \frac{\rho u_\infty x}{\mu} \tag{4.1}$$

where u_∞ is the freestream velocity, x the distance from the leading edge, μ the fluid viscosity and *rho* the fluid density. The laminar to turbulent boundary layer transition occurs over a plate region and not at a single point. For a plate with a sharp leading edge, this transition occurs in the region $\mathrm{Re}_{x,\mathrm{crit}} = 2 \cdot 10^5$ to $\mathrm{Re}_{x,\mathrm{crit}} = 3 \cdot 10^6$. The development of a boundary layer along a flat plate is shown in Figure 4.1.

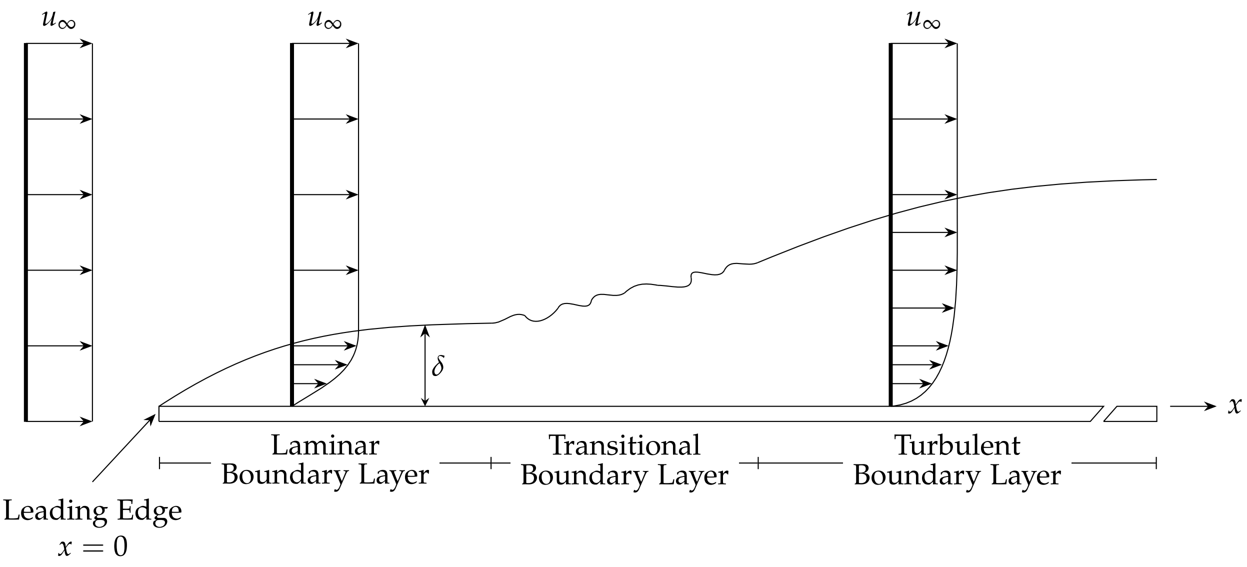

Figure 4.1: Illustration of a parallel flow boundary layer developing along a flat plate.

For the laminar boundary layer domain, the shear force between the plate and fluid is caused by the momentum transfer between molecules. The flow characteristics become more irregular and chaotic as the boundary layer develops into its turbulent domain. This phenomenon causes the shear force within a turbulent boundary layer to be noticeably greater than that of a laminar boundary layer. This effect results in the turbulent boundary layer having a larger thickness than the laminar boundary layer. The boundary layer thickness is defined as $u = 0.99u_\infty$, which gives the laminar boundary layer thickness, described by Schlichting (1979) as

$$\delta(x) \approx 5\frac{x}{\sqrt{\mathrm{Re}_x}} \tag{4.2}$$

and the turbulent boundary layer thickness for a turbulent flow

$$\delta(x) = 0.37\frac{x}{\mathrm{Re}_x^{1/5}} \tag{4.3}$$

4.1.1 Law of the Wall

A turbulent boundary layer is commonly composed of four layers, the viscous sublayer, buffer layer, logarithmic layer and the outer layer, wherein viscous forces dominate the viscous sublayer closest to the wall. As the distance from the boundary wall increases, the viscous forces gradually decrease until turbulent forces dominate in the fourth outer layer. The four layers in the near wall region can be described using the dimensionless velocity u^+ and wall distance y^+

$$u^+ = \frac{u}{u_\tau} \tag{4.4}$$

$$y^+ = \frac{yu_\tau}{\nu} \tag{4.5}$$

where the frictional velocity u_τ is described using the wall shear stress, τ_w as

$$u_\tau = \sqrt{\frac{\tau_\mathrm{w}}{\rho}} \tag{4.6}$$

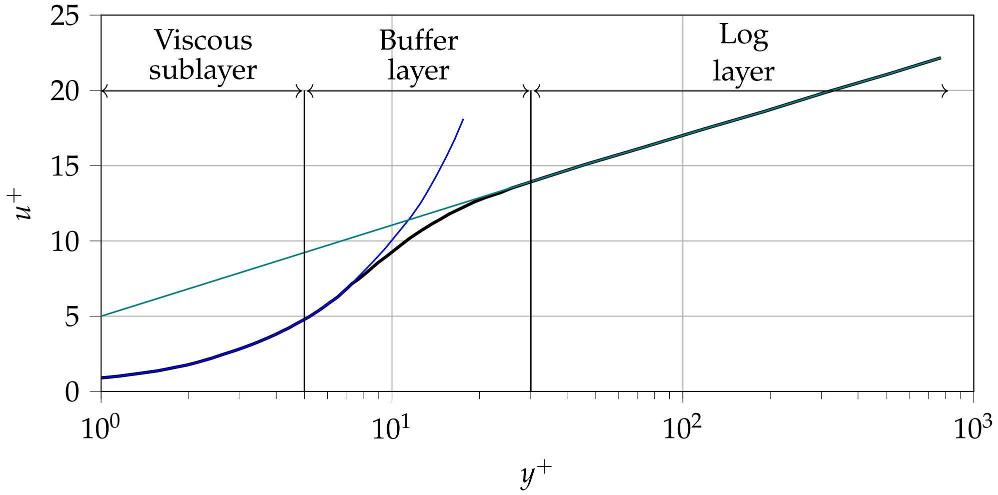

Figure 4.2: Dimensionless velocity, u^+ and wall distance, y^+ showing the velocity profile development in a boundary layer. Additionally, the three sublayers are shown.

The three layers closest to the wall are visualised in Figure 4.2 showing how in the viscous sub-layer

$$u^+ = y^+ \qquad (y^+ < 5) \tag{4.7}$$

and for the log-law layer

$$u^+ = \frac{1}{\kappa}\log(y^+) + B \qquad (y^+ > 30) \tag{4.8}$$

where κ is the von Kármán constant, typically defined as $\kappa = 0.41$ and $B = 5$ is a constant (Versteeg and Malalasekera 2007).

The buffer layer $(5 < y^+ < 30)$ is not well described and should be avoided as neither of the correlations holds. For simulations where the near-wall region physics are to be accurately resolved such as in Large Eddy Simulations, $y^+ < 1$ is imperative (Mangrulkar et al. 2019). However, if fully resolving the near-wall flow is not crucial, as is common in RANS simulations, wall functions are commonly used to predict the impact of the wall boundary upon the fluid for $y^+ > 30$.

4.1.2 Bubbly Flow Boundary Layer

In the air lubrication application, air bubbles and a continuous air layer will be present at the ship hull, affecting the boundary layer. Troshko and Hassan (1998) found that a bubbly boundary layer in turbulent flow conditions has the same structure as single-phase flow, although with reduced velocity. However, the structure of the specific boundary layer is largely affected by the volume fraction of bubbles within it. The general methodology behind modelling a bubbly boundary layer is by including additional circulation and turbulence around bubbles. This extra turbulence, also called bubble-induced turbulence (BIT) was included in a model made by Mikielewicz (2003) to predict bubbly turbulent boundary layers. The model was compared with experimental data, where a satisfactory agreement was achieved.

Law of the Wall for Bubbly Flow

As mentioned, the bubbly flow boundary layer will typically have the same asymptotic structure as a single-phase boundary layer. This means that the law of the wall should hold for the case of bubbly flow. Marié et al. (1997) proposed a log-law for bubbly flow in the near-wall region, in the same structure as the single phase log-law as

$$u^+ = \frac{1}{\kappa^*}\log(y^+) + B^* \tag{4.9}$$

where $\kappa^* = \kappa/\gamma^*$ is a modified von Kármán constant, with γ^* being a correction function which depends on bubble parameters such as the diameter and local void fractions. However, the bubbly flow log-law is shown in Bragg et al. (2021) to only hold for flow cases, in which the bubbles play a small role in the flow dynamics. Through DNS simulations the authors found that for bubbly turbulent flows with higher bubble concentration, the log-law can not represent the boundary layer flow characteristics, but rather bubble parameters such as the density ratio $\rho_\text{l}/\rho_\text{g}$, void fraction and bubble diameter dominate. Especially the density ratio may affect the boundary layer significantly, as a local density change will affect the Reynolds number and thus the turbulence.

4.1.3 Turbulence Kinetic Energy Along a Flat Plate

In a turbulent flow, the velocity at any point in space will fluctuate chaotically about some mean velocity as

$$u_i(t) = \langle u_i \rangle + u_i' \tag{4.10}$$

where $\langle u_i \rangle$ represents the time averaged velocity. The magnitude of the velocity fluctuations can be characterised by the turbulence kinetic energy, k, at said point. The turbulence kinetic energy per unit mass is computed as

$$k = \frac{1}{2}\left(\langle u'^2\rangle + \langle v'^2\rangle + \langle w'^2\rangle\right) \tag{4.11}$$

Turbulence intensity, I, can be determined based on the turbulence kinetic energy and a reference flow velocity, u_{ref}, characterising the velocity fluctuations on a percentile scale

$$I = \frac{(2/3\,k)^{1/2}}{u_{\text{ref}}} \tag{4.12}$$

where the numerator represents the root mean square of the velocity fluctuations over a time interval (Schlichting 1979).
As the boundary layer develops in its laminar region, the turbulence kinetic energy stays steady at zero, as long as no interruptions occur. When the boundary layer inevitably becomes turbulent along a flat plate, the turbulence kinetic energy in the boundary layer increases, as the boundary layer develops (Siikonen et al. 2019).

In the wall-normal direction, the turbulence kinetic energy approaches 0 at the wall (Wei 2020). Whereas, just off the wall, the turbulence kinetic energy peaks at $y^+ \approx 30$, after then slowly decreasing as the distance to the wall increases (Lardeau et al. 2012) (Siikonen et al. 2019).

4.2 Wall Shear Stress

For any object moving with a relative velocity to the fluid it is immersed within, a shear force is exerted on it, known as wall shear stress. The wall shear stress decreases as the boundary layer thickens, as a consequence of the velocity gradient at the wall decreasing. For a flat plate, the wall shear stress thus decreases as the distance from the leading edge increases. With a known velocity profile, the wall shear stress on the plate surface can be determined by

$$\boldsymbol{\tau}_{\text{w}} = \mu \frac{\partial \boldsymbol{u}}{\partial \boldsymbol{y}}_{y=0} \tag{4.13}$$

where $\boldsymbol{y}$ is the normal distance from the plate (Munson et al. 2012). For flow parallel to a flat plate, an analytical solution for the wall shear stress can be derived as (Schlichting 1979)

$$\boldsymbol{\tau}_{\text{w}} = 0.332 \mu u_{\infty} \sqrt{\frac{u_{\infty}}{\nu x}} \tag{4.14}$$

where x is the distance from the leading edge of a plate. The wall shear stress as a function of distance x for pure water and an air-water mixture is shown in Figure 4.3.

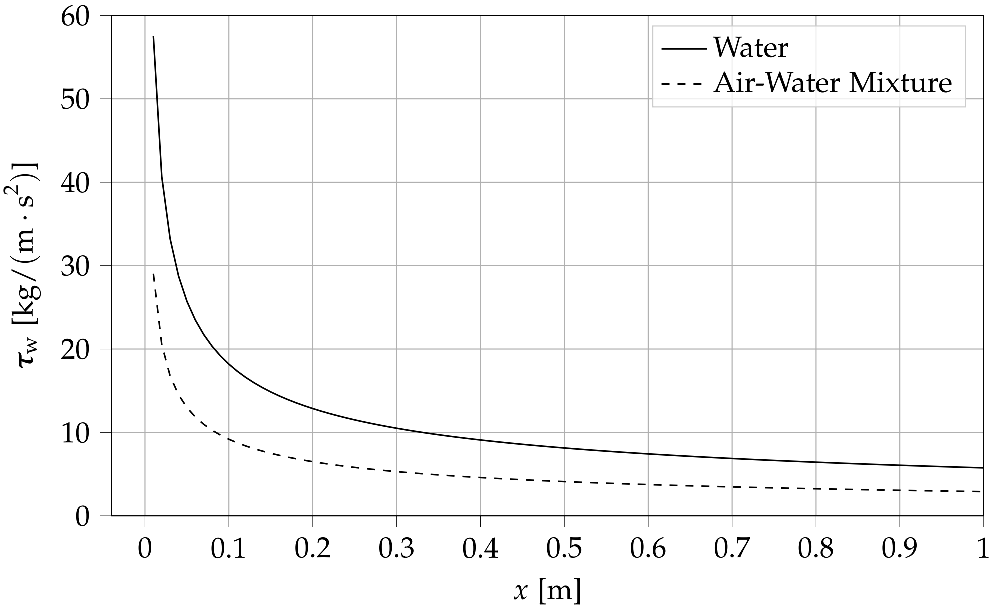

Figure 4.3: Analytically calculated wall shear stress along a flat plate for pure water and an air-water mixture, from Equation 4.14.

The wall shear stress can then be used to find the frictional drag force exerted upon the plate by the fluid by

$$F_D = \int \tau_w \sin\theta \, dA \tag{4.15}$$

where θ is the angle between the surface normal and the fluid velocity, and dA is some element area. For a flat plate parallel to the flow direction, the term reduces to $F_D = \int \tau_w \, dA$.
From Equation 4.14, it is evident that the viscosity directly influences the wall shear stress, and thereby the drag on an object. As the dynamic viscosity of air is roughly 10 times lower than water's, injecting air under the hull of a ship, as is done in air lubrication, will likely reduce the frictional drag. This is also seen in Figure 4.3, where the wall shear stress is reduced for the mixture of air and water.

To quantify frictional drag reduction, a drag reduction (DR) parameter will be used. In this work, DR will be given as a percentage drag reduction between a multiphase case with air-induced drag reduction, and a singlephase case without air injection. The percentage DR is calculated according to Elbing et al. (2008) as

$$\mathrm{DR} = \frac{\int \tau_{w,1} \, dA - \int \tau_{w,2} \, dA}{\int \tau_{w,1} \, dA} \cdot 100 \tag{4.16}$$

where subscripts 1 and 2 denote the wall shear stress for two different cases. In this report, the wall shear stress will be integrated over a full plate or for a smaller section of the plate.

4.3 Surface Roughness Modelling

When modelling surface roughness, two analysis methods are commonly used. The first method is to completely model a rough surface, which requires a very fine mesh resolution. The second method is to model the effect of the surface roughness upon the fluid by models such as the equivalent sand grain approach. Due to the high computational cost of the first method, the second method, albeit less accurate, is the most commonly used in industrial applications (Lipej et al. 2017).

4.3.1 General Surface Roughness

To represent surface roughness a surface profile, as illustrated in the top part of Figure 4.4, is commonly used. From a surface profile, the parameters R_{am} and R_{z} can be extracted to describe the roughness. R_{am} is the arithmetic mean of the absolute values of the profile. The lesser-used parameter R_{z} is a peak-to-valley parameter, meaning that it is the mean of the distance between the five highest peaks and five lowest valleys (Adams et al. 2012).

If a large profile height is observed throughout a surface profile, using the arithmetic mean parameter to describe the roughness, can result in inaccurate smoothening of the surface roughness. For such cases, the peak-to-valley parameter gives a better representation of the surface roughness (Johansson 2014).

4.3.2 Equivalent Sand-Grain Roughness

The mentioned equivalent sand grain roughness approach, developed from an experimental study by Nikuradse (1950), is based on the principle that having spherical sand grains on a surface can accurately resemble surface roughness.

To adapt the real surface roughness to an equivalent sand-grain size, an equivalent wall roughness, ϵ, is defined as the average sand-grain diameter, as visualised in Figure 4.4. Adams et al. (2012) developed a simple algorithm which converts a measured surface roughness to an equivalent sand-grain roughness, using the relations presented in Equations 4.17 and 4.18.

$$\epsilon = 5.863 R_{\mathrm{am}} \tag{4.17}$$

$$\epsilon = 0.978 R_{\mathrm{z}} \tag{4.18}$$

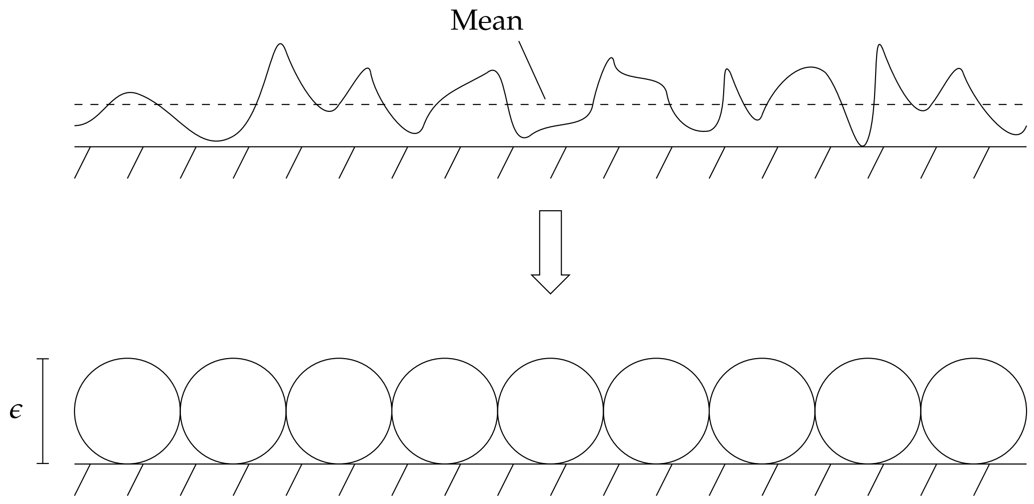

Figure 4.4: Conversion from surface roughness to equivalent sand-grain roughness.

However, real surfaces do not have a surface as regular as that represented by a monolayer of equally sized sand grains. Because of this, a roughness constant, C_s, is introduced to denote either a uniform or non-uniform equivalent sand grain roughness both in terms of height and spacing. The roughness constant can take values between 0.5 and 1, where $C_s = 0.5$ denotes a uniform surface roughness, while $C_s = 1$ denotes a strongly non-uniform roughness.

5 System Description

The numerical model will be based on a two-dimensional flat plate of length L_1, shown in Figure 5.1, with the domain height defined as D. For the air lubrication application, the air is injected at X_{inj}, which occurs a distance of L_2 downstream on the plate. A uniform velocity profile $u_{\mathrm{w,b}}$ is implemented at the water inlet. The dimensions of the numerical domain are listed in Table 5.1.

The coordinate system is set, such that the point of air injection occurs at $x = 0$.

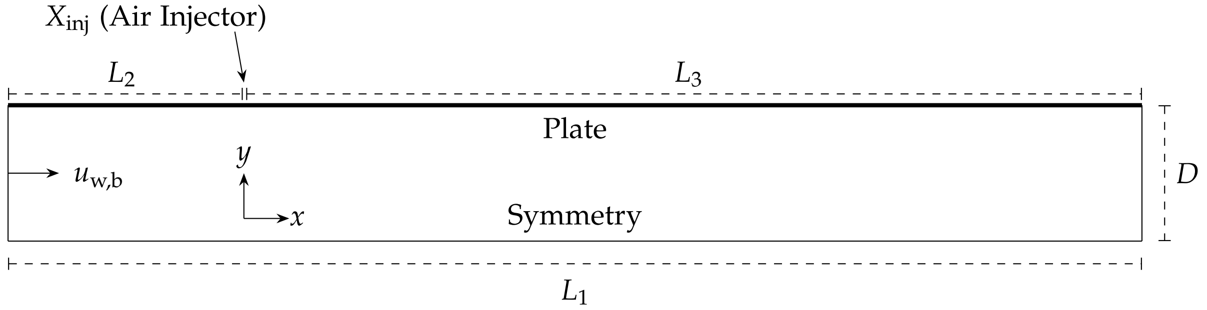

Figure 5.1: Illustration of the two-dimensional model setup on which validation of the MultiMorph model will be done.

Table 5.1: Geometric properties for the numerical model and the bulk velocity.

Symbol	Description	Value
D	Domain height	0.5 m
L_1	Plate length	$24D$
L_2	Length before injector	$4D$
L_3	Length after injector	$20D$
$u_{\mathrm{w,b}}$	Inlet water bulk velocity	11.1 m/s

6 Numerical Approach

The following sections will describe the MultiMorph model framework developed by Schlegel et al. (2023) for the air lubrication application. The meshing strategy and boundary conditions for the numerical model will also be presented.

In the MultiMorph model, the general modelling strategy, depending on grid refinement, is illustrated in Figure 6.1. The method combines the Euler-Euler model with a Volume of Fluid model, based on URANS equations with a k-ω SST model for the liquid phase turbulence. As mentioned, the MultiMorph model is a multifield two-fluid model, meaning it can handle two different states, either disperse or continuous, for each phase resulting in four different *morphologies*:

- Disperse water (droplets)
- Continuous water
- Disperse air (bubbles)
- Continuous air

Each morphology can coexist independently and is coupled by appropriate mass and momentum exchange terms. For air lubrication, only three morphologies are required to cover the problem; continuous water, disperse air bubbles and continuous air.

The model framework is presented with the following approach:

1. Phase-averaged Navier-Stokes governing equations
2. Model considerations in dispersed mode
3. Model considerations in resolved mode
4. Morphology transfer in the transition region

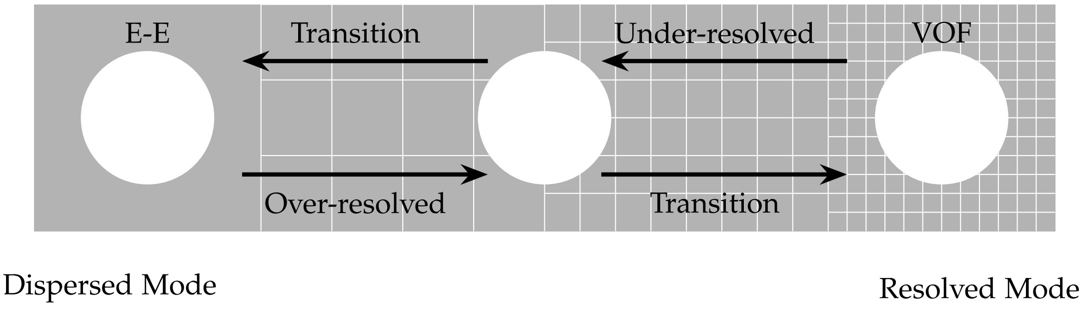

Figure 6.1: Illustration of the modelling strategy employed in the two-fluid MultiMorph model, dependent on grid refinement level. The white circles represent gas bubbles.

6.1 Governing Equations

The MultiMorph model applies to incompressible isothermal multifluid flows based on finite volume discretization. In the following governing equations, the subscript r denotes an arbitrary phase, while the subscripts "l" and "g" denote the liquid and gas phases, respectively. The phase-averaged mass and momentum conservation equations of a phase r are given as

$$\frac{\partial \alpha_\mathrm{r}\rho_\mathrm{r}}{\partial t} + \nabla \cdot (\boldsymbol{u}_\mathrm{r}\alpha_\mathrm{r}\rho_\mathrm{r}) = \Gamma_\mathrm{r} \tag{6.1}$$

$$\frac{\partial(\alpha_\mathrm{r}\rho_\mathrm{r}\boldsymbol{u}_\mathrm{r})}{\partial t} + \nabla \cdot (\alpha_\mathrm{r}\rho_\mathrm{r}\boldsymbol{u}_\mathrm{r}\boldsymbol{u}_\mathrm{r}) = \nabla \cdot (2\alpha_\mathrm{r}\mu_\mathrm{r}\boldsymbol{S}_\mathrm{r}) - \alpha_\mathrm{r}\nabla p + \alpha_\mathrm{r}\rho_\mathrm{r}\boldsymbol{g} + \boldsymbol{f}_\mathrm{r} + \boldsymbol{\Gamma}^*_\mathbf{r} \tag{6.2}$$

where α is the phase fraction, ρ the phase density, $\boldsymbol{u}$ the phase velocity vector, μ_r the phase dynamic viscosity, p the pressure shared by both phases, $\boldsymbol{f}_\mathrm{r}$ the interfacial momentum exchange vector and $\boldsymbol{g}$ the gravitational acceleration vector. The source term $\boldsymbol{S}_\mathrm{r}$ describes the phase-specific shear-rate tensor.

$$\boldsymbol{S}_\mathrm{r} = \frac{1}{2}(\nabla \cdot \boldsymbol{u}_\mathrm{r} + (\nabla \cdot \boldsymbol{u}_\mathrm{r})^\mathrm{T}) - \frac{1}{3}(\nabla \cdot \boldsymbol{u}_\mathrm{r})\mathbf{I} \tag{6.3}$$

$\Gamma_\mathrm{r} = \sum \Gamma_\mathrm{lg}$ and $\boldsymbol{\Gamma}^*_\mathbf{r} = \sum \Gamma_\mathrm{lg}\boldsymbol{u}_\mathrm{r}$ describe interfacial mass exchange and momentum exchange due to mass exchange, respectively. These are described further in Section 6.4. Note that, Γ_r and $\boldsymbol{\Gamma}^*_\mathbf{r}$ only contribute to the equations, if phase transfer is taking place.

The equations are integrated in time with a semi-implicit first-order accurate Euler scheme and spatially discretised with the second-order accurate finite volume method.

6.1.1 Turbulence Modelling

The turbulence of the liquid phase is modelled by the k-ω Shear-Stress Transport (SST) URANS turbulence model. The ω_k transport equation is given in Menter et al. (2003) as

$$\frac{\partial(\alpha_l \rho_l \boldsymbol{u}_l)}{\partial t} + \nabla \cdot (\alpha_l \rho_l \boldsymbol{u}_l \omega_l) = \nabla(\alpha_l(\mu_l + \sigma_\omega \mu^{\mathrm{T}})\nabla \omega_l) + \frac{\alpha_l \rho_l \gamma}{\mu^{\mathrm{T}}} \tilde{P}_l - \beta \alpha_l \rho_l \omega_l^2 \tag{6.4}$$

$$+2(1-F_1)\frac{\alpha_l \rho_l \sigma_{\omega 2}}{\omega_l}(\nabla k_l)(\nabla \omega_l) + S^{\omega}_{\mathrm{TDa}} + S^{\omega}_{\mathrm{BIT}}$$

where k_l is the turbulence kinetic energy, μ_l and μ_l^{T} are the dynamic and eddy viscosities, respectively. $\tilde{P}_l$ is the turbulence kinetic energy production term, and F_1, σ_ω, $\sigma_{\omega 2}$, γ and β are model coefficients.

In the k-ω SST model, the eddy viscosity is given as

$$\mu^{\mathrm{T}} = \frac{a_1 \rho k}{\max(a_1 \omega, S F_2)} \tag{6.5}$$

where a_1 is a model constant, F_2 is a blending function and S is the mean rate of deformation. $S^{\omega}_{\mathrm{TDa}}$ and $S^{\omega}_{\mathrm{BIT}}$ are the turbulence damping and bubble-induced turbulence source terms, described in Section 6.3.3 and 6.2.1, respectively.

6.2 Dispersed Mode

In the case of a coarse mesh, the model tends towards an Euler-Euler formulation as seen in Figure 6.2, thus a set of closure models is necessary to model interfacial momentum transfer terms between the disperse air bubbles and continuous water. The closure models consist of various forces acting upon a disperse bubble, and a model for bubble-induced turbulence (BIT).

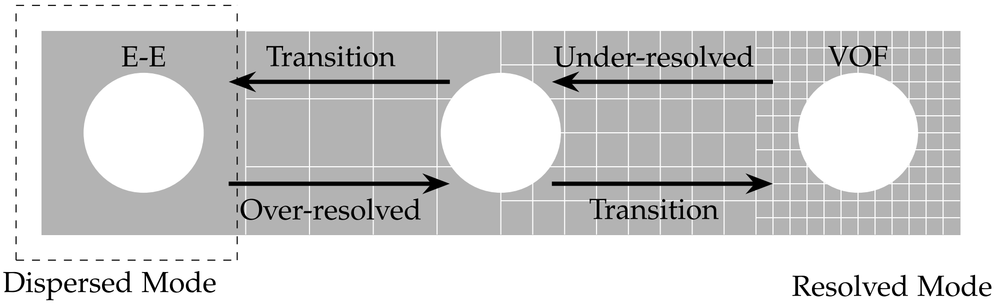

Figure 6.2: Illustration of the modelling strategy employed in the two-fluid MultiMorph model, dependent on grid refinement level. The white circles represent gas bubbles. Focusing on the dispersed mode.

6.2.1 Analysis of Disperse Phase Bubble Force Closure Models

The interfacial momentum exchange term $\boldsymbol{f}_{\mathrm{r}}$, consists of closure models for the momentum transfer between disperse air bubbles and continuous water. Closure models for the lift, drag, virtual mass, wall lubrication and turbulent dispersion force are considered:

$$\boldsymbol{f}_{\mathrm{r}} = \sum \boldsymbol{f}_{\mathrm{lg}} = \boldsymbol{F}^{\mathrm{L}}_{\mathrm{lg}} + \boldsymbol{F}^{\mathrm{D}}_{\mathrm{lg}} + \boldsymbol{F}^{\mathrm{VM}}_{\mathrm{lg}} + \boldsymbol{F}^{\mathrm{W}}_{\mathrm{lg}} + \boldsymbol{F}^{\mathrm{TD}}_{\mathrm{lg}} \tag{6.6}$$

Figure 6.3 presents the five forces acting upon a bubble and provides an overview of which direction each bubble force is acting.
A parameter variation will be done for each bubble force closure model to understand how the force models behave. Buoyancy and gravitational forces acting upon each phase are also present in the model but are outside the scope of this analysis.

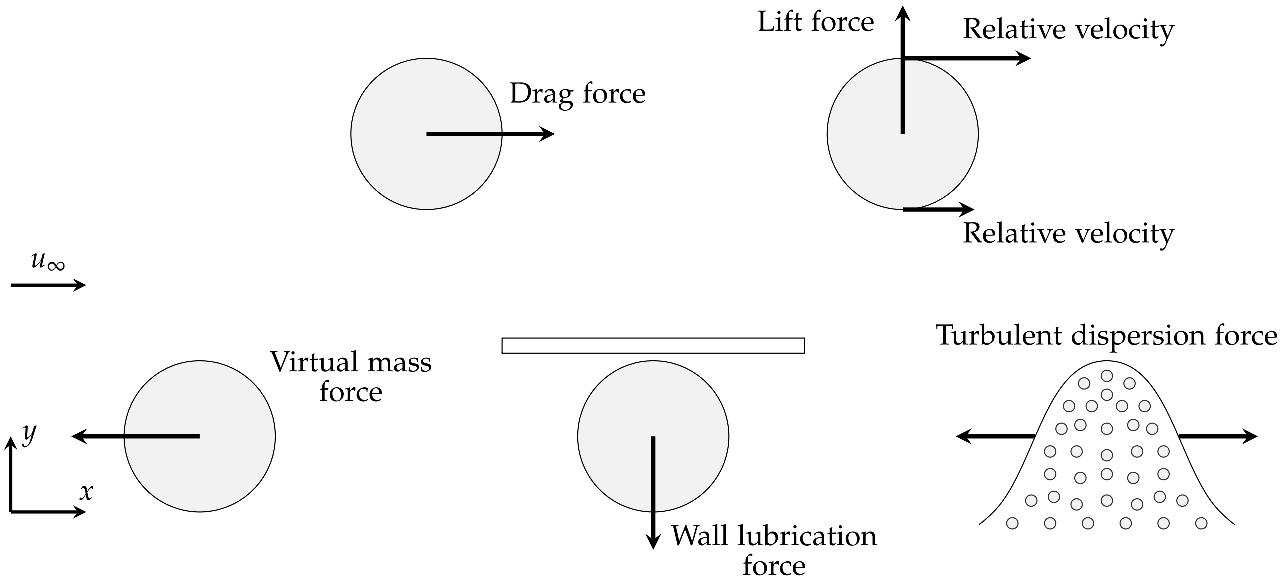

Figure 6.3: Illustration of forces acting upon a bubble in the disperse phase. The freestream velocity direction is denoted as u_∞, and the force direction is shown for each force.

Drag Force

In viscous flows, a force will act upon an object moving through a fluid due to friction. This is defined as the viscous drag force, $\boldsymbol{F}^{\mathrm{D}}$, and will always act in the same direction as the relative fluid velocity. In general, the drag force is a function of the fluid density ρ_{l}, some characteristic surface area A, a drag coefficient C_{D} and relative velocity squared $\boldsymbol{u} \cdot |\boldsymbol{u}|$, given as:

$$\boldsymbol{F}^{\mathrm{D}} = \frac{1}{2} C_{\mathrm{D}} \rho_{\mathrm{l}} \, \boldsymbol{u} \cdot |\boldsymbol{u}| A \tag{6.7}$$

In the Euler-Euler framework, the drag force is acting upon a bubble or droplet suspended in a liquid, therefore, the drag force equation can be rewritten, by defining A as the cross-sectional area of a sphere and dividing by the volume of a sphere, as

$$\boldsymbol{F}_{\mathrm{lg}}^{\mathrm{D}} = \frac{3}{4d_{\mathrm{B}}} C_{\mathrm{D}} \rho_{\mathrm{l}} \alpha_{\mathrm{g}} \left| \boldsymbol{u}_{\mathrm{g}} - \boldsymbol{u}_{\mathrm{l}} \right| \left(\boldsymbol{u}_{\mathrm{g}} - \boldsymbol{u}_{\mathrm{l}} \right) \tag{6.8}$$

where d_{B} is the bubble diameter for a spherical bubble and α_{g} is the volume fraction of a bubble within a computational cell. In the MultiMorph framework, the drag coefficient C_{D} is based on the work of Ishii and Zuber (1979), who define the drag coefficient on a spherical bubble as

$$C_{\mathrm{D}} = \max\left(C_{\mathrm{D,sphere}}, C_{\mathrm{D,cap}}\right), \text{where} \tag{6.9}$$

$$C_{\mathrm{D,sphere}} = \frac{24}{\mathrm{Re_p}}\left(1 + 0.1\mathrm{Re_p^{0.75}}\right)$$

$$C_{\mathrm{D,cap}} = \frac{8}{3}$$

where the single-particle Reynolds number is defined as $\mathrm{Re_p} = (d_{\mathrm{B}}\rho_{\mathrm{l}}(\boldsymbol{u}_{\mathrm{g}} - \boldsymbol{u}_{\mathrm{l}}))/\mu_{\mathrm{l}}$ for a bubble.

Figure 6.4, analyses the drag force at varying relative velocities and bubble diameters. The drag force increases exponentially with increasing relative velocity, proving an important parameter for the drag force. For the bubble diameter variation, larger bubbles will experience a larger drag force acting upon them, while the drag force decreases for a decreasing bubble diameter.

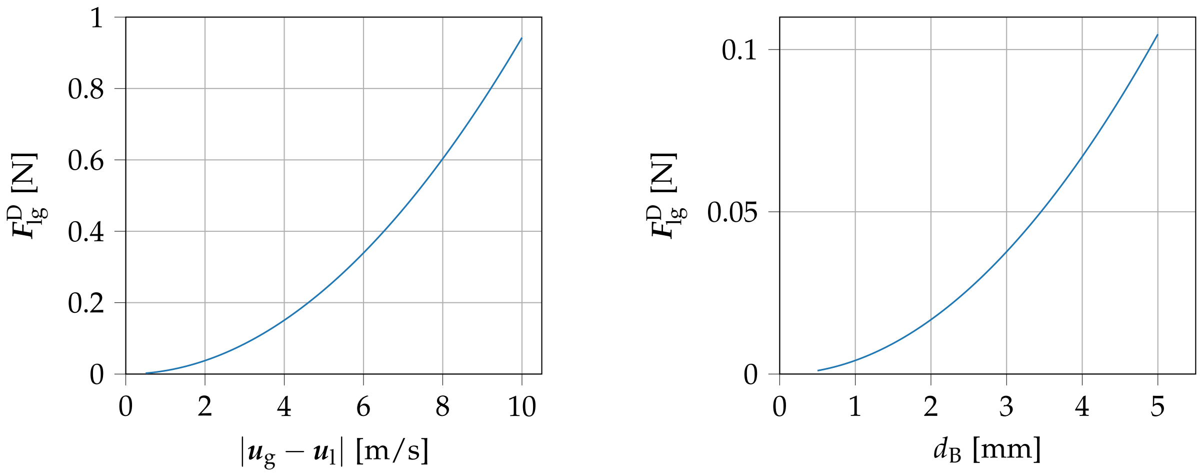

(a) A constant bubble diameter of $d_{\mathrm{B}} = 3$ mm is used for the relative velocity variation.

(b) A constant relative velocity of $|\boldsymbol{u}_{\mathrm{g}} - \boldsymbol{u}_{\mathrm{l}}| = 2$ m/s is used for the bubble diameter variation.

Figure 6.4: Analysis of drag force, as formulated by Ishii and Zuber (1979), with varying bubble diameter, d_{B}, and relative velocity, $|\boldsymbol{u}_{\mathrm{g}} - \boldsymbol{u}_{\mathrm{l}}|$.

Lift Force

The lift force $\boldsymbol{F}^{\mathrm{L}}$ is defined as acting perpendicular to the relative fluid velocity. The lift force occurs due to a bubble being subject to shear flows, thus there may be a difference in relative velocity on different parts of the bubble, as illustrated in Figure 6.3. This can cause rotation in the bubble, ultimately resulting in the bubble experiencing a lift force. In the Euler-Euler models, the lift force on a small spherical bubble passing a shear field is therefore defined as

$$\boldsymbol{F}^{\mathrm{L}}_{\mathrm{lg}} = C_{\mathrm{L}}\, \rho_{\mathrm{l}}\, \alpha_{\mathrm{g}}(\boldsymbol{u}_{\mathrm{g}} - \boldsymbol{u}_{\mathrm{l}}) \times (\boldsymbol{\nabla} \times (\boldsymbol{u}_{\mathrm{l}})) \tag{6.10}$$

where $\boldsymbol{\nabla} \times (\boldsymbol{u}_{\mathrm{l}})$ describes the curl of the liquid phase and C_{L} is the lift coefficient.

The difficulty in achieving accurate predictions of lift force lies in determining an accurate expression for said coefficient. The correlation used for this project, described in Hessenkemper et al. (2021), is a combination of the function of the dimensionless shear rate Sr and particle Reynolds number $\mathrm{Re_p}$, $f(\mathrm{Sr}, \mathrm{Re_p})$ and an applied fit $f(\mathrm{Eo}_\perp)$ where $\mathrm{Eo}_\perp$ is the modified Eötvös number, thus

$$C_{\mathrm{L}} = f(\mathrm{Sr}, \mathrm{Re_p}) - f(\mathrm{Eo}_\perp), \text{ where} \tag{6.11}$$

$$f(\mathrm{Eo}_\perp) = \frac{\ln(1 + \exp(-12(G)))}{12}$$

$$G = 0.11\frac{\ln(1 + \exp(4(\mathrm{Eo}_\perp - 5.6)))}{4} - 0.14(\mathrm{Eo}_\perp - 5.2) - 0.44, \text{ and}$$

$$f(\mathrm{Sr}, \mathrm{Re_p}) = \left(\left(\frac{6}{\pi^2}\frac{1}{\sqrt{\mathrm{Re_p Sr}}}\frac{2.255}{(1 + 0.2\epsilon^{-2})^{3/2}}\right)^2 + \left(0.5\frac{\mathrm{Re_p} + 16}{\mathrm{Re_p} + 29}\right)^2\right)^{1/2} \tag{6.12}$$

$$\mathrm{Re_p} = \frac{\rho_{\mathrm{l}}(\boldsymbol{u}_{\mathrm{g}} - \boldsymbol{u}_{\mathrm{l}})d_{\mathrm{B}}}{\mu_{\mathrm{l}}};\ \mathrm{Sr} = \frac{d_{\mathrm{B}}\gamma}{(\boldsymbol{u}_{\mathrm{g}} - \boldsymbol{u}_{\mathrm{l}})};\ \epsilon = \left(\frac{\mathrm{Sr}}{\mathrm{Re_p}}\right)^{1/2};\ \mathrm{Eo}_\perp = \frac{\Delta\rho_{\mathrm{lg}} g d^2_{\mathrm{major}}}{\sigma_{\mathrm{lg}}}$$

where γ is the shear rate and d_{major} denotes the major axis of a bubble. The proposed lift coefficient is valid only for bubbles of sizes smaller than 6.5 mm.

As the lift force of Equation 6.10 is a challenging calculation, only the lift coefficient is presented in the following Figure 6.5. The analysis shows that the relative velocity between the two phases has a negligible effect on the lift coefficient. However, the influence of relative velocity is more pronounced at low values.

For the bubble diameter variation, the analysis shows, that the lift coefficient, and thus the lift force, changes sign at a critical bubble diameter of $d_\mathrm{B} \approx 1.8$ mm. This means, that bubbles larger than the critical diameter, will have a force pointing towards regions with higher liquid velocity, thus away from the wall. Meanwhile, bubbles smaller than the critical diameter will have a lift force towards the wall (Lucas et al. 2005).

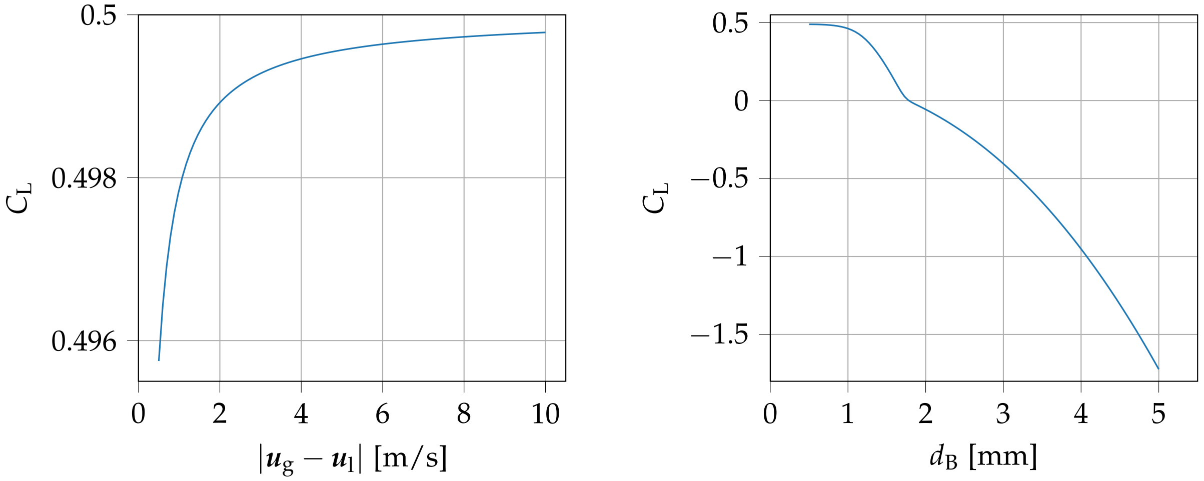

(a) For the relative velocity variation, a constant bubble diameter of $d_\mathrm{B} = 3$ mm is used.

(b) For the bubble diameter variation, a constant relative velocity of $|\boldsymbol{u}_\mathrm{g} - \boldsymbol{u}_\mathrm{l}| = 2$ m/s is used.

Figure 6.5: Lift coefficient of Hessenkemper et al. (2021) shown for varying relative velocity and bubble diameter in (a) and (b), respectively.

Virtual Mass Force

Virtual mass must be considered when a submerged body in fluid accelerates or decelerates thus accelerating some mass of the surrounding fluid. In the air lubrication application, this must be modelled for the air bubbles dispersed in a continuous phase. This is especially important, as the density of the submerged body, in this case, air, is much smaller than the surrounding water. To accelerate the bubbles, both it and the surrounding fluid must be set in motion. The virtual mass force between a disperse phase, and continuous phase, can then be defined according to Crowe et al. (2011) as

$$\boldsymbol{F}_\mathrm{lg}^\mathrm{VM} = \alpha_\mathrm{g} \rho_\mathrm{l} C_\mathrm{lg}^\mathrm{VM} \left(\frac{\mathrm{d}\boldsymbol{u}_\mathrm{g}}{\mathrm{d}t} - \frac{\mathrm{d}\boldsymbol{u}_\mathrm{l}}{\mathrm{d}t} \right) \tag{6.13}$$

where $C_\mathrm{lg}^\mathrm{VM}$ is the virtual mass coefficient. The virtual mass coefficient is a dimensionless coefficient, which depends on the shape of the object. This model uses a constant value of $C_\mathrm{lg}^\mathrm{VM} = 0.5$, which is the value often used in literature (Crowe et al. 2011).

The virtual mass force varied as a function of the relative acceleration, is presented in Figure 6.6. A linear correlation is seen between the force and relative acceleration, with increasing acceleration resulting in increasing virtual mass force.

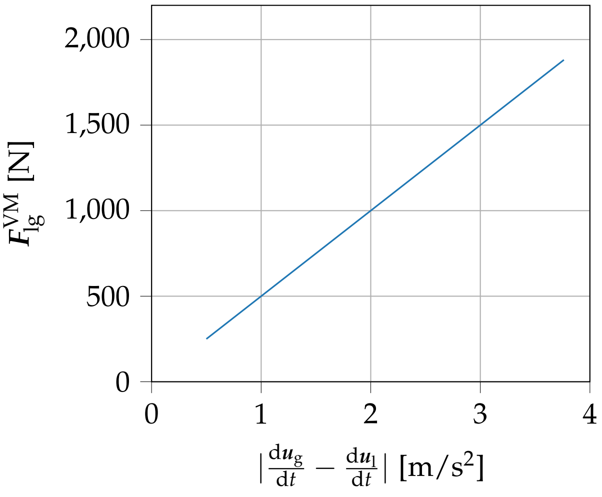

Figure 6.6: Analysis of the virtual mass force, proposed by Crowe et al. (2011), as a function of the relative acceleration between two phases.

Wall Lubrication Force

In bubbly flows, a lubrication effect results in a reduction of bubbles in the near-wall region. This results in bubbles being repelled from the wall by a force, maintaining a lubrication water film between the wall and the gas layer. For multiphase simulations, if this is disregarded, a large overshoot of the gas fraction in near-wall computational cells can occur. A model is therefore necessary, to prescribe an artificial force in this region, to model migration of gas bubbles away from the wall. The formulation of the wall lubrication force used in this model is proposed by Hosokawa et al. (2002).

$$\boldsymbol{F}_{\mathrm{lg}}^{\mathrm{W}} = \frac{2}{d_{\mathrm{B}}} C_{\mathrm{W}} \alpha_{\mathrm{g}} \left(\frac{d_{\mathrm{B}}}{2y}\right)^2 \rho_{\mathrm{l}} |\boldsymbol{u}_{\mathrm{g}} - \boldsymbol{u}_{\mathrm{l}}|^2 \hat{\boldsymbol{y}} \tag{6.14}$$

where d_{B} is the bubble diameter, y is the vertical distance from the wall, and $\hat{\boldsymbol{y}}$ is the wall normal vector. C_{W} is the wall lubrication coefficient, which was obtained by Hosokawa et al. (2002) and is a function of either the Reynolds number or Eotvos number.

$$C_{\mathrm{W}} = \max\left\{\frac{3.5}{\mathrm{Re}_{\mathrm{p,t}}{}^{1.9}},\ 0.0185\mathrm{Eo}\right\} \tag{6.15}$$

The Reynolds number is in this case based on the terminal velocity for a bubble in a spherical regime defined as

$$\mathrm{Re}_{\mathrm{p,t}} = \frac{\rho_{\mathrm{l}} u_{\mathrm{t}} d_{\mathrm{B}}}{\mu_{\mathrm{l}}}, \qquad u_{\mathrm{t}} = \frac{g d_{\mathrm{B}}^2 \Delta\rho}{6\mu_{\mathrm{l}}} \frac{1 + \mu_{\mathrm{g}}/\mu_{\mathrm{l}}}{2 + 3\mu_{\mathrm{g}}/\mu_{\mathrm{l}}} \tag{6.16}$$

and the Eotvos number is defined as

$$\mathrm{Eo} = \frac{\Delta\rho_{\mathrm{lg}} g d_{\mathrm{B}}}{\sigma_{\mathrm{lg}}} \tag{6.17}$$

where $\Delta\rho_{\mathrm{lg}}$ is the density difference between the two phases.

The wall lubrication force is studied as a function of the relative velocity, bubble diameter and also the distance from the wall, y, presented in Figure 6.7. For the study of relative velocity and bubble diameter a constant wall distance of $y = 0.1$ mm is used.

In Figure 6.7a, it is seen that an increase in relative velocity also causes an increase in the wall lubrication force. The opposite is observed in Figure 6.7b for an increasing bubble diameter, resulting in a decreasing wall lubrication force. It is also noted that bubbles with a diameter less than $d_{\mathrm{B}} = 1$ mm show a drastic increase in the wall lubrication force.
When varying the bubble centre distance from the wall, presented in Figure 6.7c, it is observed that an increasing distance from the wall causes a decrease in the wall lubrication force. It should be noted that bubbles where $y < d_{\mathrm{B}}/2$ are physically impossible if perfect sphericity is maintained.

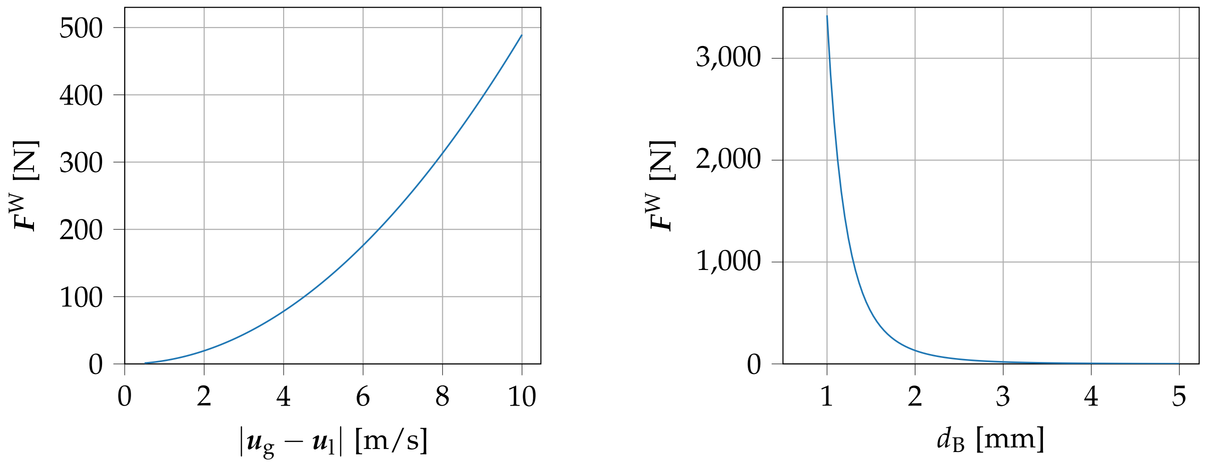

(a) The bubble diameter and distance from the wall are $d_B = 3$ mm and $y = 0.1$ mm, respectively

(b) The relative velocity and distance from the wall are $|u_g - u_l| = 2$ m/s and $y = 0.1$ mm, respectively

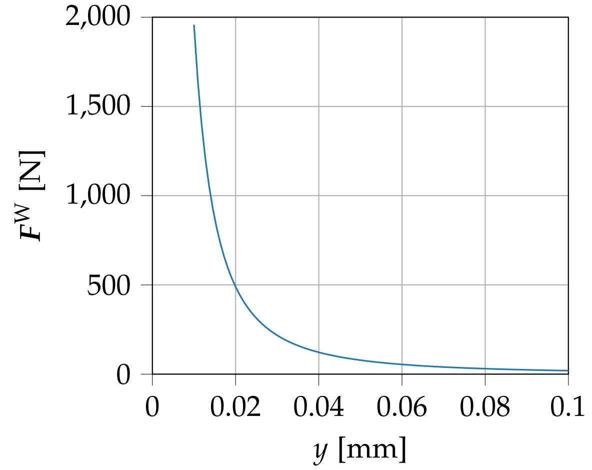

(c) The bubble diameter and relative velocity are $d_B = 3$ mm and $|u_g - u_l| = 2$ m/s, respectively

Figure 6.7: Analysis of the wall lubrication force, as proposed by Hosokawa et al. (2002), by varying the relative velocity, bubble diameter and distance from the wall.

Turbulent Dispersion Force

Turbulent dispersion (TD) occurs when the turbulence of a continuous phase has a direct effect on the particles of a disperse phase. This is usually seen as disperse particles being caught up in eddies of the continuous phase, thus being moved to regions of low concentration from regions of high concentration. This is modelled as interfacial momentum transfer due to the continuous phase velocity fluctuations. In this model, the turbulent dispersion force is modelled by the Favre averaging drag force model of Burns et al. (2004).

$$F_{lg}^{TD} = -\frac{3}{4} C_D \frac{\alpha_g}{d_B} |u_g - u_l| \frac{\mu_l^T}{\sigma_{TD}} \left(\frac{\nabla \alpha_g}{\alpha_g} - \frac{\nabla \alpha_l}{\alpha_l} \right) \tag{6.18}$$

where $\sigma_{TD} = 0.9$ is the turbulent Prandtl number and C_D is the drag coefficient, calculated in the same manner as for the drag force. A study of how varying the relative velocity and bubble diameter affects the turbulent dispersion force is presented in Figure 6.8.

Figure 6.8a shows how an increase in relative velocity results in a linearly increasing turbulent dispersion force. As the disperse bubble diameter increases, presented in Figure 6.8b, a decreasing turbulent dispersion force is seen, going towards 0 N for larger bubbles.

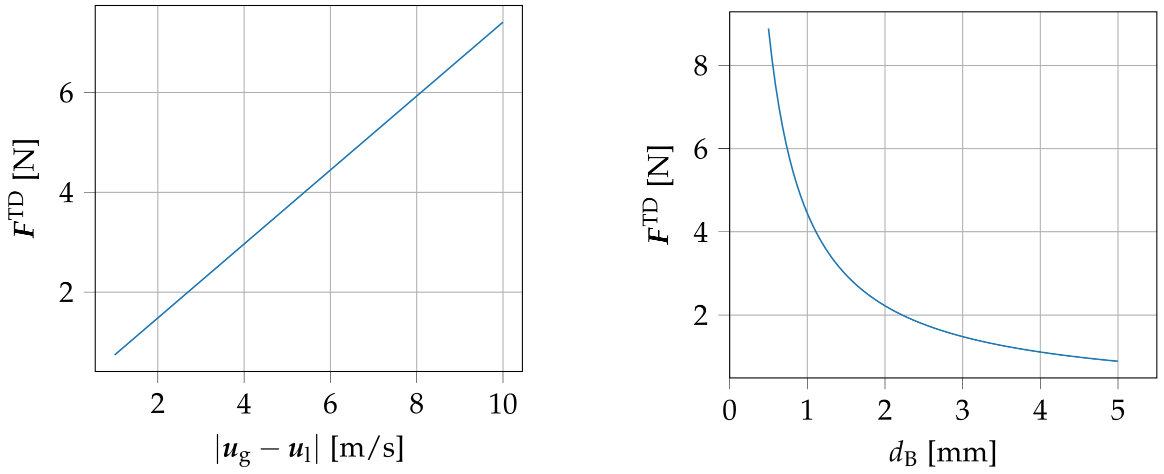

(a) For the relative velocity variation, a constant bubble diameter of $d_{\mathrm{B}} = 3$ mm is used.

(b) For the bubble diameter variation, a constant relative velocity of $|\boldsymbol{u}_{\mathrm{g}} - \boldsymbol{u}_{\mathrm{l}}| = 2$ m/s is used.

Figure 6.8: Turbulent dispersion force by Burns et al. (2004) shown for varying relative velocity and bubble diameter in (a) and (b), respectively.

Bubble-Induced Turbulence

In general two-phase flow simulations, the turbulence of the liquid phase affects various factors of the disperse phase, such as bubble breakup, coalescence etc. Conversely, the presence of bubbles will also affect the turbulence and is therefore important to model in the disperse Euler-Euler mode. This bubble-induced turbulence (BIT) is included as additional interfacial source terms in the conservation equation for the turbulent kinetic energy and turbulent dissipation. The BIT source terms S^{k}_{BIT} and $S^{\epsilon}_{\mathrm{BIT}}$ are derived from a Direct Numerical Simulation (DNS) model using Volume of Fluid of a bubble column by Ma et al. (2017).

$$S^{k}_{\mathrm{BIT}} = \min(0.18\mathrm{Re}_{\mathrm{p}}^{0.23}, 1)\boldsymbol{F}^{\mathrm{D}}_{\mathrm{lg}} \cdot \left|\boldsymbol{u}_{\mathrm{g}} - \boldsymbol{u}_{\mathrm{l}}\right| \tag{6.19}$$

$$S^{\epsilon}_{\mathrm{BIT}} = 0.3C_{\mathrm{D}}\frac{S^{k}_{\mathrm{l}}}{\tau}, \ \tau = \frac{d_{\mathrm{B}}}{\left|\boldsymbol{u}_{\mathrm{g}} - \boldsymbol{u}_{\mathrm{l}}\right|}$$

where C_{D} is the drag coefficient and τ is the chosen timescale for characterising BIT.
The source term for the ω-equation can be derived from,

$$S^{\omega}_{\mathrm{BIT}} = \frac{1}{C_{\mu}k_{\mathrm{l}}}S^{\epsilon}_{\mathrm{BIT}} - \frac{\omega_{\mathrm{l}}}{k_{\mathrm{l}}}S^{k}_{\mathrm{BIT}} \tag{6.20}$$

where C_μ is a standard model coefficient.

6.3 Resolved Mode

In the case of sufficient grid refinement, the flow structures can be resolved and the model tends towards a VOF formulation, as shown in Figure 6.9. In resolved mode, an assumption is made for the interfacial velocity u^{I}, such that the velocity of the two phases across the interface is continuous, $\boldsymbol{u}_{\mathrm{l}} = \boldsymbol{u}_{\mathrm{g}} = u^{\mathrm{I}}$. In this way, a mixture density is introduced as $\rho_{\mathrm{mix}} = \alpha_{\mathrm{l}}\rho_{\mathrm{l}} + \alpha_{\mathrm{g}}\rho_{\mathrm{g}}$ resulting in the following mass and momentum conservation equations

$$\frac{\partial \rho_{\mathrm{mix}}}{\partial t} + \nabla \cdot (u^{\mathrm{I}} \rho_{\mathrm{mix}}) = 0 \tag{6.21}$$

$$\frac{\partial (\rho_{\mathrm{mix}} u^{\mathrm{I}})}{\partial t} + \nabla \cdot (\rho_{\mathrm{mix}} u^{\mathrm{I}} u^{\mathrm{I}}) = \nabla \cdot (2\mu_{\mathrm{mix}} \boldsymbol{S}_{\mathrm{r}}) - \nabla p + \rho_{\mathrm{mix}} g + \boldsymbol{F}^{\sigma} \tag{6.22}$$

Where $\boldsymbol{F}_{\sigma}$ represents surface tension. In this way, the homogenous VOF model is recovered.

For the resolved formulation, the interfacial momentum exchange term, $\boldsymbol{f}_{\mathrm{r}}$, is described by a numerical drag formulation to ensure phase coupling between the continuous air and water. Additionally, a model is required for the surface tension and turbulence damping at the gas-liquid interface. These are described in the following sections.

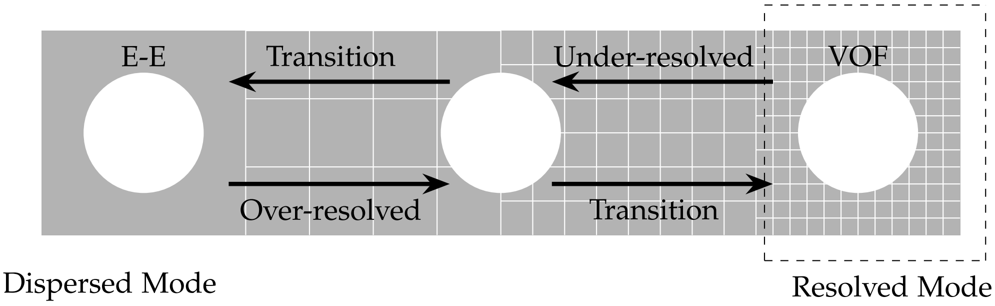

Figure 6.9: Illustration of the modelling strategy employed in the two-fluid MultiMorph model, dependent on grid refinement level. The white circles represent gas bubbles. Focusing on the resolved mode.

6.3.1 Interfacial Drag Force

In single-fluid models, where both fluids share the same velocity field, no drag force occurs. However, in multi-fluid models such as the MultiMorph model, where interface tracking is implemented, a drag term is necessary for the interfacial drag. The function of the interfacial drag is to ensure equal velocities of both fluids at the interface. This is implemented with the correlation proposed by Štrubelj and Tiselj (2011):

$$\boldsymbol{f}_\mathrm{r} = \sum \boldsymbol{f}_\mathrm{lg} = \boldsymbol{F}^\mathrm{D,i}_\mathrm{lg} = K^\mathrm{D,i}_\mathrm{lg}(\boldsymbol{u}_\mathrm{g} - \boldsymbol{u}_\mathrm{l}) \tag{6.23}$$

where the interfacial drag coefficient $K^\mathrm{D,i}_\mathrm{lg}$ is defined as

$$K^\mathrm{D,i}_\mathrm{lg} = \alpha_\mathrm{l}\alpha_\mathrm{g}\rho_\mathrm{lg}\frac{1}{\tau_\mathrm{r}} \tag{6.24}$$

where τ_r is the relaxation time and $\rho_\mathrm{lg} = (\alpha_\mathrm{l}\rho_\mathrm{l} + \alpha_\mathrm{g}\rho_\mathrm{g})/(\alpha_\mathrm{l} + \alpha_\mathrm{g})$ is the weighted density of the phase pair of liquid and gas. The relaxation time has to be several orders of magnitude smaller than the timestep. The relaxation time chosen for the air lubrication application is $\tau_\mathrm{r} = 10^{-8}\Delta t$ to ensure strong coupling. For calculating the drag of a dispersed phase submerged in a continuous phase of equal properties, a fixed drag coefficient is simply applied.

6.3.2 Surface Tension Model

To model the surface tension force in the model, $\boldsymbol{F}^\sigma$, a Continuum Surface Force (CSF) model is used, proposed by Brackbill et al. (1992). The CSF methods are commonly used in CFD due to the relative ease of implementation. The surface tension is given by:

$$\boldsymbol{F}^\sigma = \alpha_\mathrm{l}\sigma_\mathrm{lg}\kappa_\mathrm{lg}\hat{\boldsymbol{n}}_\mathrm{lg} \tag{6.25}$$

where κ_lg is the interface curvature, σ_lg is the surface tension coefficient given as $\sigma_\mathrm{lg} = 0.072$ N/m for air-water and $\hat{\boldsymbol{n}}_\mathrm{lg}$ is the unit interface normal vector. The interface curvature is given as:

$$\kappa_\mathrm{lg} = \nabla \cdot \hat{\boldsymbol{n}}_\mathrm{lg} \tag{6.26}$$

where the interface normal is calculated from the volume fraction gradient

$$\hat{\boldsymbol{n}}_\mathrm{lg} = \frac{\nabla\alpha}{|\nabla\alpha|} \tag{6.27}$$

6.3.3 Gas-Liquid Interphase Turbulence Damping

A drawback of the MultiMorph model is the overprediction of turbulence by the turbulence kinetic energy near large interfaces. Therefore, a turbulence damping method is implemented based on an expression by Frederix et al. (2018). The turbulence damping term S^ω_TDa is added to the ω-transport equation of the k-ω SST turbulence model. This term counteracts the dissipation rate destruction term $-\beta\alpha_\mathrm{l}\rho_\mathrm{l}\omega_\mathrm{l}^2$ where β is a model coefficient. The idea of this approach is thus to introduce a large wall-like turbulence damping near an interface. The turbulence-damping term is defined as:

$$S^{\omega}_{\mathrm{TDa}} = A_{\mathrm{I}}\alpha_{\mathrm{r}}\beta\rho_{\mathrm{r}}\left(\frac{\nu_{\mathrm{r}}}{\beta\delta_{\mathrm{r}}^{2}}\right)^{2} \tag{6.28}$$

with δ_{r} is the damping length scale, ν_{r} is the phase kinematic viscosity and A^{I} is an interface indicator field. The indicator field ensures, that turbulence damping is only applied near an interface, therefore A^{I} is nonzero only at an interface.
The damping length scale δ_{r} is a tuneable parameter, however, Frederix et al. (2018) recommends a value of $\delta_{\mathrm{r}} = 10^{-4}$ for most applications, which is the value used in this project.

6.4 Transition Region Methodology

Additional modelling steps are necessary for accurate VOF and Euler-Euler formulations on under-resolved and over-resolved grids respectively. Additionally, this section will describe the methodology behind the disintegration of a continuous phase to disperse morphologies and the accumulation of a disperse phase to continuous morphologies. An example two-dimensional bubble dynamics case has been done in Appendix A.1, where a further understanding of the disperse, resolved and transitional modes can be had.

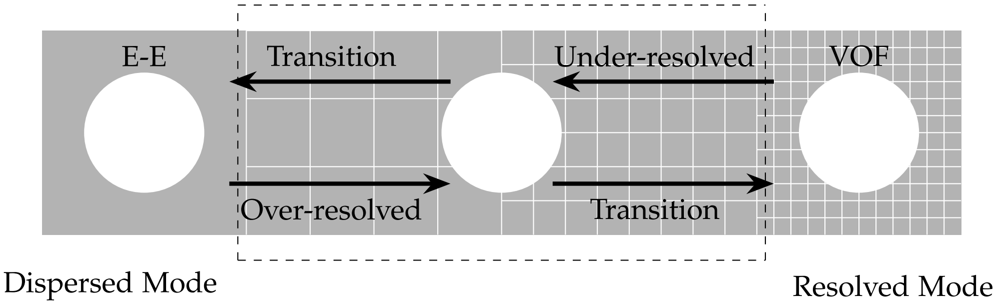

Figure 6.10: Illustration of the modelling strategy employed in the two-fluid MultiMorph model, dependent on grid refinement level. The white circles represent gas bubbles. Focusing on the transition region.

6.4.1 VOF on Under-Resolved Structures

Approximating VOF on under-resolved structures is done by implementing resolution-adaptive drag modelling, described in Meller et al. (2023). Recall that, in resolved mode, the interfacial drag between phases is modelled using the drag coefficient of Equation 6.24, from here on written as $K_{\mathrm{lg}}^{\mathrm{D,R}}$ to denote a *resolved* drag model. Problems arise, as the drag predicted by this model tends to overshoot actual values on an under-resolved grid. Comparatively, the drag model used for under-resolved structures in the Euler-Euler mode, $K_{\mathrm{lg}}^{\mathrm{D,UR}}$ for *under-resolved*, such as the one presented in Section 6.2.1 tends to undershoot values for drag. To account for this, a resolution-adaptive drag model is set up from linear interpolation as:

$$K_{\mathrm{lg}}^{\mathrm{D}} = \frac{K_{\mathrm{lg}}^{\mathrm{D,UR}} K_{\mathrm{lg}}^{\mathrm{D,R}}}{K_{\mathrm{lg}}^{\mathrm{D,UR}} + \zeta_{\mathrm{lg}}^{\mathrm{UR}} K_{\mathrm{lg}}^{\mathrm{D,R}}} \tag{6.29}$$

where $\zeta_{\mathrm{lg}}^{\mathrm{UR}}$ is an under-resolution indicator. This quantity becomes one in fully under-resolved flow, and zero in fully resolved cases. For all other cases, the indicator takes values between zero and one. Further explanation of the exact calculation of the indicator, is done in Meller et al. (2023). The authors also tested the adaptive drag modelling on a 3D rising gas bubble and in 2D stratified channel flow. For both cases, the model showed promising results on both fine and, more importantly, coarse mesh refinements.

6.4.2 Euler-Euler on Over-Resolved Structures

The Euler-Euler model is typically applied on coarse meshes with closure models for forces, where bubbles are assumed to be smaller than a cell. However, on meshes where the cells are refined to become smaller than a bubble diameter, the model tends not to converge and results in unphysical oscillations. A method is therefore needed to approximate the Euler-Euler model on over-resolved structures. In the MultiMorph model, this is done by applying a Gaussian smoothing filter to the volume fraction, as described in Krull et al. (2024). The filter parameter σ_{f} is defined based on the bubble diameter as

$$\sigma_{\mathrm{f}} = \frac{d_{\mathrm{B}}}{8} \tag{6.30}$$

such that no filtering occurs on coarse meshes with $d_{\mathrm{B}}/h \leq 1$ where h is the local cell width, defined as $h = \Delta V^{1/3}$ with V being the local cell volume. The filter gradually becomes more active on increasing diameter resolutions, d_{B}/h. The filter is realised by implementing a diffusion term in the continuity equation as

$$\frac{\partial \alpha_{\mathrm{r}} \rho_{\mathrm{r}}}{\partial t} + \nabla \cdot (\boldsymbol{u}_{\mathrm{r}} \alpha_{\mathrm{r}} \rho_{\mathrm{r}}) = \nabla \cdot (C_{\mathrm{f}} \nabla \alpha_{\mathrm{r}}) + \Gamma_{\mathrm{r}} \tag{6.31}$$

where $C_{\mathrm{f}} = \min(C_{\mathrm{f,F}}, C_{\mathrm{f,max}})$. $C_{\mathrm{f,F}}$ is the filter diffusion computed by σ and is limited by $C_{\mathrm{f,max}}$. Krull et al. (2024) tested the filtering on various cases and found that the mesh dependence was significantly decreased.

6.4.3 Accumulation of Disperse to Continuous Structures

The accumulation of disperse bubbles to continuous structures is based upon a threshold value defined by the dense packing limit of 0.74. Accumulation occurs when $\alpha_{\mathrm{r,cont}} + \alpha_{\mathrm{r,disp}} \geq \alpha_{\mathrm{r,threshold}}$

and the mass transfer is thus defined as

$$\Gamma_{\text{cont}} = \frac{\rho_{\text{r}}\sqrt{\alpha_{\text{r,disp}}}}{\tau} \tag{6.32}$$

where τ is a user-defined timescale.

6.4.4 Disintegration of Continuous to Disperse Structures

A threshold is defined for the continuous phase, such that when the local fraction of the continuous phase is $\alpha_{\text{r,cont}} < 0.75$, mass transfer to the disperse phase occurs according to

$$\Gamma_{\text{disp}} = \frac{\rho_{\text{r}}\sqrt{\alpha_{\text{r,cont}}}}{\tau} \tag{6.33}$$

where τ is a user-defined timescale. Note that, additional modelling is required such that the production of the disperse phase only occurs when the interface is conserved, else a constant production would occur in the interface region.

6.5 Numerical Model Setup

With the MultiMorph model described in the previous sections, the numerical model has to be meshed and boundary conditions applied. This, along with an averaging strategy, is defined in the following.

6.5.1 Computational Grid

Due to how the MultiMorph model switches between Euler-Euler and VOF based on, among other things, the mesh refinement, a mesh independence analysis is challenging. This is because, as the mesh refinement increases, the model will tend towards pure VOF simulations, and the accuracy will increase until all bubbles are refined sufficiently. This will increase the computational cells exponentially, thus defeating the purpose of the MultiMorph model. Therefore, no grid independence study will be done. The general meshing strategy is shown in Figure 6.11, showing a small model section along the x-direction.

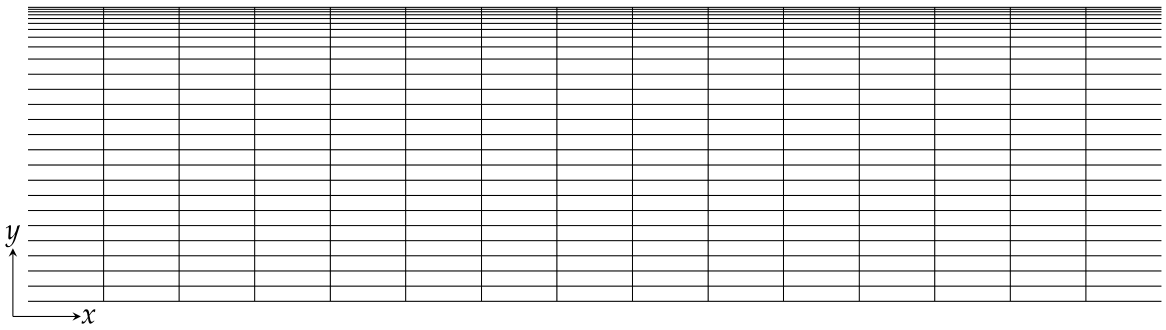

Figure 6.11: Illustration of the meshing strategy used in the numerical model for validation. The full mesh is shown in the y-direction, while only a small part of the total x length is shown

The figure shows, that the cells are graded towards the plate in the y-direction to have smaller cells where the air is present, while larger cells are acceptable in the free stream. The near-wall cells' growth ratio is 1.2 during the first 20% of the y-domain height. In the x-direction the cells are kept at a constant size. The height of the near-wall cell in the y-direction, and the length of cells in the x-direction, are presented in Tabel 6.1. This mesh will be used for the sensitivity study and validation.

Table 6.1: Key characteristics of the computational mesh used for the numerical model.

Near-wall cell height in y	Cell length in x	Total cells
1.42 mm	100 mm	20,300

6.5.2 Boundary Conditions and Initial Parameters

Table A.3 in Appendix A.2 presents the boundary conditions set for each boundary in the model. Schemes and solver settings are presented in Table A.4 and A.5 in the same appendix. In the model, the included closure models for the disperse phase are lift, drag, virtual mass, turbulent dispersion and wall lubrication. A bubble diameter also has to be defined for the disperse phase, this value will be varied in the sensitivity study but is initially set as $d_\mathrm{B} = 0.3$ mm.

6.5.3 Averaging

Due to the instability caused by turbulence and as the bubbly flow at the hull is highly transient, averaging will be used for the URANS solution. The wall shear stress of water is averaged during a period of $t_\mathrm{avg} = 12\,\mathrm{s}$, with the total simulation time being $t = 20\,\mathrm{s}$. Furthermore, to determine the drag on the hull at an exact measurement point, the wall shear stress of the water is integrated on an area 5 cm before and after the point of measuring.

7 Validation of MultiMorph Model on a Two-Dimensional Plate

As the MultiMorph model is yet to be extensively tested for the air lubrication application, this will be done by comparing the two-dimensional model with experimental data from Elbing et al. (2008). First, a sensitivity study will be performed for various model parameters to determine their impact and the model sensitivity. Afterwards, the model will be validated by comparing drag reduction data from experiments conducted by Elbing et al. (2008) on a flat plate dragged through a body of water.

7.1 Experimental Study by Elbing et al. (2008)

The data with which the MultiMorph model will be validated stems from an experiment performed by Elbing et al. (2008). The experimental setup, shown in Figure A.4, consists of a flat plate of length $X = 13$ m and width $Z = 3.05$ m with two air injector locations 1 and 2 at $X = 1.38$ m and $X = 3.73$ m respectively. Additionally, a boundary layer trip is positioned at roughly $X = 0.6$ m. The experiment was done by placing the flat plate in a large water channel while injecting air at various flow rates. Several measurement devices were implemented along the streamwise direction to measure skin friction and void fraction, while cameras were used to capture near-wall boundary layer images. The authors conducted several experiments for different injector types, plate roughness and measurement methods, presented in Table 7.1. The MultiMorph model will be compared with experiments conducted under Test 1a conditions.

Table 7.1: Different test conditions used in the experiments performed by Elbing et al. (2008).

	Model	Injector	Skin-friction measurement	Temperature (°C)
Test 1a	Smooth	Porous-plate and Slot A	Local	21.6
Test 1b	Smooth	Porous-plate	Local	27.9
Test 2a	Smooth	Slot B	Local	29.0
Test 2b	Smooth	Slot B	Local	22.0
Test 3	Smooth	Slot B	Integrated	22.2

For the sensitivity study, the data from Elbing et al. (2008) with which the model will be compared, to quantify the model sensitivity, consists of drag reduction versus air flow rate shown in Figure 7.1. The drag reduction is measured at $X - X_{\text{inj}} = 6.05$ m, where X_{inj} denotes the injection location along the plate. For this experiment, the free stream velocity is $u_{\text{w,b}} = 11.1$ m/s.

The data shows three drag reduction regions, a region of BDR where the air mostly consists of air bubbles, and the drag reduction increases almost linearly with gas flow rate, a narrow transition region with a greatly increased slope and a region of ALDR with maximum drag reduction due to a continuous air layer.

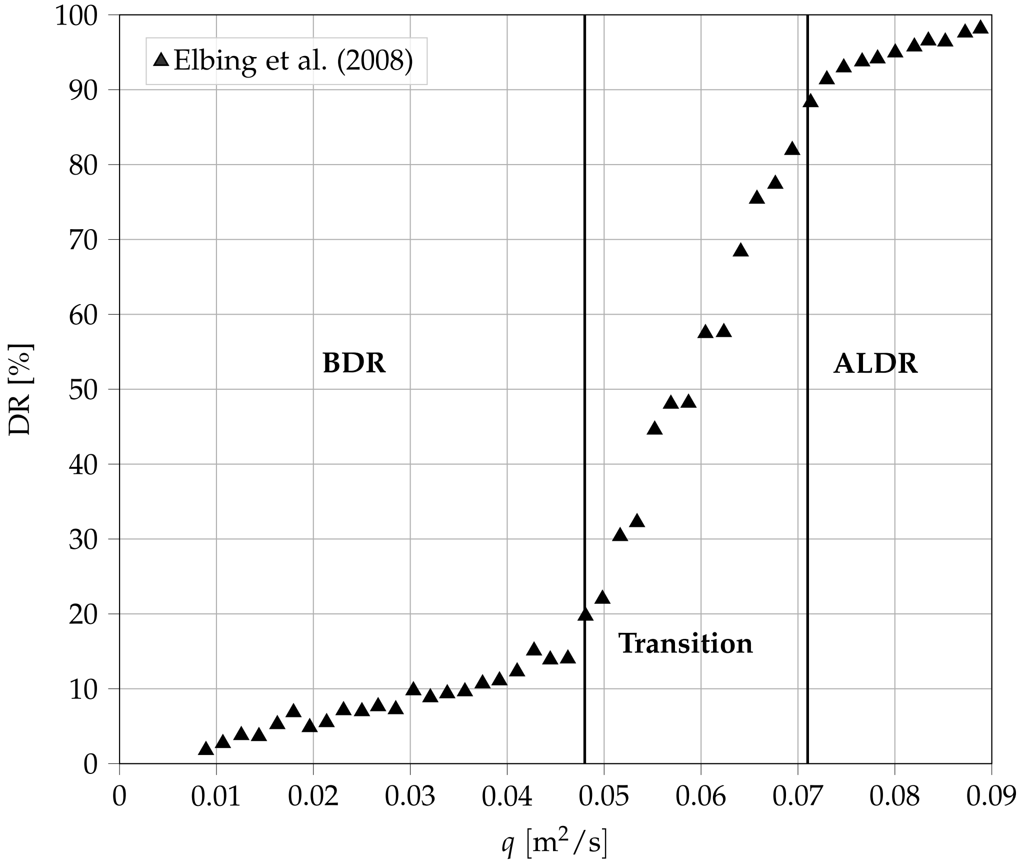

Figure 7.1: Drag reduction versus gas flow rate measurements presented in Elbing et al. (2008), used for comparison in the sensitivity study. The drag reduction is measured at $X - X_{\text{inj}} = 6.05$ m.

For validating the MultiMorph model on a two-dimensional plate, the data from Elbing et al. (2008) with which the model will be compared consists of drag reduction versus downstream distance from the injector, shown in Figure 7.2. In this way, the model will be validated on the full plate length, and the dissipation of the air layer will be taken into account. For this experiment, the free stream velocity is $u_{\text{w,b}} = 13.3$ m/s and the gas flow rate is $q = 0.056$ m^2/s, which will be matched in the model.

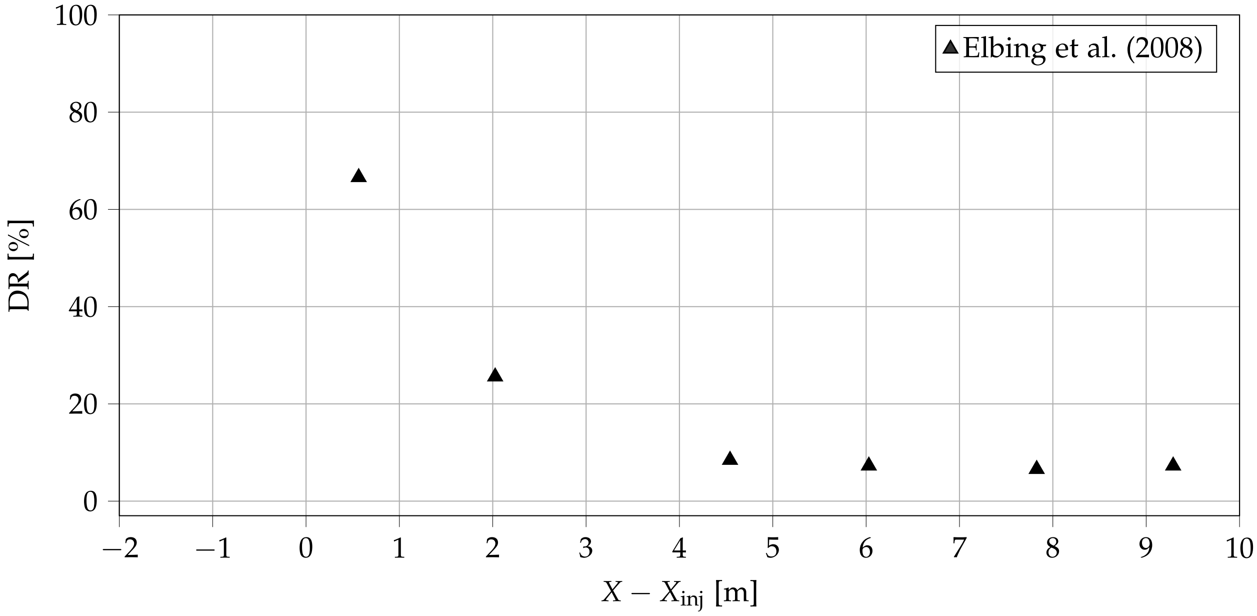

Figure 7.2: Drag reduction versus downstream distance from the injector presented in Elbing et al. (2008), used for validating the MultiMorph model.

7.2 Model Parameters for Sensitivity Study

In the MultiMorph framework, several model parameters can be tuned and implemented, to fit a specific case. In this section, a sensitivity study assesses whether the model is sensitive to the parameter variation. This study's two main parameters of interest are the turbulence intensity of water at the inlet and the disperse phase bubble diameter. Additionally, two different methods of handling the air injection into the domain are analysed.

The sensitivity study will consider drag reduction at various gas flow rates, where each parameter is tested at four different gas flow rates of $q = 0.02,\ 0.04,\ 0.06$ and $0.08\ \text{m}^2/\text{s}$.

7.2.1 Turbulence Intensity

The turbulence in the computational domain will greatly affect the air-induced drag reduction, as increased turbulence will increase the rate at which air bubbles are transported away from the wall, thus reducing the drag reduction. In the URANS k-ω SST turbulence model, the turbulence parameters, turbulence kinetic energy k and turbulence dissipation rate ω, are important to consider when providing initial- and boundary conditions. In the model, the turbulence parameters for the water and continuous air phase are calculated as:

$$k = \frac{3}{2}(I u_{\text{w,b}})^2 \tag{7.1}$$

$$\omega = \frac{\sqrt{k}}{l C_{\mu}^{0.25}}$$

where $u_{\mathrm{w,b}}$ is the bulk velocity, $C_{\mu} = 0.09$ is a model constant, l is a characteristic length scale and I is the turbulence intensity. The turbulence intensity parameter estimates the turbulence level for a given simulation, which will be varied in the sensitivity study. In general, values for the turbulence intensity can be split into three cases: low turbulence, medium turbulence and high turbulence with values of $I = 0.05\%$, $I = 1\%$ - 5% and $I = 5\%$ - 20%, respectively. Based on these estimations, the sensitivity study will test turbulence intensity values of 0.5%, 5% and 15%.

7.2.2 Disperse Phase Bubble Diameter

As the disperse bubbly flow is assumed to be monodisperse in the model framework, a constant value for the disperse phase bubble diameter has to be defined. This value is used in calculating various bubble forces, as described in 6.2.1, why the diameter greatly influences the balance of forces on a bubble. This is especially important for the lift force, where a sign change of the lift coefficient can occur with changing bubble deformation and diameter (Hessenkemper et al. 2021). In the sensitivity study, a bubble diameter of $d_{\mathrm{B}} = 0.03$ mm, $d_{\mathrm{B}} = 0.3$ mm and $d_{\mathrm{B}} = 3$ mm will be tested.

7.2.3 Slot Injector

The air injection can be handled in various ways within the model framework. Therefore it is of interest to analyse whether the exact method impacts the drag reduction. One air injection method is to recreate the air injection slot used by Elbing et al. (2008). This method is shown in Figure 7.3, where an air slot is implemented at $X = 0$ m. At the top of the slot, air in the continuous phase is input into the domain. The air injection velocity has an angle of $-12°$ to ensure flow parallel to the walls of the air injection slot.

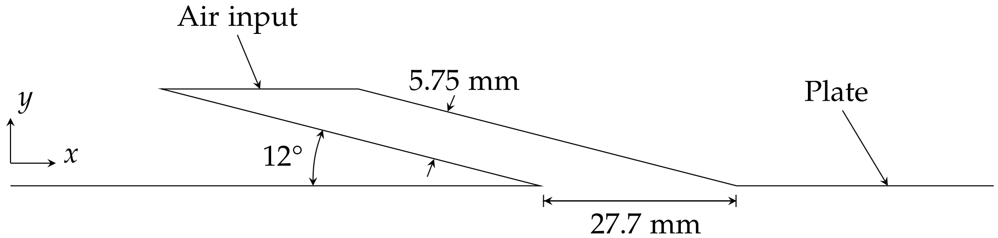

Figure 7.3: Air slot injector used in Elbing et al. (2008). The air is injected as a continuous phase. The figure is not to scale.

A visualisation of the presence of air in the domain using the air slot injection method is shown in Figure 7.4, with a gas flux of $q = 0.04$ m^2/s. It is seen how as air enters the free stream, the air becomes present downstream of the slot injector in the near wall region.

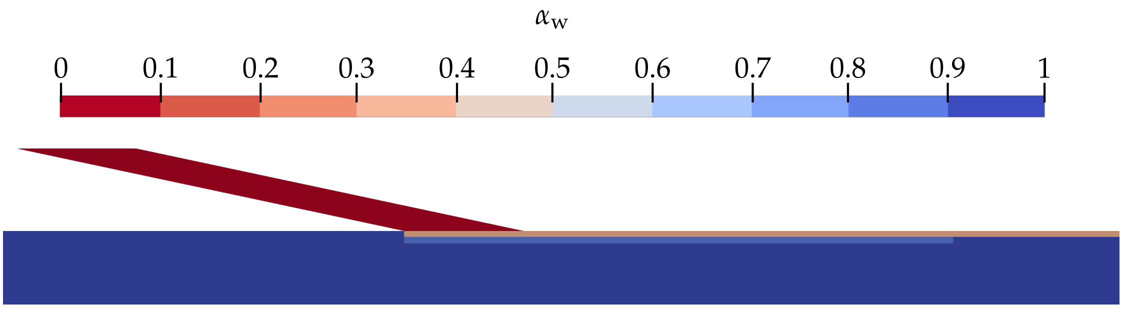

Figure 7.4: Visualisation of the air slot injector. Only a small part of the domain x-length and y-height is shown.

7.2.4 Mass Source Air Injection

Another air injection method is by utilising point mass sources, which applies a mass source term to the continuity equation and all field equations, in a defined set of computational cells. An advantage of the point mass source injection method is the flexibility of the exact injection location, it allows for. Additionally, no additional geometry changes are needed for the numerical model, as is the case for the slot injector. This model implements the mass source across several points, where the total mass flow rate is divided across the points. The points used for the mass source are set 5 mm along the x-direction with the first point being at $X - X_{\text{inj}} = 0$ m, in the first near-wall computational cell. This ensures, that the air injection occurs right at the wall. To ensure mass conservation, an identical mass of water is removed from the domain when the air injection occurs. The method is shown in Figure 7.5, illustrating how the points for mass source injection are implemented.

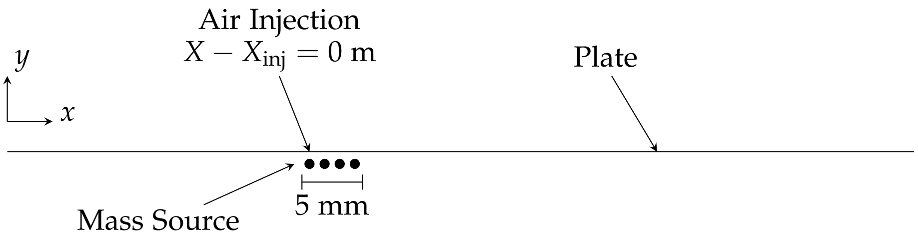

Figure 7.5: Illustration of mass source air injection method. The points used for mass source are shown as black circles. The figure is not to scale.

Figure 7.6 shows an example of the mass source air injection method for an air flow rate of $q = 0.04$ m^2/s. The figure illustrates, how the air enters the domain in the near-wall region and an air layer forms immediately downstream, like was seen in the slot injector.

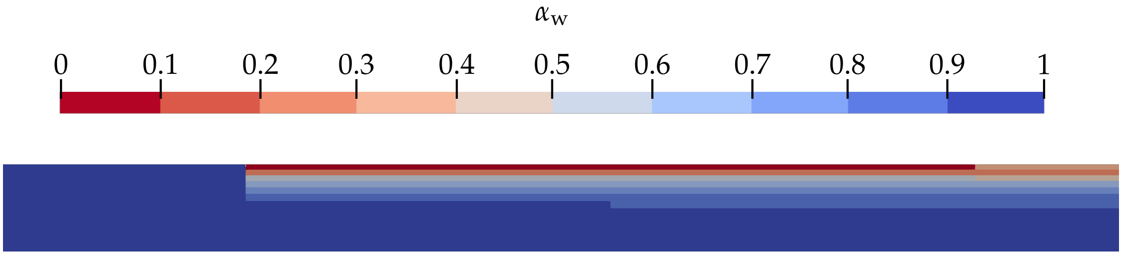

Figure 7.6: Visualisation of the mass source air injection method. Only a small part of the domain x-length and y-height is shown.

7.3 Sensitivity Study of Air Slot Injector

This section presents the sensitivity study of the air slot injector method. Figure 7.7 shows the drag reduction versus gas flow rate for the three cases of varying turbulence intensity. For this analysis, a constant disperse bubble diameter of $d_B = 0.3$ mm has been used. The figure shows, that for turbulence intensity of $I = 5\%$ and $I = 15\%$, little to no difference is observed in the drag reduction, however, in the low turbulence case of $I = 0.5\%$, the drag reduction differs slightly at $q = 0.04\,\mathrm{m^2/s}$ and more significantly at $q = 0.06\,\mathrm{m^2/s}$. This indicates, that for higher turbulence, the rate of air transportation away from the wall increases, causing the transition from BDR to ALDR to occur at a higher gas flow rate.

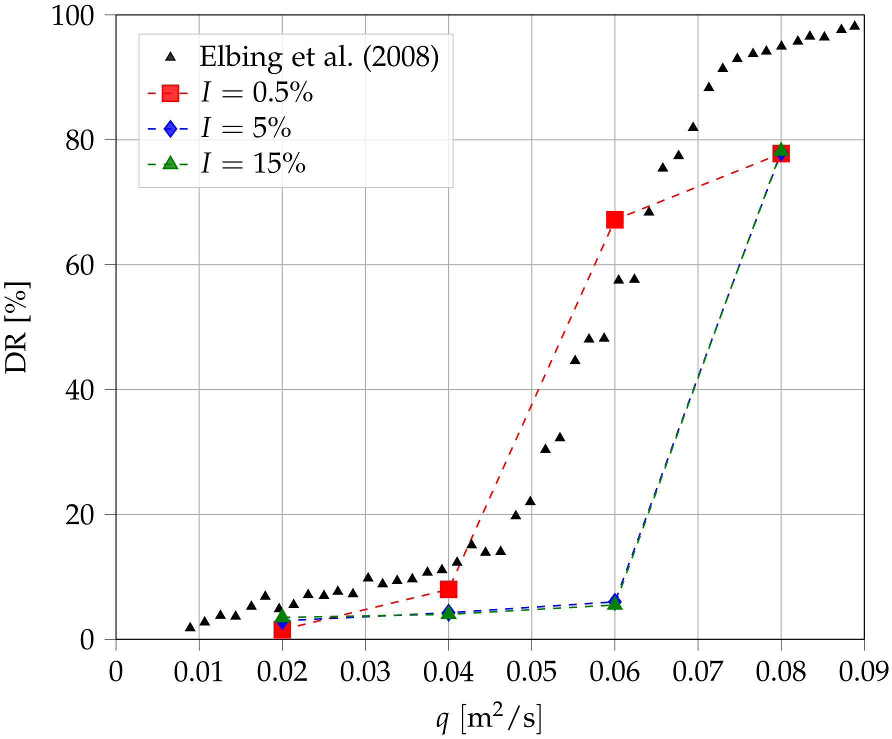

Figure 7.7: Drag reduction versus gas flow rate for the air slot injector and experimental data, at three different values for turbulence intensity. A constant bubble diameter of $d_B = 0.3$ mm is used.

For the disperse bubble diameter sensitivity analysis, a constant turbulence intensity of $I = 0.5\%$ will be used. Figure 7.8 shows the drag reduction versus gas flow rate for the three cases of varying bubble diameter. In general, the results of a bubble diameter of $d_B = 0.03$ mm varies significantly from the two other diameters considered, especially for low gas flow rates, which reside in the BDR regime. The results show that the model is more sensitive to the diameter variation in the BDR regime, as the air largely consists of disperse bubbles. For large gas flow rates, the bubble diameter has less influence on the drag reduction, as the air is generally in the continuous phase and the bubble forces are resolved on the grid. For bubble diameters of $d_B = 0.3$ mm and $d_B = 3$ mm, the drag results are mostly similar showing that the model is most sensitive to very low values for the bubble diameter.

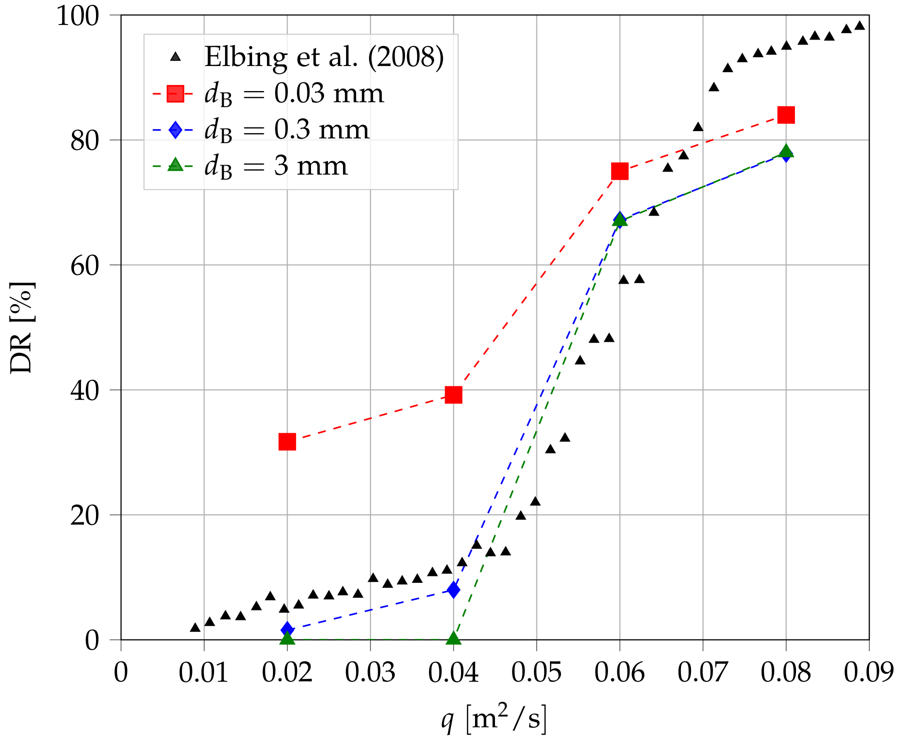

Figure 7.8: Drag reduction versus gas flow rate for the air slot injector and experimental data, at three different values for disperse bubble diameter. A constant turbulent intensity of $I = 0.5\%$ is used.

7.4 Sensitivity Study of Mass Source Air Injection

In this section, a sensitivity study is done on the turbulence intensity and the disperse phase bubble diameter, using the mass source air injection method described in Section 7.2.4. The turbulence intensity variation is presented in Figure 7.9 showing that this parameter only has a small impact on the drag reduction. In the BDR region, the turbulence intensity of $I = 0.5\%$ shows a slightly higher drag reduction than the higher turbulence intensity simulations. However, in both the transition and ALDR regions, all three cases provide very similar drag reduction. In general, the drag reduction is insensitive to turbulence intensity variations for the mass source air injection method.

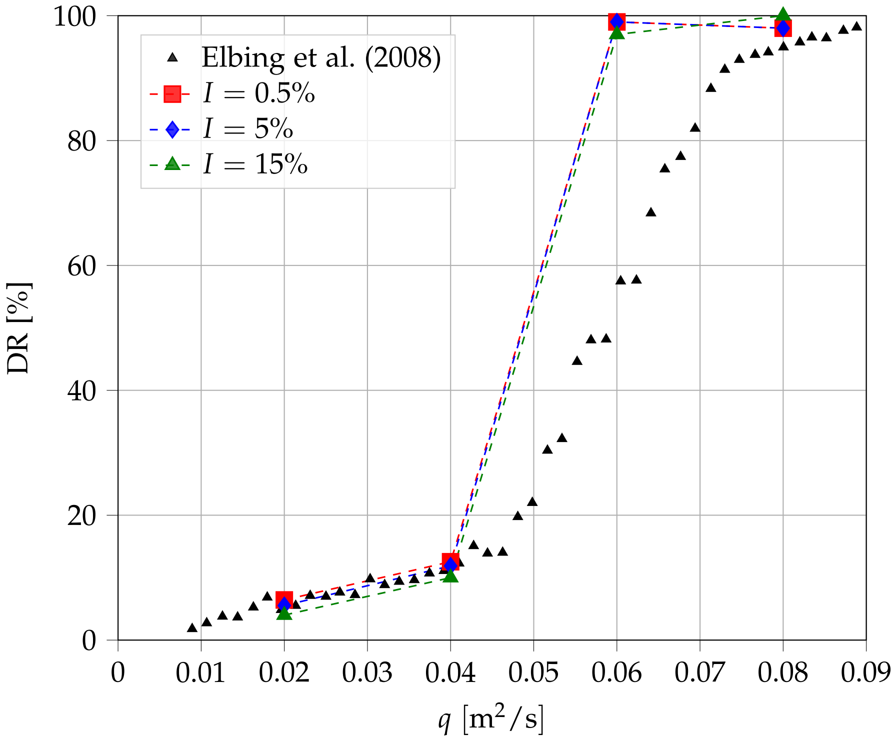

Figure 7.9: Drag reduction versus gas flow rate for the mass source injection method and experimental data, at three different values for turbulence intensity. A constant bubble diameter of $d_\mathrm{B} = 0.3$ mm is used.

The sensitivity analysis of the disperse bubble diameter is presented in Figure 7.10 with a constant turbulence intensity of $I = 0.5\%$. The study shows how, like was the case for the slot injector, very small bubbles with a diameter of $d_\mathrm{B} = 0.03$ mm vary significantly from larger bubble diameters at low gas flow rates in the BDR region, but provide similar drag reduction at higher gas flow rates in the ALDR region. Additionally, no significant change in the simulation results occurs between the two larger bubble diameters of $d_\mathrm{B} = 0.3$ mm and $d_\mathrm{B} = 3$ mm.

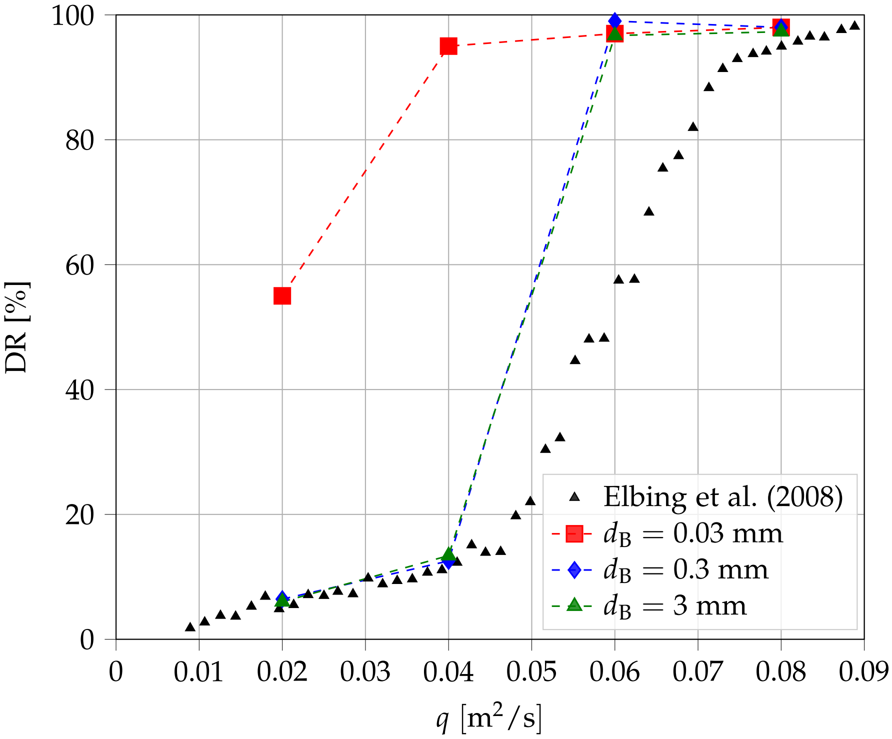

Figure 7.10: Drag reduction versus gas flow rate for the mass source injection method and experimental data, at three different values for disperse bubble diameter. A constant turbulence intensity of $I = 0.5\%$ is used.

7.5 Concluding Remarks of Sensitivity Study

Based on the sensitivity study, values for the turbulence intensity and disperse bubble diameter must be defined before validating the 2D model with experimental results. For the disperse bubble diameter, the model showed to be insensitive to diameters above $d_B = 0.3$ mm, although for $d_B = 0.03$ mm, a significant impact on the drag reduction occurred. Measurements by Elbing et al. (2008) also showed that bubbles generally had a diameter in the order of 0.2 mm to 0.4 mm, additionally bubbles in the order of $d_B = 0.03$ mm, is not expected to dominate the bubbly flow, why a bubble diameter of $d_B = 0.3$ mm is chosen for further analysis and validation. The turbulence intensity was shown to have a lesser impact on the drag reduction results, so an intensity level of $I = 0.5\%$ is defined. The air injector methods showed similar results, with both methods being able to predict the three drag reduction regimes. Therefore, to further compare the methods, both will be considered for the 2D validation.

7.6 Validation of Two-Dimensional MultiMorph Model

With the previous model parameters defined in the sensitivity study, the 2D model will be validated by comparing experimental data by Elbing et al. (2008) for drag reduction along the plate

length with simulated data. This is done, to ensure the model's accuracy on the full plate, whereas the sensitivity study only considered drag reduction on a small area. Once again, the comparison will be made for both the mass source injection method and the slot injector.
The numerical model is unchanged, however, the flow conditions are set to match that of the experiment. A freestream velocity of $u_{\mathrm{w,b}} = 13.3$ m/s and gas volume flow rate of $q = 0.056$ m^2/s is used. At these flow conditions, the drag reduction is in the BDR regime.

Figure 7.11 presents the drag reduction versus downstream distance from the injector, such that $X - X_{\mathrm{inj}} = 0$ is at the point of air injection. The mass source and slot injector are shown in Figure 7.11a and 7.11b, respectively.

Both methods show the same tendency, with the drag reduction peaking immediately downstream of the air injection point before decreasing further downstream, as the turbulence and mixing transports the air away from the wall. However, there are still clear differences between the two air injection methods, as the slot injector is seen to undershoot the drag reduction at all points along the plate. Compared with the mass source injection method, the simulated data follows the experimental data with higher accuracy at $X - X_{\mathrm{inj}} = 0.6$ m and $X - X_{\mathrm{inj}} = 2$ m although this method also seems to overpredict the drag reduction slightly further downstream of the injector.

Based on the validation, air injection using the mass source method is seen to predict the drag reduction along the plate with the most accuracy. Additionally, this air injection method was able to capture the different air lubrication regimes in the drag reduction over a range of gas flow rates, as presented in the sensitivity study. As the mass source method also allows for the easiest implementation within the numerical model, this method is used for further analysis.

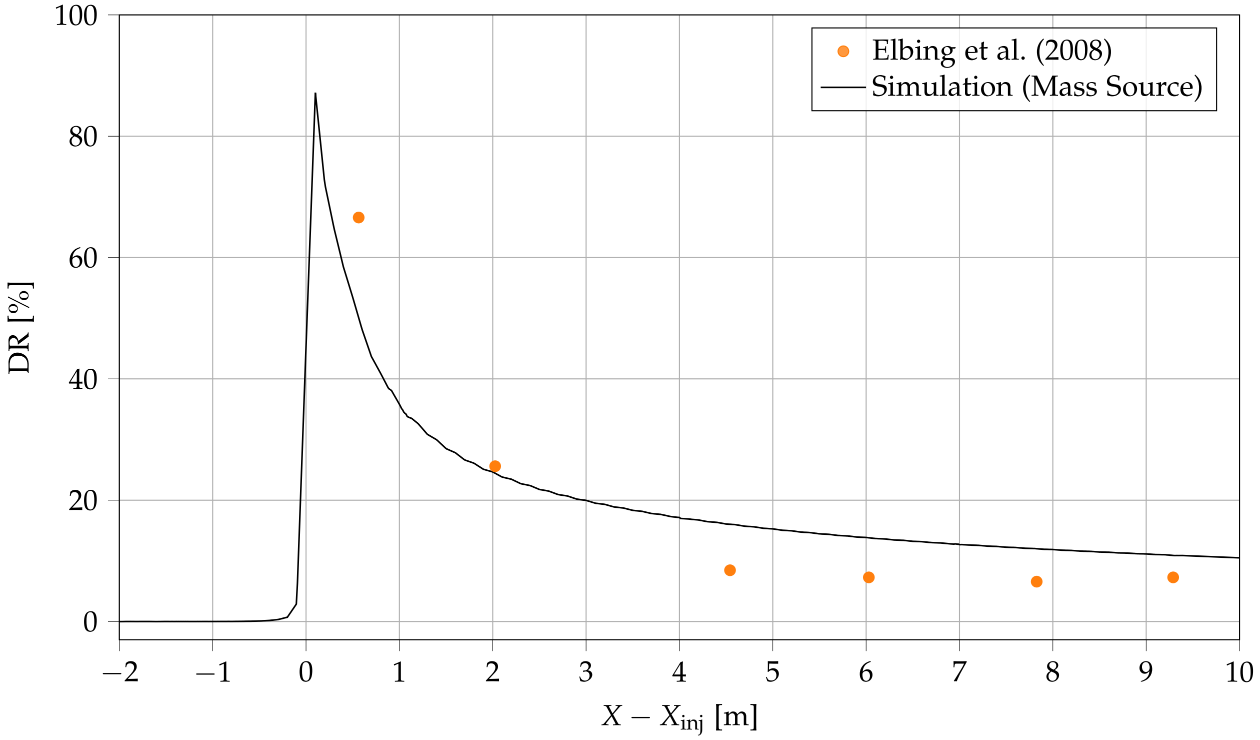

(a) Simulated data is given for the mass source injector.

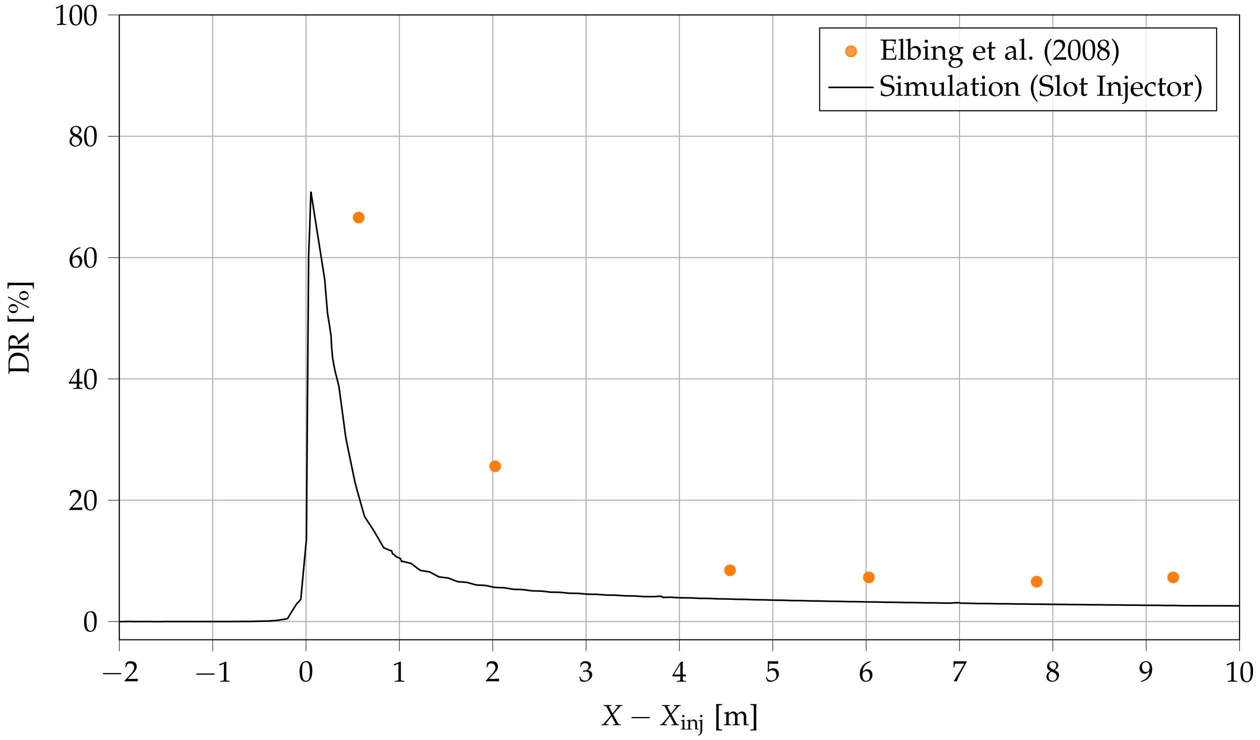

(b) Simulated data is given for the slot injector.

Figure 7.11: Comparison of drag reduction versus downstream length of injector ($X - X_{\text{inj}}$) between experimental data of Elbing et al. (2008) and simulated data. Flow conditions of $u_{\text{w,b}} = 13.3$ m/s and $q = 0.056$ m^2/s are used.

7.6.1 Conclusion of MultiMorph Model for 2D Air Lubrication

Based on both the sensitivity study and the previous validation, the MultiMorph model is demonstrated to be able to predict the air lubrication drag reduction with high accuracy, for the case of a simple two-dimensional application. Importantly, these results are obtained for a relatively coarse mesh, which thereby results in short simulation times, especially when compared with other methods, such as VOF, which require significantly more grid refinement. The MultiMorph framework is therefore proven to be a low-cost, in terms of computational time, and highly accurate model for modelling air lubrication, and serves as a good candidate for large-scale ship modelling.

8 Analysis of Air Lubrication Under Varying Conditions

As the MultiMorph framework has shown to provide accurate results for the air lubrication application, various air lubrication conditions will be analysed. For air lubrication on full-size ships, analyses of drag reduction on rough surfaces and how maintaining a continuous air layer by implementing multiple injectors is important. These cases and further study of how the near-wall boundary layer develops for the BDR and ALDR air lubrication regimes are considered in the following sections.

8.1 Analysis of Boundary Layer in the BDR and ALDR Regimes

This section will analyse how the presence of bubbles impacts how the boundary layer develops, and the velocity profile in the boundary layer. This is analysed for the case of mass source injection, a bubble diameter of $d_\mathrm{B} = 0.3$ mm and turbulent intensity of $I = 0.5\%$, to match that of the validation.

Figures 8.1 and 8.3 show the normalised streamwise velocity profile and water volume fraction of the first 5 cm in the wall-normal direction for a gas flow rate of $q = 0.04$ m^2/s and $q = 0.08$ m^2/s, respectively. The gas flow rates are chosen, to analyse the boundary layer in both the BDR (0.04 m^2/s) and ALDR (0.08 m^2/s) air lubrication regimes. The normalised streamwise velocity is shown for the multiphase simulation denoted as 2P, and for a reference singlephase water simulation denoted as 1P. The analysis is done at three downstream locations of $X - X_\mathrm{inj} = 0.5$ m, $X - X_\mathrm{inj} = 3$ m and $X - X_\mathrm{inj} = 8$ m to show how the boundary layer develops. Air is injected at $X - X_\mathrm{inj} = 0$ m. Additionally, Figures 8.2 and 8.4 show the water volume fraction in the near-wall region for the three plotted locations.

8.1.1 Boundary Layer Analysis in the BDR Regime

Figure 8.1 shows that immediately downstream of the injector at $X - X_\mathrm{inj} = 0.5$ m, there is a large presence of air in the boundary layer, as the water volume fraction reaches $\alpha_\mathrm{w} \approx 0.5$. As a result, the largest drag reduction is seen for this location, as was also found in the validation of Section 7.6. Further downstream, the volume fraction of water increases, as the air is transported away from the near-wall region, thus the drag reduction decreases. The same tendency is illustrated in Figure 8.2, which shows how the volume fraction of water increases downstream of the air injection point.

It is also evident from the Figure, that no continuous air layer has formed, as the water volume fraction does not decrease below $\alpha_\mathrm{w} \approx 0.5$, indicating that the air layer consists of a mixture of air bubbles and water, as is expected in the BDR regime. This is likely due to the turbulent dispersion force and turbulence which ensures mixing between the two phases, and thus a continuous air layer is unable to form. The boundary layer velocity profiles between the multiphase and single-phase simulations are also seen to be mostly similar, meaning that the air bubbles have a negligible effect on the velocity profile.

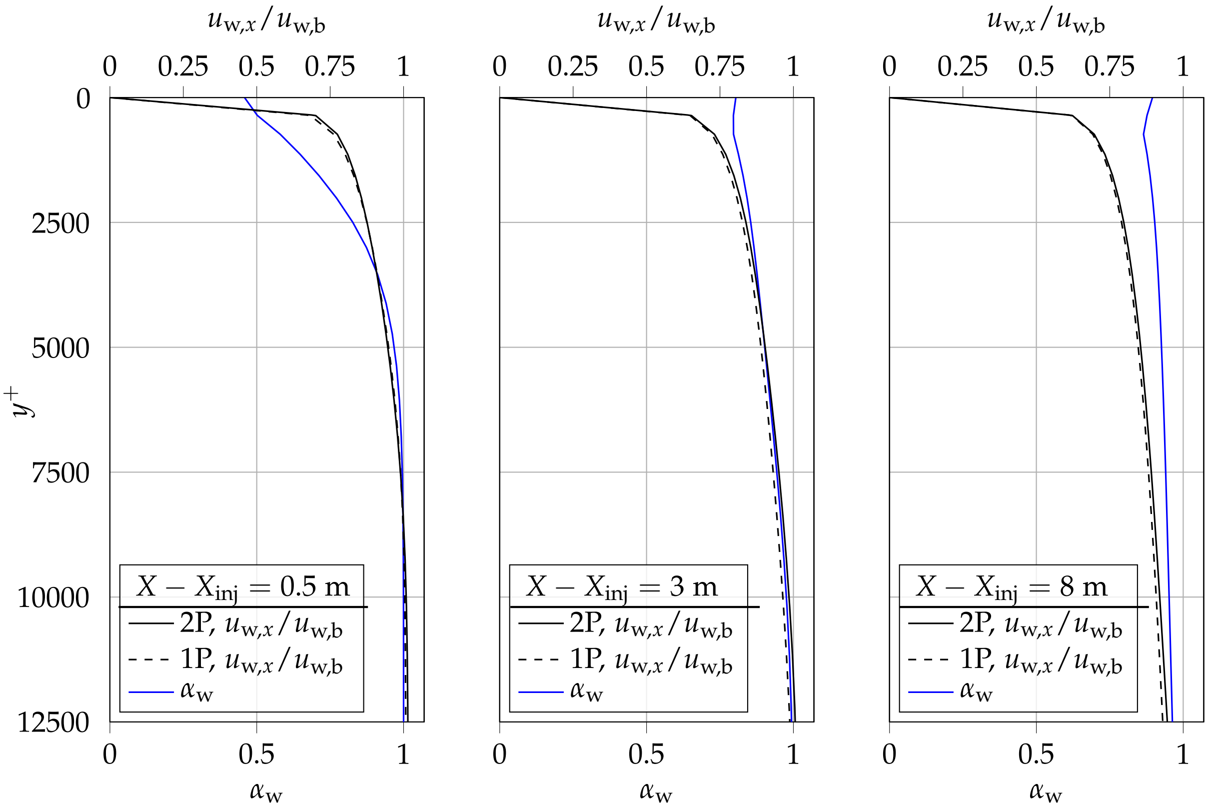

Figure 8.1: Normalised streamwise velocity and water volume fraction for the first 5 cm in the wall-normal direction at $q = 0.04$ m^2/s. 2P denotes multiphase simulations, while 1P denotes a reference singlephase simulation for water. The leftmost figure shows the analysis at $X - X_\mathrm{inj} = 0.5$ m, middle at $X - X_\mathrm{inj} = 3$ m and rightmost figure at $X - X_\mathrm{inj} = 8$ m.

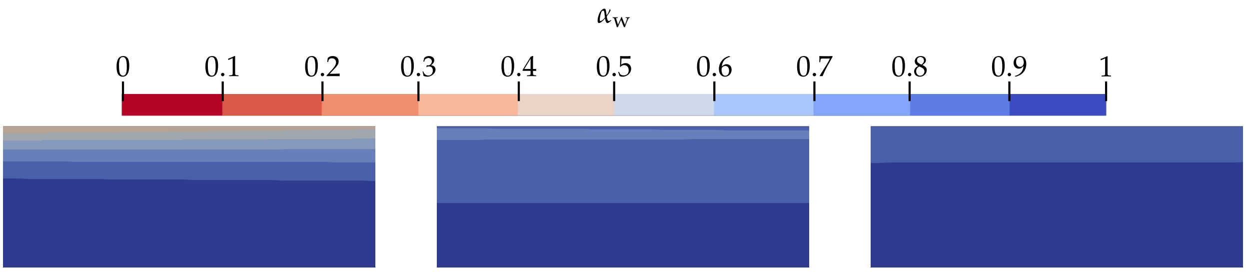

(a) $X - X_\mathrm{inj} = 0.5$ m

(b) $X - X_\mathrm{inj} = 3$ m

(c) $X - X_\mathrm{inj} = 8$ m

Figure 8.2: Volume fraction of water, α_w, in the near-wall region for $q = 0.04$ m^2/s, at three downstream lengths.

8.1.2 Boundary Layer Analysis for ALDR Regime

In Figure 8.3, where the gas flow rate is doubled, a continuous air layer is visibly formed, as the water volume fraction reaches $\alpha_w = 0$ immediately adjacent to the wall. This is also clearly evident in Figure 8.4, showing the water volume fraction in the near-wall region. Additionally, the continuous air layer thickness is seen to decrease when comparing the water volume fraction at $X - X_{inj} = 0.5$ m and $X - X_{inj} = 3$ m. However, the volume fraction does not increase noticeably from $\alpha_w = 0$, indicating that the air layer, and thus the drag reduction remains consistent along the plate. This was also seen by Elbing et al. (2008), where for the ALDR regime, the drag reduction remained constant along the plate length.

The boundary layer velocity profile is also seen to be affected by the continuous gas layer. Compared with the single-phase reference case, the boundary layer thickness is reduced with the air layer present at $X - X_{inj} = 3$ m and $X - X_{inj} = 8$ m. This is likely due to the dynamic viscosity decreasing in the boundary layer due to the presence of air.

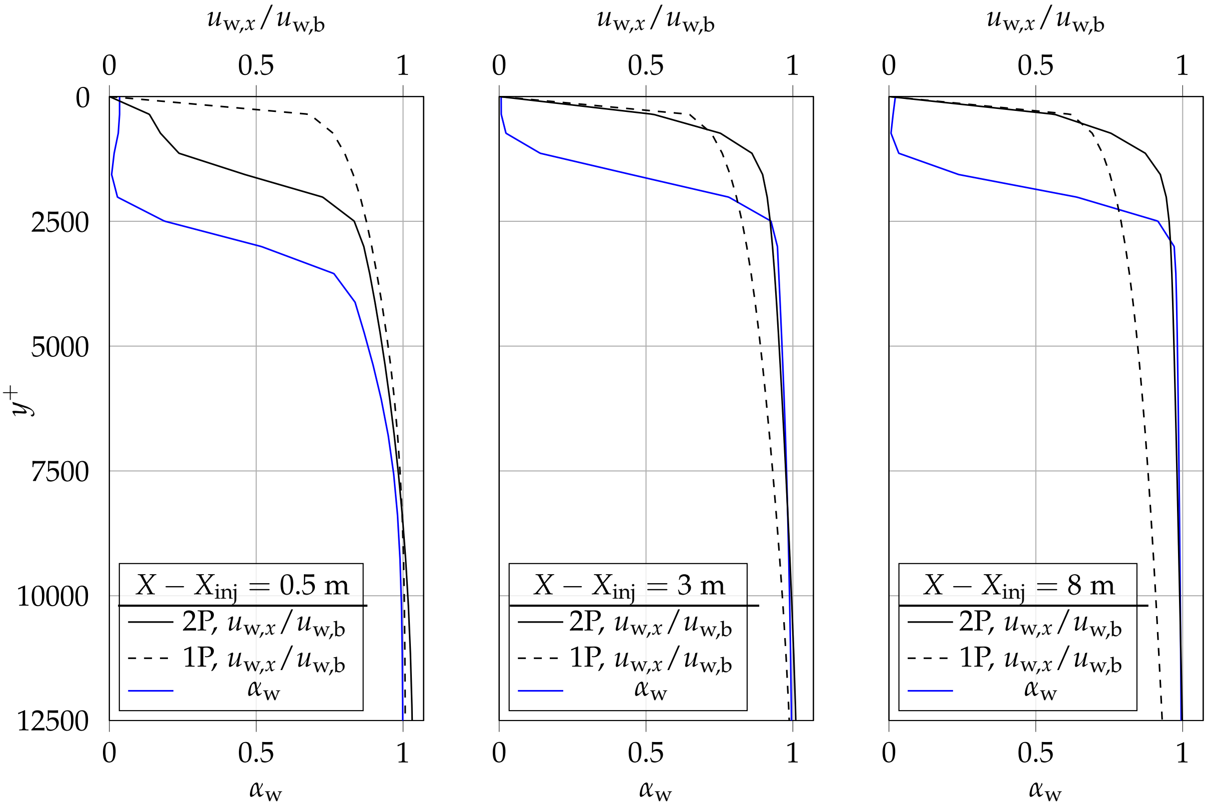

Figure 8.3: Normalised streamwise velocity and water volume fraction for the first 5 cm in the wall-normal direction at $q = 0.08$ m^2/s. 2P denotes multiphase simulations, while 1P denotes a reference singlephase simulation for water. The leftmost figure shows the analysis at $X - X_{inj} = 0.5$ m, middle at $X - X_{inj} = 3$ m and rightmost figure at $X - X_{inj} = 8$ m.

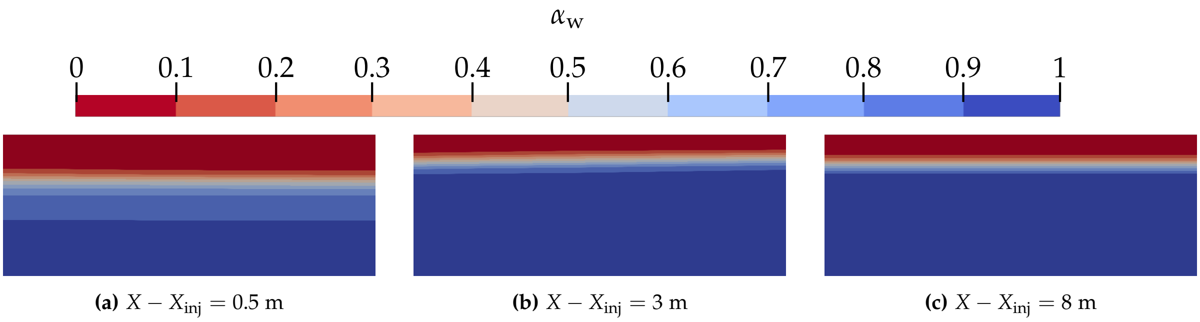

(a) $X - X_{\mathrm{inj}} = 0.5$ m **(b)** $X - X_{\mathrm{inj}} = 3$ m **(c)** $X - X_{\mathrm{inj}} = 8$ m

Figure 8.4: Volume fraction of water, α_{w}, in the near-wall region for $q = 0.08$ m^2/s, at three downstream lengths.

8.2 Surface Roughness

Until this point, the plate upon which the drag reduction is measured has been assumed to be a perfectly smooth surface. For real-world applications, such as air lubrication used for large-scale ships, the hull can not be assumed to be a smooth surface, so surface roughness must be considered. To achieve a smoother surface, ships are usually painted, however, as the paint breaks down due to mainly fouling, the surface roughness will increase (Visscher 1928). Seok and Park (2020) found that, typically, the roughness will increase by 40 µm/year due to fouling, thus an analysis will be done by comparing drag reduction and air layer persistence along the two-dimensional plate for a perfectly smooth surface and varying roughness.

The analysis is done for the same numerical model setup and flow conditions of the validation in Section 7.6 with bulk velocity and gas flow rate of $u_{\mathrm{w,b}} = 13.3$ m/s and $q = 0.056$ m^2/s, respectively. In the numerical framework, wall roughness is modelled by applying a wall constraint on the turbulent viscosity, when using wall functions, based on the turbulent kinetic energy k. The equivalent sand-grain roughness approach, described in Section 4.3.1, will be utilised to model the roughness of the flat plate, using the arithmetic mean roughness. In this way, the surface roughness will not directly affect the air bubbles, as the actual surface roughness is not resolved. Instead, the modelled equivalent sand-grain roughness will affect the flow field and turbulence in the near-wall region, thus indirectly affecting the air layer and bubbles.

The analysis will be done for a fully uniform and strongly non-uniform surface roughness, at two different surface roughness heights. The four cases are presented in Table 8.1. Additionally, the cases will be compared with the results of a perfectly smooth wall, with $\epsilon = 0$.

Table 8.1: Overview of the four different surface roughness conditions to be tested. R_a denotes the actual arithmetic mean surface roughness height, and ϵ denotes the equivalent sand-grain roughness height.

	R_am [μm]	ϵ [μm]	C_s
Case 1	100	586	0.5
Case 2	200	1173	0.5
Case 3	100	586	1
Case 4	200	1173	1

8.2.1 Drag Reduction

Figure 8.5 presents the drag reduction versus downstream distance from the injector for the case of uniform and non-uniform surface roughness in (a) and (b), respectively, for a smooth wall and two surface roughness heights. The average difference in drag reduction, presented in percentage points, between the smooth wall and the various surface roughness cases is also shown in Table 8.2. The percentage point difference $\Delta\mathrm{DR}$ is found by the difference in the mean drag reduction of each case, from the point of air injection at $X - X_\mathrm{inj} = 0$ until $X - X_\mathrm{inj} = 10$ m, for a given surface roughness as:

$$\Delta\mathrm{DR} = \overline{\mathrm{DR}}_\mathrm{smooth} - \overline{\mathrm{DR}}_\mathrm{rough} \tag{8.1}$$

The figure shows that independent of roughness uniformity, introducing surface roughness of $R_\mathrm{a} = 100$ μm at the wall will decrease the drag reduction substantially. Furthermore, doubling the surface roughness only reduces the drag reduction by 0.6%pt. for both cases of roughness uniformity. Comparing the uniform and non-uniform roughness, little difference is seen, although the non-uniform roughness results in slightly lower drag reduction.

Table 8.2: Overview of drag reduction difference, in percentage points, between the four cases of surface roughness and a smooth wall.

	Case 1	Case 2	Case 3	Case 4
ΔDR [%pt.]	3.5	4.1	4.1	4.7

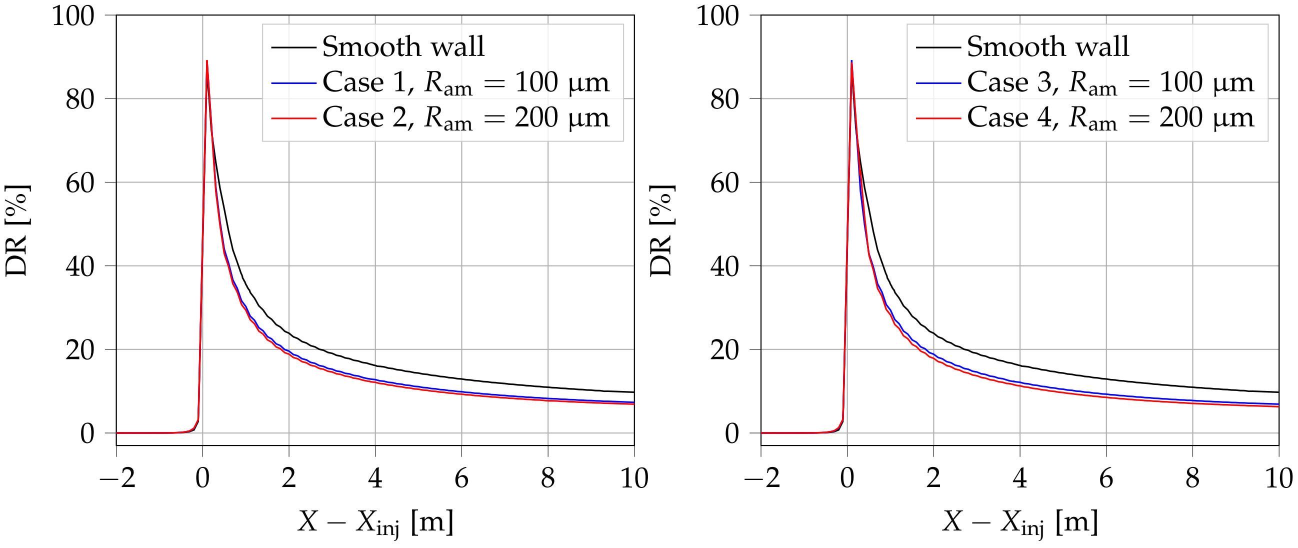

(a) Uniform surface roughness of $C_s = 0.5$.

(b) Strongly non-uniform surface roughness of $C_s = 1$.

Figure 8.5: Drag reduction versus downstream distance of the injector for a smooth plate and two values for surface roughness. A uniform and non-uniform surface roughness is presented in (a) and (b), respectively.

To analyse the decrease in drag reduction seen as a result of surface roughness, the turbulent kinetic energy of the water phase, k_{w} and volume fraction of the disperse air phase, α_{airD} in the first near-wall cell is presented in Figure 8.6. The analysis is done for a smooth wall, shown as the dashed lines, and for the rough wall of Case 4, shown as the full lines.

From the figure, it is clear that for a rough wall, the volume fraction of disperse air is noticeably reduced compared with the smooth wall, meaning fewer bubbles are present in the near-wall region, which likely explains the decrease in drag reduction. The decrease of air bubbles in the near-wall region can be explained by considering the turbulent kinetic energy, shown in red in the figure. For the case of surface roughness, the turbulent kinetic energy is seen to be increased by a factor of roughly three along the plate length. As the turbulence is modelled through a k-ω SST model, an increase in turbulent kinetic energy will also increase the eddy viscosity. The eddy viscosity is an important parameter in the calculation of the turbulent dispersion force, where a larger TD force occurs for increasing eddy viscosity, thus the dispersion of air from the near-wall region is larger.

Additionally, the turbulent kinetic energy is greatly increased for the rough wall immediately downstream of the injector. This also indicates that the transition from a laminar to a turbulent boundary layer occurs further downstream for the smooth wall. The surface roughness therefore results in increased turbulence in the boundary layer, which increases air transport away from the wall.

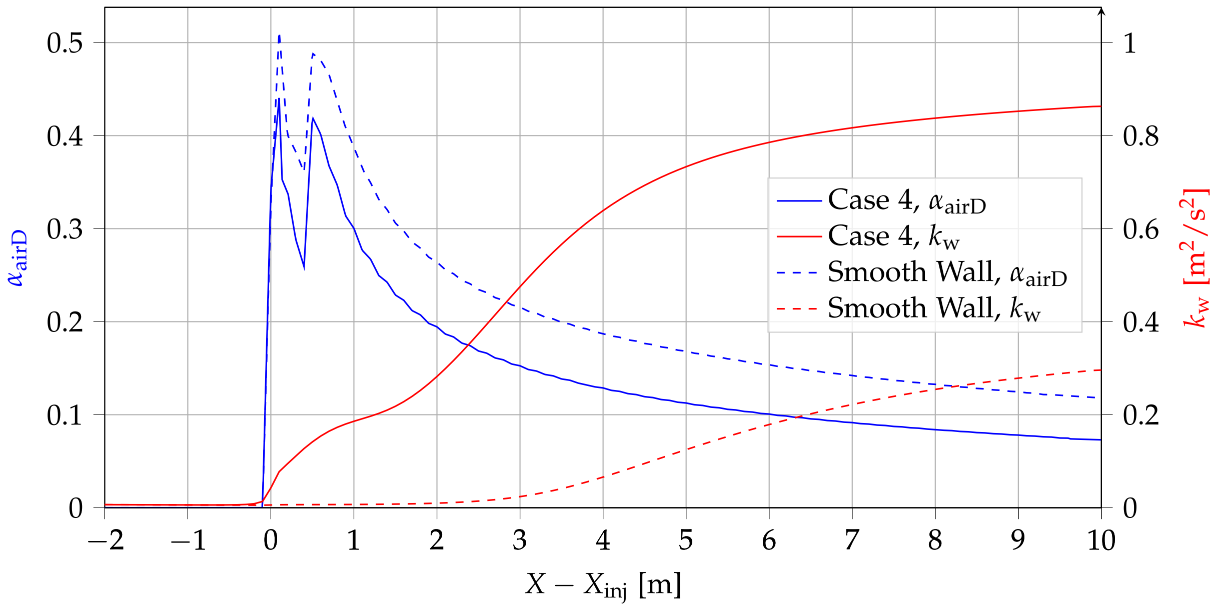

Figure 8.6: Turbulent kinetic energy of the water phase, k_{w} shown in red and volume fraction of the disperse air phase, α_{airD} shown in blue in the near-wall region along the plate length. The analysis is done for a smooth wall and Case 4 with a non-uniform surface roughness of $R_{\mathrm{am}} = 200\ \mu$m.

8.3 Additional Air Injectors

As seen in previous analyses, the air layer, and thus the drag reduction, tends to dissipate quickly for the BDR regime. Already at $X - X_{\mathrm{inj}} = 2$ m the drag reduction is reduced to roughly 20%, from a peak of roughly 85%. The same phenomenon, though at a larger scale, will occur for air lubrication on full-scale ships, as the air layer will dissipate both due to turbulence and mixing, and on the sides of the hull. Therefore, there is a need for multiple air injector locations to sustain the air layer and a high drag reduction.

A second injector location will be implemented for the two-dimensional case to analyse how this affects the air layer. The second injector will be tested at three different downstream locations of $X - X_{\mathrm{inj}} = 2$ m, $X - X_{\mathrm{inj}} = 4$ m and $X - X_{\mathrm{inj}} = 6$ m. The flow conditions will mimic that of previous analyses with $u_{\mathrm{w,b}} = 13.3$ m/s and $q = 0.056$ m^2/s. The second injector will inject air at an equal gas flow rate to the first injector, thus with two injectors, the total air injection into the system is doubled.

Figures 8.7-8.9 present the drag reduction and volume fraction of air in the disperse and continuous phase along the full plate length, for the three different locations of the second air injector. In Figure 8.7, where the second injector is implemented at $X - X_{\mathrm{inj}} = 2$ m, it is seen how the drag reduction increases to roughly 90% and stays constant for the full plate length. This indicates that a continuous air layer has been formed, and the drag reduction is in the ALDR regime. This is also seen in the air volume fraction, as the continuous volume fraction increases to roughly $\alpha_{\text{airC}} = 0.9$ and the disperse volume fraction decreases.

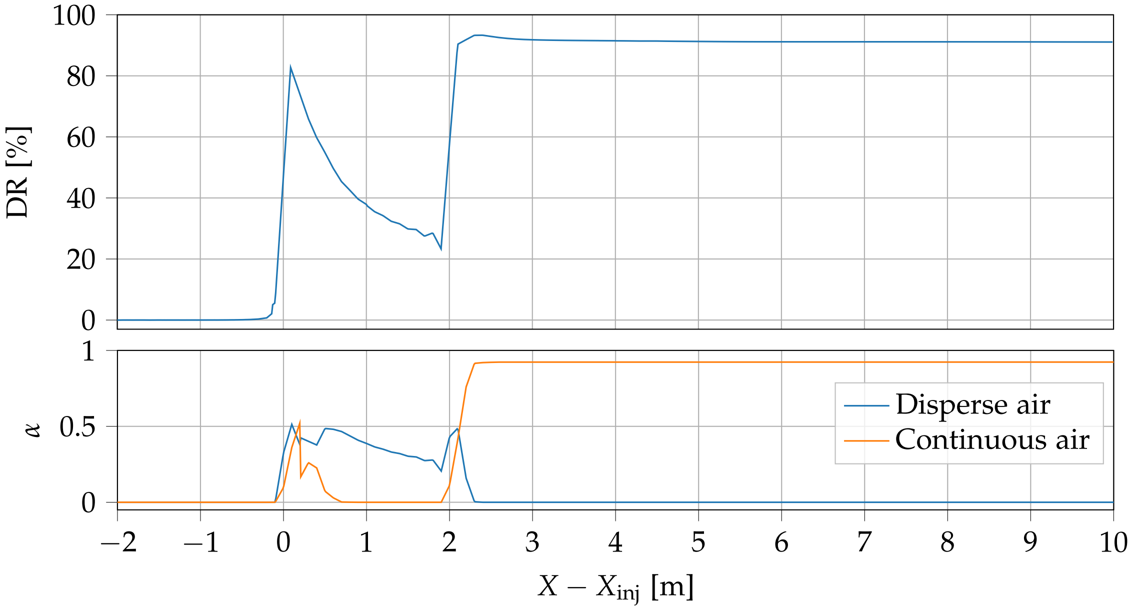

Figure 8.7: Drag reduction and air volume fraction versus downstream distance of the first injector location. A second air injector is implemented at $X - X_{\text{inj}} = 2\,\text{m}$.

Figures 8.8 and 8.9, where the second injector is implemented at $X - X_{\text{inj}} = 4\,\text{m}$ and $X - X_{\text{inj}} = 6\,\text{m}$, respectively, show very similar results as no continuous air layer forms after the second injector. This is also visible in the volume fraction graphs, where the continuous air volume fraction decreases rapidly after the second injector. This indicates, that the disperse air volume fraction has decreased sufficiently from the first injector, due to turbulence and dissipation, such that an additional injector at $X - X_{\text{inj}} = 4\,\text{m}$ and further downstream, will not transition the drag reduction to the ALDR regime. However, for both cases, the drag reduction is still increased after the second injector, as the overall disperse air volume fraction is increased. In general, this analysis shows, that a second injector should be implemented at roughly $X - X_{\text{inj}} = 2\,\text{m}$ to obtain a continuous air layer.

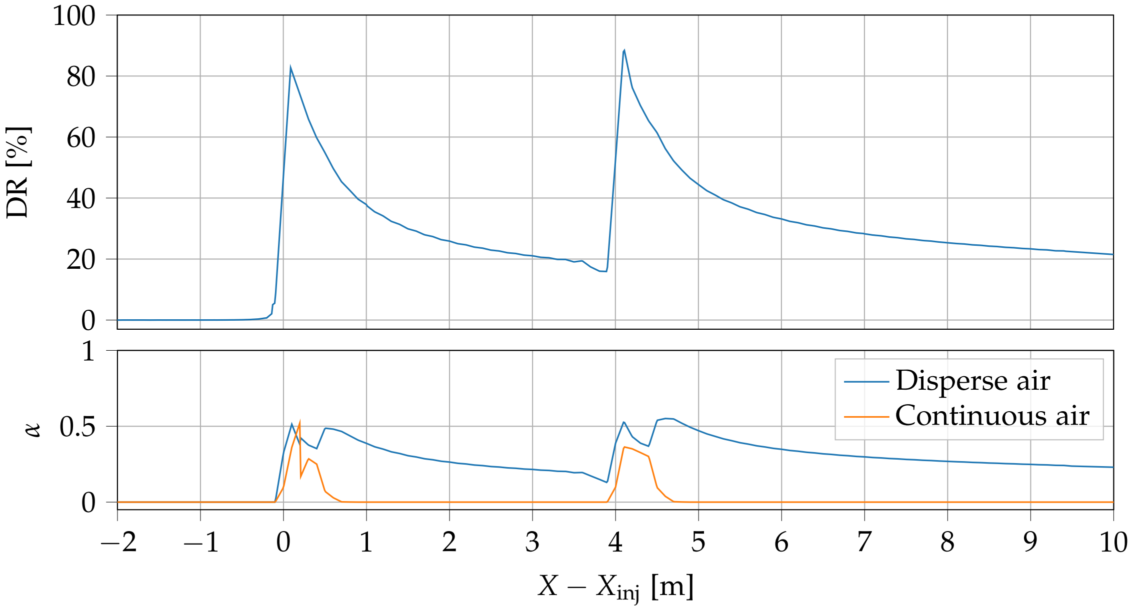

Figure 8.8: Drag reduction and air volume fraction versus downstream distance of the first injector location. A second air injector is implemented at $X - X_{\text{inj}} = 4\,\text{m}$.

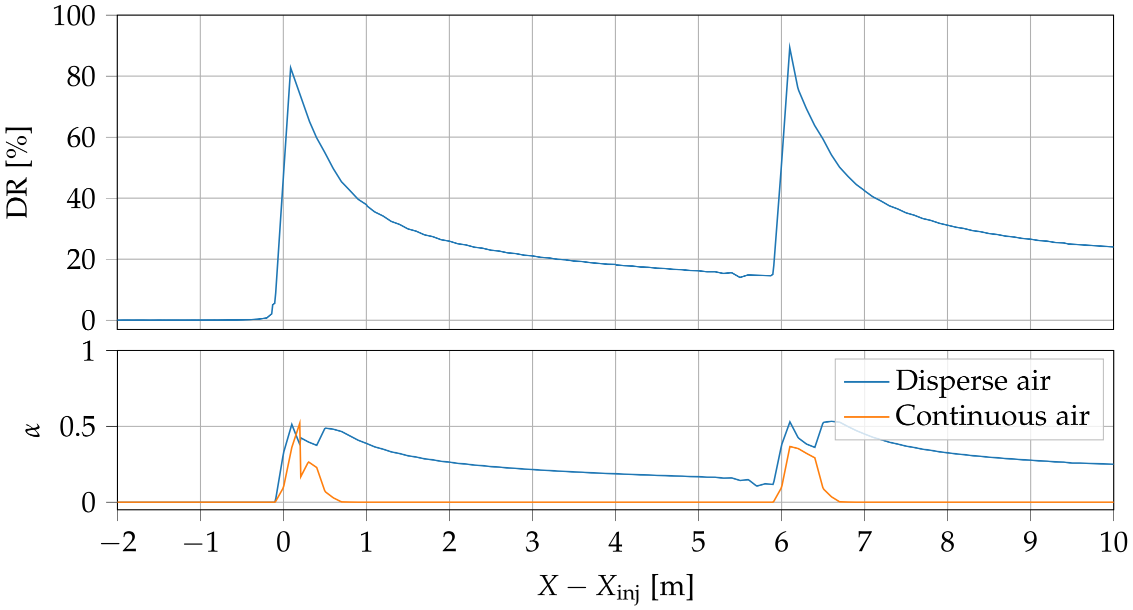

Figure 8.9: Drag reduction and air volume fraction versus downstream distance of the first injector location. A second air injector is implemented at $X - X_{\text{inj}} = 6\,\text{m}$.

9 Numerical Modelling of Air Lubrication with VOF LES

To further understand the bubbly flow in air lubrication applications and the potential shortcomings of the MultiMorph model, an additional analysis is done on the air injector geometry of Elbing et al. (2008). This is done by performing a VOF simulation using a LES turbulence model on a small part of the domain around the air injection point. The results of this simulation give an understanding of where the MultiMorph model differs from the real world in the case of bubble generation in air lubrication. Additionally, the results will illustrate the velocity field and turbulence in and around an air injector, to further understand air lubrication. To achieve accurate modelling, several modelling considerations are done. These and a description of the geometry are given in the following sections.

9.1 Geometry and Computational Domain

The geometry of the air injector domain is seen in Figure 9.1, with parameters listed in Table 9.1. The width of the computational domain in the z-direction, L_6, is not shown in the figure, but is also listed in the table. To set up the numerical model, boundary conditions are defined for each boundary, listed in Table A.6 in Appendix A.5. The boundaries defining the edges in the spanwise direction are defined as *front* and *back*.

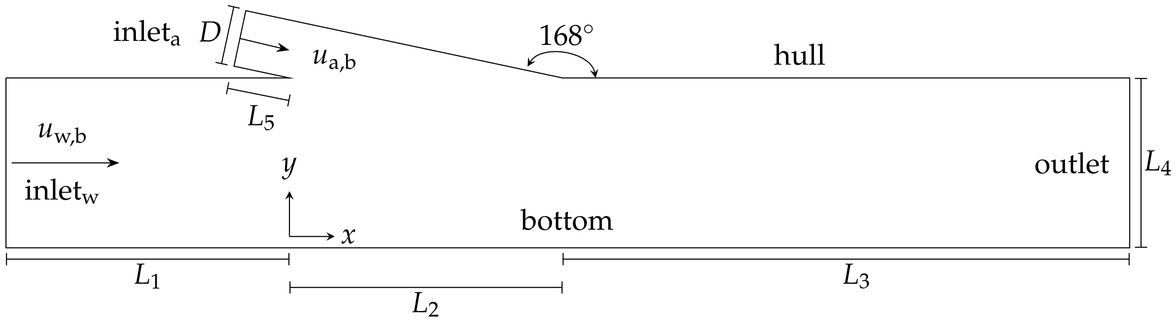

Figure 9.1: Geometry considered for the air injection analysis. Parameters are presented in Table 9.1.

Parameter	L_1/D	L_2/D	L_3/D	L_4/D	L_5/D	L_6/D	$u_{w,b}$	D
Value	5	4.82	10	1.5	1	0.5	6.7 m/s	5.75 mm

Table 9.1: Overview of the parameter set considered for this study.

The air injector has an angle of 12° to the water channel, to match the injector geometry of

Elbing et al. (2008). To greatly reduce computational time, only a periodic part of the domain is considered in the z-direction, and the width is defined as $L_6/D = 0.5$.

9.1.1 Two-Point Correlation for Determining Domain Width

The width of the domain is based on a two-point correlation at three different sample locations within the domain. The two-point correlation is based on the instantaneous velocity component in the x-direction, at three locations and two different instances.

The analysis showed that a domain width of $0.4D$ was sufficient to ensure no correlation between the two domain sides. However, to ensure that at no point in time any eddies larger than the domain will occur, a domain width of $0.5D$ is chosen. The computational technique and graphing of said two-point correlation can be seen in Appendix A.4.

9.2 Numerical Method

For the computational method, the VOF multiphase model is used to track the interface between the air and water. The interface is tracked by a function α. When $\alpha = 1$ a control volume is filled purely of water and $\alpha = 0$ denotes a control volume unoccupied by water. The interface between the two phases is present for $0 < \alpha < 1$.

$$\alpha = \begin{cases} 1 & \text{phase 1} \\ 0 & \text{phase 2} \\ 0 < \alpha < 1 & \text{interface} \end{cases} \tag{9.1}$$

When using the function α, only a single set of equations is necessary to calculate the properties of a given phase, as α can be used as a weight. In this way, the density and dynamic viscosity can be calculated as

$$\rho = \alpha\rho_\mathrm{w} + (1-\alpha)\rho_\mathrm{a} \tag{9.2}$$

$$\mu = \alpha\mu_\mathrm{w} + (1-\alpha)\mu_\mathrm{a}$$

where the subscripts “a” and “w” denote the air and water, respectively.

9.2.1 Governing Equations

The VOF model solves Navier-Stokes equations for two immiscible isothermal incompressible fluids, where the mass and momentum equation are given as

$$\frac{\partial\rho}{\partial t} + \nabla(\rho\boldsymbol{u}) = 0 \tag{9.3}$$

$$\frac{\partial(\rho \boldsymbol{u})}{\partial t} + \nabla(\rho \boldsymbol{u}\boldsymbol{u}) = -\nabla p + \nabla \boldsymbol{T} + \rho \boldsymbol{g} + \boldsymbol{F_\sigma} \tag{9.4}$$

where $\boldsymbol{T}$ is a stress tensor and $\boldsymbol{F_\sigma}$ describes the surface tension. An additional equation is necessary to describe the transport of the volume fraction α, the advection equation, which is given as

$$\frac{\partial \alpha}{\partial t} + \nabla(\alpha \boldsymbol{u}) = 0 \tag{9.5}$$

A challenging issue of the VOF model is the discretisation of the advection equation to achieve correct transport of α, especially in cells where the interface is present. High-order algebraic schemes tend to result in unstable numerical oscillations, while lower-order schemes will smear the surface (Gopala and van Wachem 2008). Another method is to employ a geometric scheme, which reconstructs the computational cells where the interface is present. The model used in this analysis employs the isoAdvector scheme by Roenby et al. (2016), where the interface cells are cut according to the isosurface that accurately represents the interface.

9.2.2 Dimensionless Parameters

Water enters the computational domain with the bulk velocity $u_{\mathrm{w,b}}$. The Reynolds number, Re_{x}, characterises the water flow

$$\mathrm{Re}_{\mathrm{x}} = \frac{\rho u_{\mathrm{w,b}} x}{\mu_{\mathrm{w}}} \tag{9.6}$$

with x indicating a point along the plate from the leading edge. The flow conditions are defined, such that a Reynolds number of $\mathrm{Re}_{\mathrm{x}} = 10^6$ is reached at the point of the air injector at $x = L_1$.

Air enters the air injector at a constant rate of $u_{\mathrm{w,b}}/u_{\mathrm{a,b}} = 0.1$, where $u_{\mathrm{w,b}}$ is the bulk inlet velocity of the water.

9.2.3 Computational Mesh

The computational mesh is presented in Figure 9.2. The mesh consists of roughly 33,500,000 computational cells where cells in the free stream after the injector have lengths in the order of 35 µm to 45 µm to resolve the smallest eddies and air bubbles sufficiently. At the hull, boundary cells are refined to achieve $y^+ < 1$ to adequately resolve the boundary layer, as is essential for LES. Table 9.2 shows a comprehensive list of mesh statistics, with the boundary layer cells shown in Figure 9.3.

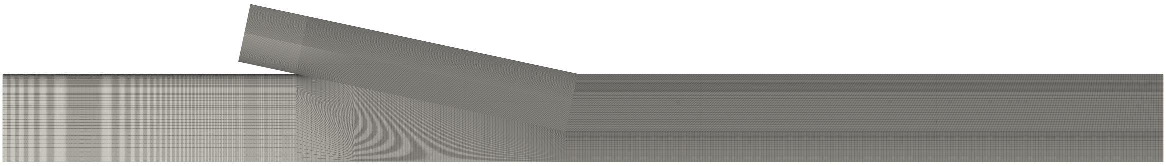

Figure 9.2: Meshing of the computational domain presented in Figure 9.1.

Figure 9.3: Close up of boundary layers of mesh shown in Figure 9.2.

Property	Value
# of cells	33,500,000
# of boundary layers	5
First layer thickness, $L_{\text{bl,first}}$	$1.3 \cdot 10^{-4} D$
Final layer thickness, $L_{\text{bl,last}}$	$0.0024D$
Tot. layer thickness, $L_{\text{bl,tot}}$	$0.0045D$
Max. skewness	0.54
Max. aspect ratio	61.5
Max. y^+	0.9
Average y^+	0.34

Table 9.2: Several properties for the injector geometry mesh. Sizes of layers are shown in Figure 9.3.

9.2.4 Boundary Conditions and Model Parameters

For the air injection, a fully developed velocity profile is applied at the boundary with bulk velocity $u_{\text{a,b}}$.

The Divergence Free Synthetic Eddie Method (DFSEM) model by Poletto et al. (2013) applies a turbulent velocity profile for the water inlet boundary condition, by generating synthetic eddies at the inlet. To generate the eddies, a k-ω SST URANS single-phase simulation is done to generate Reynolds stresses and turbulent length scale parameters to apply in the model domain.

The time step is dynamically adjusted to ensure a Courant-Friedrichs-Levy (CFL) number of $\text{Co} = u_{\text{w,b}} \Delta t / \Delta x < 0.8$, and a constant contact angle between the water and the hull is set as $\beta = 75^\circ$.

The simulations are done on AMD EPYC 7763 processors on 1792 processor cores.

9.2.5 Initialisation of Domain with URANS

The VOF LES domain is initialised to decrease computational time by a k-ω SST URANS VOF simulation in a quasi-steady state. In this way, the initial simulation time where the air injector is filling with air and a quasi-steady air layer is being formed downstream, is skipped. The URANS simulation is done for similar geometry and boundary conditions, although on a much coarser mesh of roughly 400,000 computational cells. To minimise all URANS effects, results of the LES simulation are only considered after some time equal to a single water flow pass-through of the domain.

9.2.6 Averaging of Results

As the water flow and air bubbles exert transient behaviour, the model's results will be averaged to achieve more representative results than instantaneous measurements. As mentioned, the first pass-through will not be considered due to the URANS initialisation. Averaging will therefore start after a settling period equal to one pass-through. The averaging will be done on the volume fraction, velocity and pressure fields, and the wall shear stress at the hull boundary downstream of the injector.

9.3 Results and Discussion

The following sections will present the results of the VOF LES model. Firstly an analysis is done on how the air bubbles are generated by the injector, and how the bubbles behave downstream. This is used to understand some of the potential phenomena not captured by the MultiMorph model. Afterwards, the velocity field and turbulence in the domain are presented and analysed to understand how the bubble generation occurs.

9.3.1 Air Bubble Generation in VOF LES Simulations

In Figure 9.4 the water volume fraction, α_{w}, is seen on a slice of the computational domain. The figure shows how bubbles form and travel downstream close to the hull as the air is injected into the water freestream. Larger bubbles of similar size can be seen for the full length of the domain, with smaller bubbles, which in some cases are not fully resolved, in between the larger bubbles.

A closer view of the air injector exit is seen in Figure 9.5 showing how the interface between the air and water becomes wavy, letting off large bubbles, with a bubble structure common to that seen in a slug multiphase flow regime. This wavy structure would likely not be seen in the MultiMorph model, as the large eddies are not captured due to the URANS approach.

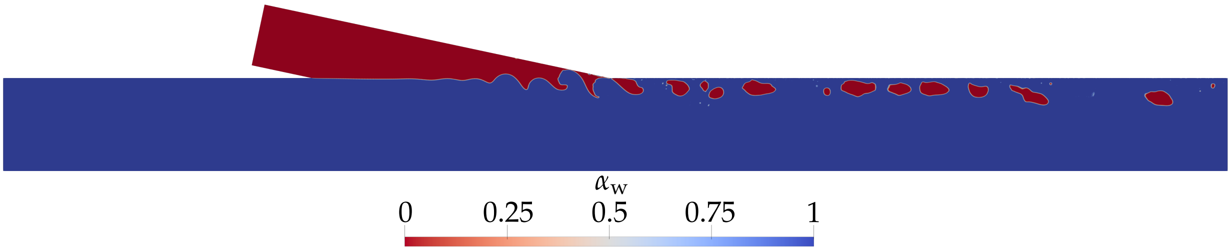

Figure 9.4: Sliced view of the instantaneous water volume fraction, α_w field. Click the image to view a GIF of the simulation.

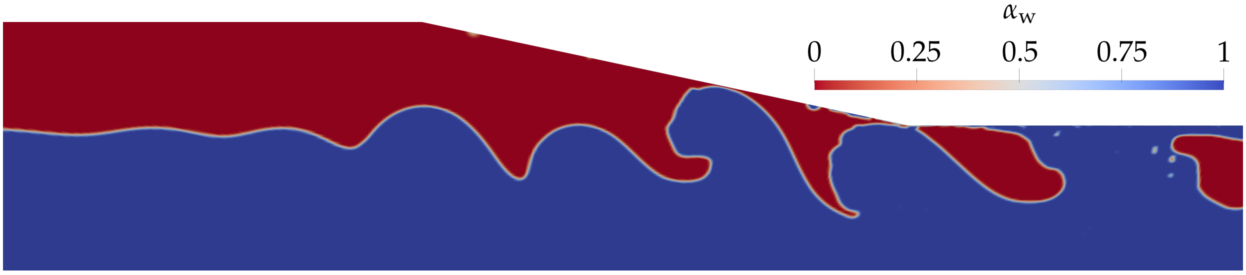

Figure 9.5: Sliced view of the instantaneous water volume fraction, α_w field around the exit of the air injector.

The large slug-like bubbles do however, not touch the wall above them, which can be seen in Figure 9.7, showing the surface of the wall after the air injector. These findings are similar to that of Sassi et al. (2020), who found that a thin liquid film is present between a gas slug and the near wall. This was also seen in Elbing et al. (2008), where a region of increased water volume fraction was seen between the wall and air bubbles, over a range of free-stream velocities and air injection rates.

Figure 9.6 presents the time-averaged water volume fraction in the near-wall domain at three locations downstream of the injector to quantify the water film between the wall and air bubbles. The figure shows a water film between the air slugs and the wall, with the water film thickness also increasing downstream. This was not seen in the results of the MultiMorph model, where the water volume fraction reached the lowest values immediately adjacent to the wall and increased continuously away from the wall, illustrated in Figure 8.1 and 8.3. This could result in an overshoot of drag reduction, as the near-wall air volume fraction is likely too high for the MultiMorph model.

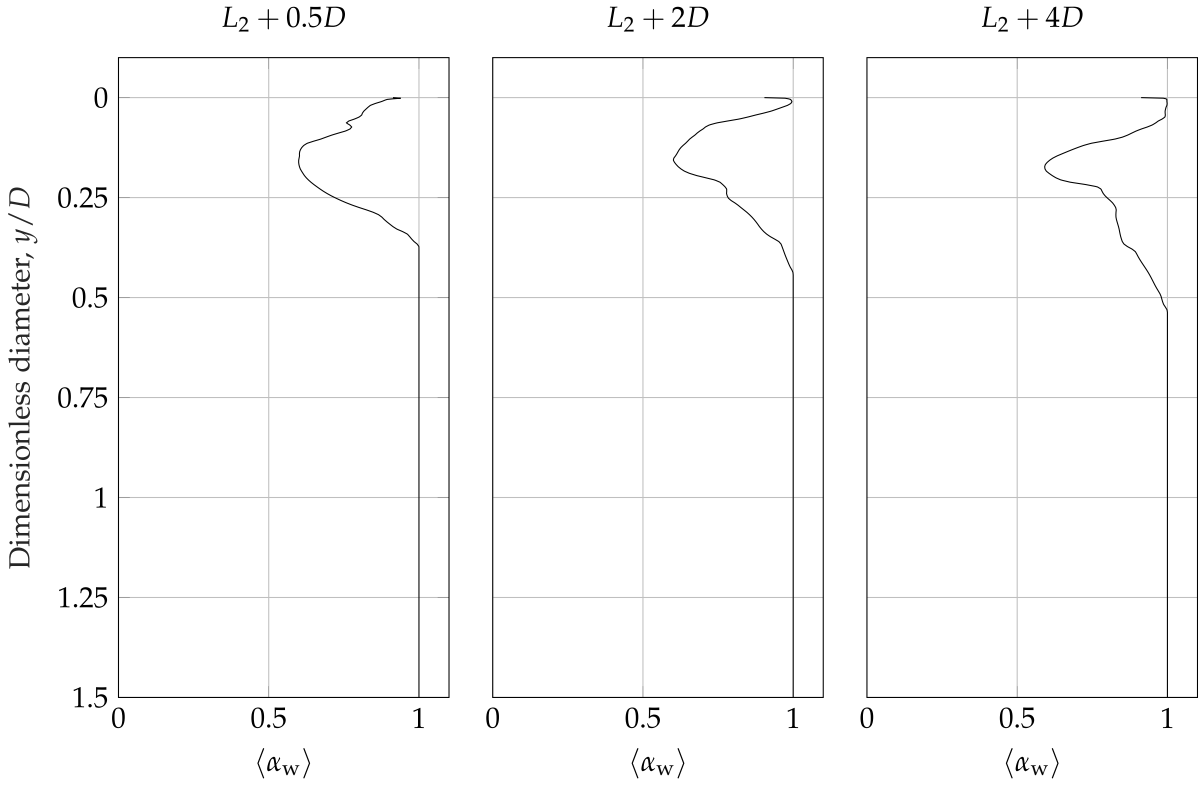

Figure 9.6: Time-averaged water volume fraction in the near-wall domain at $x/D = L_2 + 0.5D$, $x/D = L_2 + 2D$ and $x/D = L_2 + 4D$.

It is also observed in Figure 9.7 that a large number of small bubbles, which are not fully resolved, can be seen touching the surface. Elbing et al. (2008) also found that a large fraction of the total number of bubbles was in the range 50 µm to 150 µm, which supports the size of the near-wall bubbles seen in this analysis. A similar phenomenon was seen using the MultiMorph model in Section 8.1, where in the BDR regime, a disperse phase was observed for the full plate length, representing the presence of many small air bubbles.

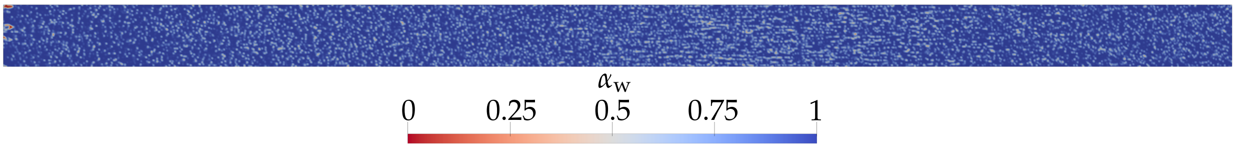

Figure 9.7: Surface view of the instantaneous α_w field on the wall after the air injector.

Further supporting that the multiphase flow is in the slug regime, is Figure 9.8, showing the $\alpha_a = 0.5$ isosurface. It is seen that most of the air bubbles are as wide as the domain, meaning that the air injector likely produces slugs as wide as the injector itself. The slugs generally produce air bubbles with a mean height, in the y-direction, of roughly 1 mm to 1.5 mm with a length-to-height ratio of approximately 2. Downstream of the air injector, the bubbles keep their shape, with negligible breakup.

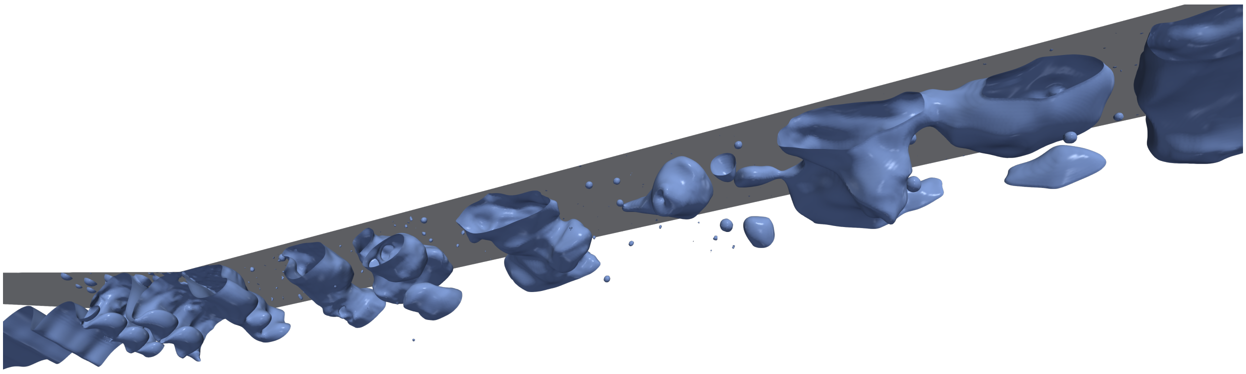

Figure 9.8: Isosurface for $\alpha_\mathrm{w} = 0.5$ just downstream of the air injector.

9.3.2 Velocity Analysis

Figure 9.9 presents the time-averaged streamwise velocity field in the domain. It is seen how an increased velocity occurs at the exit of the air injector, where the air bubbles are released into the free stream. Furthermore, it is observed that the boundary layer before the air injector is destroyed as the air collides with the water, essentially resetting and starting over again after the air injector.

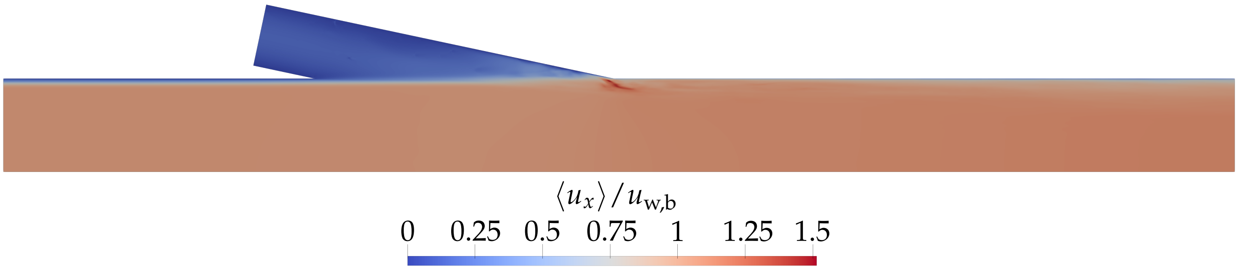

Figure 9.9: Time-averaged streamwise velocity field of the flow.

To further analyse the velocity field within the domain, the dimensionless time-averaged streamwise velocity, in the near-wall domain, at four locations is presented in Figure 9.10. The figure supports the observation that the turbulent velocity profile before the air injector is destroyed and the boundary layer starts over after the injector. The velocity gradient away from the wall is also much steeper after the injector when air bubbles are present in the boundary layer. Furthermore, it is seen how at $x/D = L_2 + 0.5D$ a velocity higher than the bulk velocity is seen just off the wall, which dissipates again further downstream.

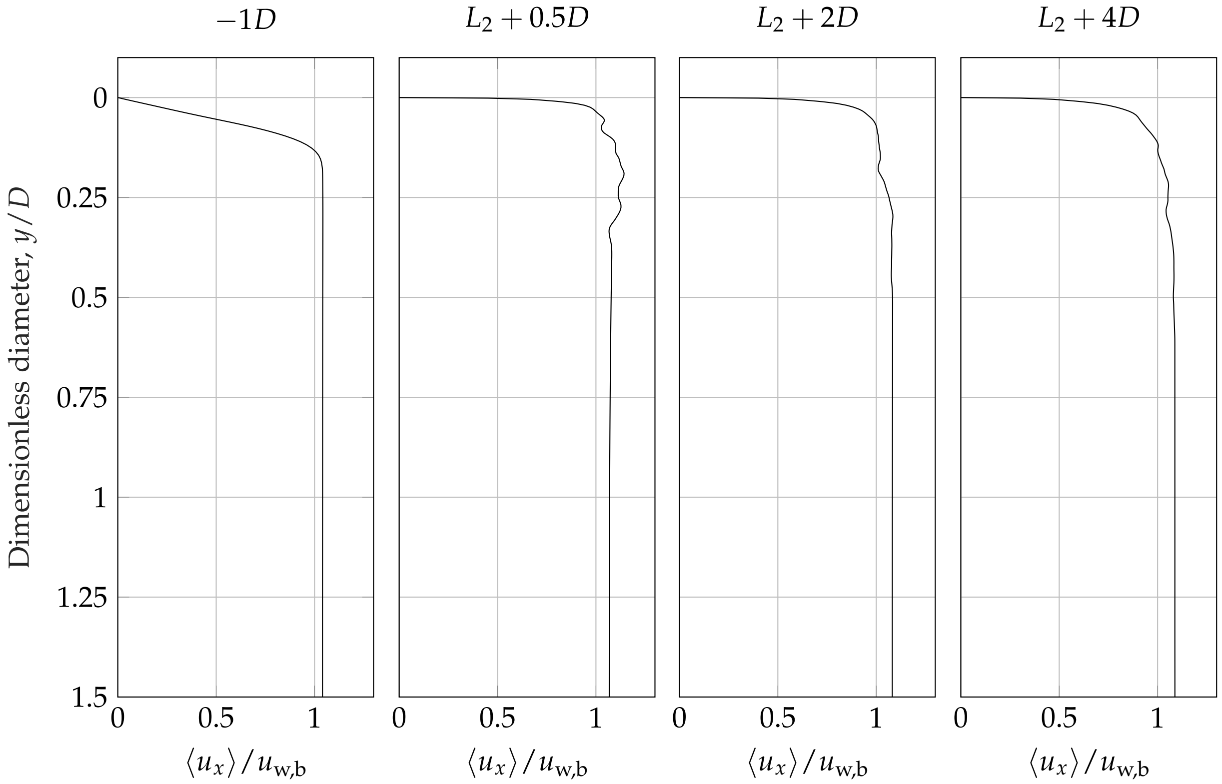

Figure 9.10: Time-averaged dimensionless streamwise velocity profiles at $x/D = -1D$, $x/D = L_2 + 0.5D$, $x/D = L_2 + 2D$ and $x/D = L_2 + 4D$.

9.3.3 Analysis of Turbulence in the Air Injector Domain

Based on the shredding of large slugs of air seen in Figure 9.5, the turbulence intensity at the air injector is shown in Figure 9.11. The turbulence intensity is calculated from the root-mean-square of the instantaneous velocity, representing the velocity fluctuations. The figure clearly illustrates, how the turbulence intensity reaches a peak value of $I \approx 1.3\%$ at the exit of the air injector, which likely causes the unstable nature and shredding of the air bubbles at this point. Additionally, the turbulence intensity takes values close to zero upstream at the air-water interface, explaining the steady interface before the injector exit.

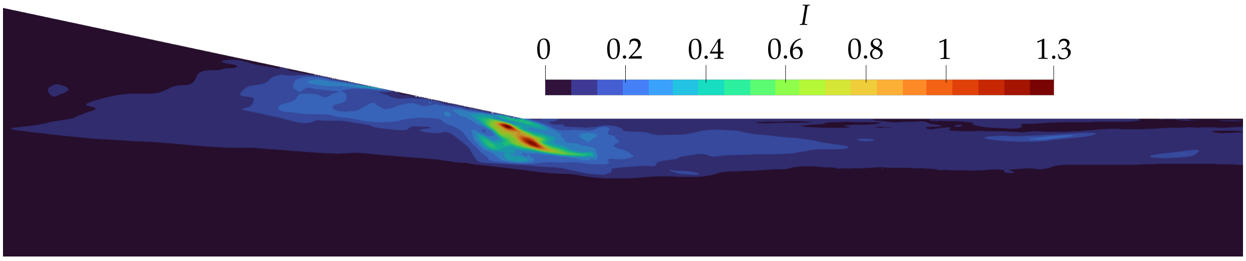

Figure 9.11: Turbulence intensity, in %, around the exit of the air injector.

To visualise and classify the three-dimensional flow structures in turbulent flow, the Q-criterion will be used. The Q-criterion is given in terms of the strain rate tensor and rotation rate tensor as

$$Q = \frac{1}{2}(||\boldsymbol{\Omega}||^2 - ||\boldsymbol{S}||^2) \tag{9.7}$$

where $\boldsymbol{\Omega}$ is the rotation rate tensor and $\boldsymbol{S}$ is the strain rate tensor (Chong et al. 1990). By thresholding Q to positive values, areas in the flowfield where the vorticity dominates are visualised, while negative Q values indicate viscous stress-dominated areas. Figure 9.12 shows the isosurface for $Q = 10$ to visualise the vortices in the flow field.

The figure clearly illustrates the function of the DFSEM model for implementing a turbulent velocity profile, as turbulence and several synthetic vortex structures are seen immediately downstream of the inlet.

Interestingly, the turbulence and vortices seem to reduce significantly at the start of the air injector, as the boundary layer is destroyed. However, downstream of the air injector, the boundary layer starts developing again as the boundary layer thickness increases significantly with downstream distance. The boundary layer downstream of the air injector also mainly consists of much smaller vortex structures, compared with the vortices before the injector. This could indicate that air bubbles greatly increase the turbulence in the flow field, and induce smaller vortices.

Figure 9.12: Isosurface of the Q-criterion, shown for a value of $Q = 10$. In this way, areas where the vorticity dominates, are shown.

10 Conclusion

This work presents an investigation into how the multifield two-fluid model MultiMorph, can be used to accurately model the dynamics of air injection beneath a flat plate to be used for analysis of air lubrication within the maritime industry.

To understand how the MultiMorph model operates, a thorough description of its framework is described, with how the model combines the Euler-Euler and the Volume of Fluid approaches. A sensitivity study is conducted on the model parameters, disperse phase bubble diameter and turbulence intensity to understand how these parameters affect air layer formation and dissipation. Furthermore, an analysis of the two different air injection methods, air slot injection and air mass source injection is done. The results of the sensitivity study shaped a model setup which was then validated against the experimental data by Elbing et al. (2008) for both air injection methods. The validation showed that the MultiMorph model was able to accurately predict the air lubrication drag reduction underneath a flat plate in a two-dimensional domain. Importantly, the validation was possible on a relatively coarse mesh, proving that the advantages of the MultiMorph model are also applicable to air lubrication applications.

Based on the validated MultiMorph model, further analysis of how the near-wall boundary layer develops is done to understand how air bubbles affect the boundary layer. In the BDR regime, it is found that the bubbles have a negligible effect on the boundary layer, with the bubbles slowly dissipating downstream of the injection point. However, when enough air is present to enter the ALDR regime, the air layer remains consistent along the plate, and slimmer boundary layer thickness is observed. Further study is done on how surface roughness affects drag reduction, where it is found that increased surface roughness decreases drag reduction, caused by an increase of turbulence, increasing air dissipation away from the wall.

An analysis was also done on how multiple air injectors would affect the air layer formation. Three investigations were done where an additional injector was implemented at 2 m, 4 m and 6 m downstream of the initial injector. The study showed that an additional injector, with an equal air injection rate, at $X - X_{\text{inj}} = 2\,\text{m}$, was able to form a continuous air layer in the ALDR regime, from the already existing bubbles which were in the BDR regime. However, for the additional injectors at $X - X_{\text{inj}} = 4\,\text{m}$ and $X - X_{\text{inj}} = 6\,\text{m}$, too many bubbles from the first injector have dissipated such that the additional bubble injections were not enough to form a continuous air layer. The study thereby suggests that some critical location of a second air injector exists where enough bubbles occur to form a continuous air layer in the ALDR regime.

An in-depth analysis of the air injector with VOF LES simulations showed, that the air bubbles are generated as slug-like structures with diameters of roughly 1 mm to 3 mm, with the defined flow conditions. Downstream of the injector, the bubbles mostly keep their shape, with negligible breakup. The analysis also showed that a region of increased water volume fraction occurs between the wall and the air bubbles, as was commonly found in the literature. This illustrated one of the MultiMorph shortcomings, as this phenomenon was not captured in the MultiMorph framework. Lastly, the air injector also disrupts the turbulence significantly, as the boundary layer is destroyed, before developing again downstream of the injector.

References

Adams, Thomas, Christopher Grant, and Heather Watson (Jan. 2012). "A Simple Algorithm to Relate Measured Surface Roughness to Equivalent Sand-grain Roughness". In: *International Journal of Mechanical Engineering and Mechatronics* 1. DOI: `10.11159/ijmem.2012.008`.

An, Hai, Haozhe Pan, and Po Yang (2022). "Research Progress of Air Lubrication Drag Reduction Technology for Ships". In: *Fluids* 7.10. ISSN: 2311-5521.

Brackbill, J.U, D.B Kothe, and C Zemach (1992). "A continuum method for modeling surface tension". In: *Journal of Computational Physics* 100.2, pp. 335–354. ISSN: 0021-9991. DOI: `https://doi.org/10.1016/0021-9991(92)90240-Y`.

Bragg, Andrew D. et al. (2021). "Assessment of the validity of a log-law for wall-bounded turbulent bubbly flows". In: *International Journal of Heat and Fluid Flow* 91, p. 108857. ISSN: 0142-727X. DOI: `https://doi.org/10.1016/j.ijheatfluidflow.2021.108857`.

Breuer, M., H.T. Baytekin, and E.A. Matida (2006). "Prediction of aerosol deposition in 90 degree bends using LES and an efficient Lagrangian tracking method". In: *Journal of Aerosol Science* 37.11, pp. 1407–1428. ISSN: 0021-8502. DOI: `https://doi.org/10.1016/j.jaerosci.2006.01.013`.

Burns, A. D. et al. (2004). "The Favre Averaged Drag Model for Turbulent Dispersion in Eulerian Multi-Phase Flows". In: *5th International Conference on Multiphase Flow*.

Ceccio, Steven L. (2010). "Friction Drag Reduction of External Flows with Bubble and Gas Injection". In: *Annual Review of Fluid Mechanics* 42.1, pp. 183–203. DOI: `10.1146/annurev-fluid-121108-145504`.

Chiroșcă, Ana and Liliana Rusu (Dec. 2021). "The Use of CFD Methods in the Shipbuilding Industry and their Benefits". In: Acta Universitatis Danubius, p. 2021.

Chong, M. S., A. E. Perry, and B. J. Cantwell (May 1990). "A general classification of three-dimensional flow fields". In: *Physics of Fluids A: Fluid Dynamics* 2.5, pp. 765–777. ISSN: 0899-8213. DOI: `10.1063/1.857730`.

Comminal, Raphaël and Jon Spangenberg (2021). "Three-dimensional cellwise conservative unsplit geometric VOF schemes". In: *Journal of Computational Physics* 442, p. 110479. ISSN: 0021-9991. DOI: `https://doi.org/10.1016/j.jcp.2021.110479`.

Crowe, C.T. et al. (2011). *Multiphase Flows with Droplets and Particles (2nd ed.)* CRC Press.

Dapelo, Davide, Federico Alberini, and John Bridgeman (2015). “Euler-Lagrange CFD modelling of unconfined gas mixing in anaerobic digestion”. In: *Water Research* 85, pp. 497–511. ISSN: 0043-1354. DOI: `https://doi.org/10.1016/j.watres.2015.08.042`.

Davidson, Lars (2022). *Fluid mechanics, turbulent flow and turbulence modeling*. Division of Fluid Dynamics, Department of Mechanics and Maritime Sciences, Chalmers University of Technology.

Edelbauer, W. (2017). “Numerical simulation of cavitating injector flow and liquid spray break-up by combination of Eulerian–Eulerian and Volume-of-Fluid methods”. In: *Computers & Fluids* 144, pp. 19–33. ISSN: 0045-7930. DOI: `https://doi.org/10.1016/j.compfluid.2016.11.019`.

Elbing, Brian R. et al. (2008). “Bubble-induced skin-friction drag reduction and the abrupt transition to air-layer drag reduction”. In: *Journal of Fluid Mechanics* 612, 201–236. DOI: `10.1017/S0022112008003029`.

Elbing, Brian R. et al. (2013). “On the scaling of air layer drag reduction”. In: *Journal of Fluid Mechanics* 717, 484–513. DOI: `10.1017/jfm.2012.588`.

Farzpourmachiani, A. et al. (2011). “Eulerian–Lagrangian 3-D simulations of unsteady two-phase gas–liquid flow in a rectangular column by considering bubble interactions”. In: *International Journal of Non-Linear Mechanics* 4.

Fenhann, Jørgen Villy (2017). “CO2 Emissions from International Shipping”. In: *UNEP DTU Partnership Working Paper Series* 4.

Fotopoulos, Andreas G. and Dionissios P. Margaris (2020). “Computational Analysis of Air Lubrication System for Commercial Shipping and Impacts on Fuel Consumption”. In: *Computation* 8.2. ISSN: 2079-3197.

Frederix, E.M.A. et al. (2018). “Reynolds-averaged modeling of turbulence damping near a large-scale interface in two-phase flow”. In: *Nuclear Engineering and Design* 333, pp. 122–130. ISSN: 0029-5493. DOI: `https://doi.org/10.1016/j.nucengdes.2018.04.010`.

Ghiji, Matt et al. (Dec. 2014). “CFD Modelling of Primary Atomisation of Diesel Spray”. In: DOI: `10.13140/2.1.3035.6488`.

Godderidge, Bernhard et al. (Feb. 2009). “An investigation of multiphase CFD modelling of a lateral sloshing tank”. In: *Computers & Fluids - COMPUT FLUIDS* 38, pp. 183–193. DOI: `10.1016/j.compfluid.2007.11.007`.

Gopala, Vinay R. and Berend G.M. van Wachem (2008). "Volume of fluid methods for immiscible-fluid and free-surface flows". In: *Chemical Engineering Journal* 141.1, pp. 204–221. ISSN: 1385-8947. DOI: `https://doi.org/10.1016/j.cej.2007.12.035`.

Haringa, Cees et al. (2016). "Euler-Lagrange computational fluid dynamics for (bio)reactor scale down: An analysis of organism lifelines". In: *Engineering in Life Sciences* 16.7, pp. 652–663. DOI: `https://doi.org/10.1002/elsc.201600061`. eprint: `https://analyticalsciencejournals.onlinelibrary.wiley.com/doi/pdf/10.1002/elsc.201600061`.

Hessenkemper, H. et al. (2021). "Lift force coefficient of ellipsoidal single bubbles in water". In: *International Journal of Multiphase Flow* 138, p. 103587. ISSN: 0301-9322. DOI: `https://doi.org/10.1016/j.ijmultiphaseflow.2021.103587`.

Hirt, C.W and B.D Nichols (1981). "Volume of fluid (VOF) method for the dynamics of free boundaries". In: *Journal of Computational Physics* 39.1, pp. 201–225. ISSN: 0021-9991. DOI: `https://doi.org/10.1016/0021-9991(81)90145-5`.

Hoang, C.L., Yasuyuki Toda, and Y. Sanada (Jan. 2009). "Full scale experiment for frictional resistance reduction using air lubrication method". In: *Proceedings of the International Offshore and Polar Engineering Conference*, pp. 812–817.

Hosokawa, Shigeo et al. (July 2002). "Lateral Migration of Single Bubbles Due to the Presence of Wall". In: Fluids Engineering Division Summer Meeting Volume 1: Fora, Parts A and B, pp. 855–860. DOI: `10.1115/FEDSM2002-31148`.

Hysing, S. et al. (Aug. 2009). "Quantitative benchmark computations of two-dimensional bubble dynamics". In: *International Journal for Numerical Methods in Fluids* 60, pp. 1259 –1288. DOI: `10.1002/fld.1934`.

Ishii, Mamoru and Novak Zuber (1979). "Drag coefficient and relative velocity in bubbly, droplet or particulate flows". In: *AIChE Journal* 25.5, pp. 843–855. DOI: `https://doi.org/10.1002/aic.690250513`. eprint: `https://aiche.onlinelibrary.wiley.com/doi/pdf/10.1002/aic.690250513`.

Johansson, Christopher (2014). "Optimization of wall parameters using CFD". MA thesis. KTH, Aerodynamics, p. 14.

Kartuzova, Olga and Mohammad Kassemi (July 2018). "Validation of a CFD Model Predicting the Effect of High Level Lateral Acceleration Sloshing on the Heat Transfer and Pressure Drop in a Small-Scale Tank in Normal Gravity". In: V003T18A002. DOI: `10.1115/FEDSM2018-83113`.

Kim, Young-Rong and Sverre Steen (2023). “Potential energy savings of air lubrication technology on merchant ships”. In: *International Journal of Naval Architecture and Ocean Engineering* 15, p. 100530. ISSN: 2092-6782. DOI: `https://doi.org/10.1016/j.ijnaoe.2023.100530`.

Krull, Benjamin et al. (2024). “A filtering approach for applying the two-fluid model to gas-liquid flows on high resolution grids”. In: *Chemical Engineering Science* 290, p. 119909. ISSN: 0009-2509. DOI: `https://doi.org/10.1016/j.ces.2024.119909`.

Lardeau, Sylvain, Michael Leschziner, and Tamer Zaki (Mar. 2012). “Large Eddy Simulation of Transitional Separated Flow over a Flat Plate and a Compressor Blade”. In: *Flow Turbulence and Combustion - FLOW TURBUL COMBUST* 88. DOI: `10.1007/s10494-011-9353-0`.

Levitsky, Semyon et al. (Jan. 2005). “Water Oxygenation in an Experimental Aerator with Different Air/Water Interaction Patterns”. In: *HAIT J. Sci. Eng. B* 2.

Lima Neto, Iran, Zhu David, and N. Rajaratnam (Apr. 2008). “Air Injection in Water with Different Nozzles”. In: *Journal of Environmental Engineering-asce - J ENVIRON ENG-ASCE* 134. DOI: `10.1061/(ASCE)0733-9372(2008)134:4(283)`.

Lipej, Andrej, Simon Muhic, and Duško Mitruševski (July 2017). “Wall Roughness Influence on the Efficiency Characteristics of Centrifugal Pump”. In: *Strojniški vestnik - Journal of Mechanical Engineering* 63. DOI: `10.5545/sv-jme.2017.4526`.

Liu, Yao et al. (Aug. 2022). “Numerical Simulation of Two-Phase Flow Using Eulerian-Eulerian Model With One-Group Interfacial Area Transport Equation”. In: DOI: `10.1115/ICONE29-93769`.

Lloyd, Thomas et al. (July 2017). “Computational fluid dynamics prediction of marine propeller cavitation including solution verification”. In.

Lucas, D., H.-M. Prasser, and A. Manera (2005). “Influence of the lift force on the stability of a bubble column”. In: *Chemical Engineering Science* 60.13, pp. 3609–3619. ISSN: 0009-2509. DOI: `https://doi.org/10.1016/j.ces.2005.02.032`.

Ma, Tian et al. (2017). “Direct numerical simulation–based Reynolds-averaged closure for bubble-induced turbulence”. In: *Phys. Rev. Fluids* 2 (3), p. 034301. DOI: `10.1103/PhysRevFluids.2.034301`.

Mangrulkar, C K, J D Abraham, and A S Dhoble (2019). “Numerical studies on the near wall y+ effect on heat and flow characteristics of the cross flow tube bank”. In: *Journal of Physics: Conference Series* 1240.1, p. 012110. DOI: `10.1088/1742-6596/1240/1/012110`.

Marié, J.L., E. Moursali, and S. Tran-Cong (1997). “Similarity law and turbulence intensity profiles in a bubbly boundary layer at low void fractions”. In: *International Journal of Multiphase*

Flow 23.2, pp. 227–247. ISSN: 0301-9322. DOI: `https://doi.org/10.1016/S0301-9322(96)00075-4`.

Mathur, A. et al. (2019). "A Hybrid Dispersed-Large Interface Solver for multi-scale two-phase flow modelling". In: *Nuclear Engineering and Design* 344, pp. 69–82. ISSN: 0029-5493. DOI: `https://doi.org/10.1016/j.nucengdes.2019.01.020`.

Meller, Richard, Fabian Schlegel, and Dirk Lucas (2021). "Basic verification of a numerical framework applied to a morphology adaptive multifield two-fluid model considering bubble motions". In: *International Journal for Numerical Methods in Fluids* 93.3, pp. 748–773. DOI: `https://doi.org/10.1002/fld.4907`.

Meller, Richard et al. (2023). "Momentum exchange modeling for coarsely resolved interfaces in a multifield two-fluid model". In: *International Journal for Numerical Methods in Fluids* 95.9, pp. 1521–1545. DOI: `https://doi.org/10.1002/fld.5215`.

Menter, Florian R, Martin Kuntz, Robin Langtry, et al. (2003). "Ten years of industrial experience with the SST turbulence model". In: *Turbulence, heat and mass transfer* 4.1.

Michaelides, Efstathios, Clayton T. Crowe, and John D. Schwarzkopf (2016). *Multiphase Flow Handbook*. 2nd ed. CRC Press. ISBN: 1498701000.

Mikielewicz, Dariusz (2003). "Hydrodynamics and heat transfer in bubbly flow in the turbulent boundary layer". In: *International Journal of Heat and Mass Transfer* 46.2, pp. 207–220. ISSN: 0017-9310. DOI: `https://doi.org/10.1016/S0017-9310(02)00287-9`.

Mikko, Manninen, Veikko Taivassalo, and Sirpa Kallio (Jan. 1996). "On the Mixture Model for Multiphase Flow". In: *VTT Publications* 288.

Mizokami, Shuji et al. (Jan. 2010). "Experimental study of air lubrication method and verification of effects on actual hull by means of sea trial". In: *Mitsubishi Heavy Industries Technical Review* 47, pp. 41–47.

Munson, B.R., A.P. Rothmayer, and T.H. Okiishi (2012). *Fundamentals of Fluid Mechanics, 7th Edition*. Blackwell handbooks in linguistics. Wiley. ISBN: 9781118214596.

Muttenthaler, Lukas and Bernhard Manhartsgruber (Apr. 2020). "Euler–Lagrange CFD simulation and experiments on accumulation and resuspension of particles in hydraulic reservoirs". In: *Journal of the Brazilian Society of Mechanical Sciences and Engineering* 42. DOI: `10.1007/s40430-020-02292-8`.

Mäkiharju, Simo A., Marc Perlin, and Steven L. Ceccio (2012). "On the energy economics of air lubrication drag reduction". In: *International Journal of Naval Architecture and Ocean Engineering* 4.4, pp. 412–422. ISSN: 2092-6782. DOI: `https://doi.org/10.2478/IJNAOE-2013-0107`.

Nations, United (2016). *The Paris Agreement.*

Nikuradse, J (1950). “Laws of Flow in Rough Pipes”. In.

Pađen, Ivan et al. (2021). “Numerical modeling of spray secondary atomization with the Euler-Eulerian multi-fluid approach”. In: *Computers & Fluids* 222, p. 104919. ISSN: 0045-7930. DOI: `https://doi.org/10.1016/j.compfluid.2021.104919`.

Pirozzoli, Sergio, Simone Di Giorgio, and Alessandro Iafrati (2019). “On algebraic TVD-VOF methods for tracking material interfaces”. In: *Computers & Fluids* 189, pp. 73–81. ISSN: 0045-7930. DOI: `https://doi.org/10.1016/j.compfluid.2019.05.013`.

Piña, Johan Sarache et al. (2022). “Air injection in vertical water column: Experimental test and numerical simulation using volume of fluid and two-fluid methods”. In: *Chemical Engineering Science* 255, p. 117665. ISSN: 0009-2509. DOI: `https://doi.org/10.1016/j.ces.2022.117665`.

Poletto, R., T. Craft, and A. Revell (2013). *A New Divergence Free Synthetic Eddy Method for the Reproduction of Inlet Flow Conditions for LES*. Flow Turbulence Combust.

Rider, William J. and Douglas B. Kothe (1998). “Reconstructing Volume Tracking”. In: *Journal of Computational Physics* 141.2, pp. 112–152. ISSN: 0021-9991. DOI: `https://doi.org/10.1006/jcph.1998.5906`.

Roenby, Johan, Henrik Bredmose, and Hrvjoe Jasak (2016). *A computational method for sharp interface advection*. R. Soc.

Sassi, Paolo et al. (2020). “Experimental Analysis of Gas–Liquid–Solid Three-Phase Flows in Horizontal Pipelines”. In: DOI: `10.1007/s10494-020-00141-1`.

Sattar, M.A., J. Naser, and G. Brooks (2013a). “Numerical Simulation of Slag Foaming in High Temperature Molten Metal with Population Balance Modeling”. In: *Procedia Engineering* 56. 5th BSME International Conference on Thermal Engineering, pp. 421–428. ISSN: 1877-7058. DOI: `https://doi.org/10.1016/j.proeng.2013.03.142`.

– (2013b). “Numerical simulation of two-phase flow with bubble break-up and coalescence coupled with population balance modeling”. In: *Chemical Engineering and Processing: Process Intensification* 70, pp. 66–76. ISSN: 0255-2701. DOI: `https://doi.org/10.1016/j.cep.2013.05.006`.

Schlegel, Fabian et al. (2023). “OpenFOAM-Hybrid: A Morphology Adaptive Multifield Two-Fluid Model”. In: *Nuclear Science and Engineering* 197.10, pp. 2620–2633. DOI: `10.1080/00295639.2022.2120316`.

Schlichting, H. (1979). *Boundary-layer Theory*. McGraw-Hill classic textbook reissue series. McGraw-Hill. ISBN: 9780070553347.

Seok, Jun and Jong-Chun Park (2020). “Numerical simulation of resistance performance according to surface roughness in container ships”. In: *International Journal of Naval Architecture and Ocean Engineering* 12, pp. 11–19. ISSN: 2092-6782. DOI: `https://doi.org/10.1016/j.ijnaoe.2019.05.003`.

Shin, Keun Woo and Poul Andersen (2019). “CFD Analysis of Ship Propeller Thrust Breakdown”. In.

Shonibare, Olabanji and Kent Wardle (July 2015). “Numerical Investigation of Vertical Plunging Jet Using a Hybrid Multifluid–VOF Multiphase CFD Solver”. In: *International Journal of Chemical Engineering* 2015, pp. 1–14. DOI: `10.1155/2015/925639`.

Siikonen, Timo et al. (Feb. 2019). “Consistently formulated eddy-viscosity coefficient for k - equation model”. In: *Journal of Turbulence* 19, pp. 1–36. DOI: `10.1080/14685248.2019.1567926`.

Solsvik, Jannike and Hugo A. Jakobsen (2015). “Single drop breakup experiments in stirred liquid–liquid tank”. In: *Chemical Engineering Science* 131, pp. 219–234. ISSN: 0009-2509. DOI: `https://doi.org/10.1016/j.ces.2015.03.059`.

Spalart, Philippe et al. (Jan. 1997). “Comments on the Feasibility of LES for Wings, and on a Hybrid RANS/LES Approach”. In.

Tekavčič, Matej, Richard Meller, and Fabian Schlegel (2021). “Validation of a morphology adaptive multi-field two-fluid model considering counter-current stratified flow with interfacial turbulence damping”. In: *Nuclear Engineering and Design* 379, p. 111223. ISSN: 0029-5493. DOI: `https://doi.org/10.1016/j.nucengdes.2021.111223`.

Boundary Layer Two-Phase Bubbly Flow Equation (Nov. 1998). Vol. Nuclear Engineering. ASME International Mechanical Engineering Congress and Exposition, pp. 23–29. DOI: `10.1115/IMECE1998-1130`.

UNCTAD (2023). *REVIEW OF MARITIME TRANSPORT 2023*.

Versteeg, Henk Kaarle and Weeratunge Malalasekera (2007). *An Introduction to Computational Fluid Dynamics: The Finite Volume Method*. Addison-Wesley-Longman, pp. I–X, 1–257. ISBN: 978-0-13-127498-3.

Visscher, J. Paul (1928). *Nature and extent of fouling of ships’ bottoms*. Washington G.P.O, 1928, p. 94.

Vreman, A.W. et al. (Jan. 2009). “Two- and Four-Way Coupled Euler–Lagrangian Large-Eddy Simulation of Turbulent Particle-Laden Channel Flow”. In: *Flow Turbulence and Combustion* 82, pp. 47–71. DOI: `10.1007/s10494-008-9173-z`.

Weber, Andreas and Hans-Jörg Bart (June 2017). "Flow Simulation in a 2D Bubble Column with the Euler-Lagrange and Euler-Euler Method". In: *The Open Chemical Engineering Journal* 12. DOI: `10.2174/1874123101812010001`.

Wei, Tie (2020). "Scaling of turbulent kinetic energy and dissipation in turbulent wall-bounded flows". In: *Phys. Rev. Fluids* 5 (9), p. 094602. DOI: `10.1103/PhysRevFluids.5.094602`.

Xiao, F., Y. Honma, and T. Kono (2005). "A simple algebraic interface capturing scheme using hyperbolic tangent function". In: *INTERNATIONAL JOURNAL FOR NUMERICAL METHODS IN FLUIDS* 48, pp. 1023–1040. DOI: `https://doi.org/10.1002/fld.975`.

Yan, Kai and Defu Che (2010). "A coupled model for simulation of the gas–liquid two-phase flow with complex flow patterns". In: *International Journal of Multiphase Flow* 36.4, pp. 333–348. ISSN: 0301-9322. DOI: `https://doi.org/10.1016/j.ijmultiphaseflow.2009.11.007`.

Yujie, Zhang et al. (2012). "Three-dimensional volume of fluid simulations on bubble formation and dynamics in bubble columns". In: *Chemical Engineering Science* 73, pp. 55–78. ISSN: 0009-2509. DOI: `https://doi.org/10.1016/j.ces.2012.01.012`.

Zhu, Yuhao et al. (Feb. 2023). "Numerical Study on Thermodynamic Coupling Characteristics of Fluid Sloshing in a Liquid Hydrogen Tank for Heavy-Duty Trucks". In: *Energies* 16, p. 1851. DOI: `10.3390/en16041851`.

Štrubelj, L. and I. Tiselj (2011). "Two-fluid model with interface sharpening". In: *International Journal for Numerical Methods in Engineering* 85.5, pp. 575–590. DOI: `https://doi.org/10.1002/nme.2978`. eprint: `https://onlinelibrary.wiley.com/doi/pdf/10.1002/nme.2978`.

A Appendix

A.1 Two-Dimensional Bubble Dynamics Using the MultiMorph Model

An example case used to showcase the MultiMorph model is based on a rising bubble study in a two-dimensional domain conducted by Hysing et al. (2009). The computational grid is for this case altered to adopt three different grid refinement levels as seen in Figure A.1. This method showcases how the MultiMorph model resolves the gas as either a continuous or dispersed phase, depending on the mesh refinement. Furthermore, the disintegration of continuous structures to disperse is illustrated. The simulation parameters are seen in Table A.1 with the initial gas bubble being purely in the continuous phase and with a surface tension of 24.5 N/m.

Initial Simulation Parameters	Liquid	Gas
Viscosity [kg/m s]	10	1
Density [m^3/kg]	1000	100
Gravity [m/s^2]	0.98	0.98
Droplet Parameters		
Diameter	$w/2$	
Center in x-direction	$w/2$	
Center in y-direction	$w/2$	
Mesh Parameters		
Level 0 cell length	$w/8$	
Level 1 cell length	$w/16$	
Level 2 cell length	$w/32$	

Table A.1: Simulation, droplet, and mesh parameters for rising bubble simulation.

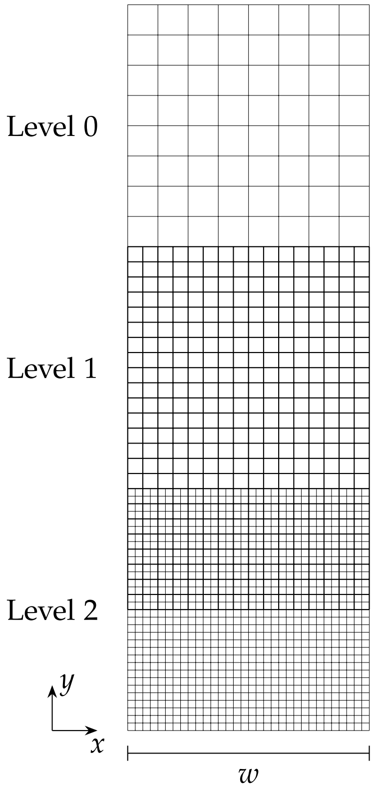

Figure A.1: Mesh for rising bubble simulation.

The alpha fields of the continuous and disperse phases are shown in Figures A.2 and A.3 respectively. The fields are shown at five different simulation times where $t^* = (t\ u_g)/r_0$, with t being the actual simulation time, r_0 is the initial bubble radius and $u_g = \sqrt{g 2 r_0}$ is the gravitational velocity as defined by Hysing et al. (2009).

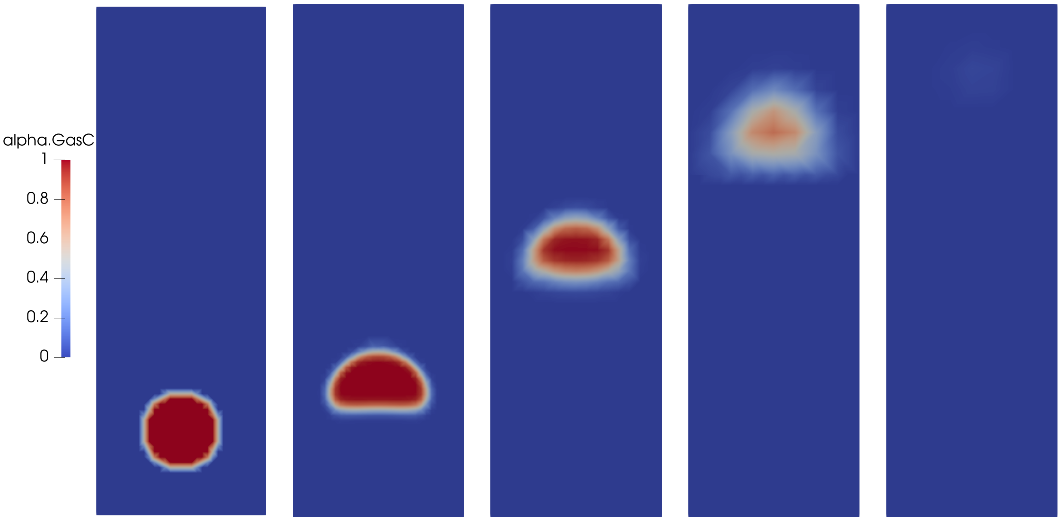

(a) $t^* = 0$ **(b)** $t^* = 4.2$ **(c)** $t^* = 14$ **(d)** $t^* = 22.4$ **(e)** $t^* = 28$

Figure A.2: Alpha fields of the continuous gas phase of a bubble rising through a computational domain with 3 different levels of refinement.

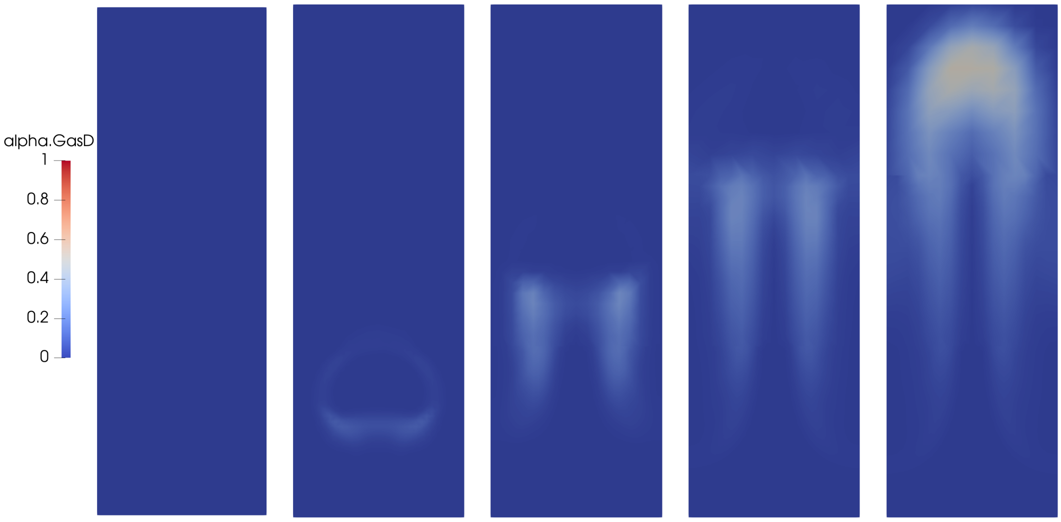

(a) $t^* = 0$ **(b)** $t^* = 4.2$ **(c)** $t^* = 14$ **(d)** $t^* = 22.4$ **(e)** $t^* = 28$

Figure A.3: Alpha fields of the dispersed air phase of a bubble rising through a computational domain with 3 different levels of refinement.

Figure A.2 shows how as the bubble rises through the different mesh refinement levels, the gas-liquid interface becomes more blurred. As the bubble hits refinement level 0, it stays in the continuous phase for a short time, before fully disintegrating to the disperse phase. Figure A.3 shows how as the bubble rises, part of the gas is left behind from the main bubble shape, as a trailing edge. For further analysis, a table presenting the volume fraction of each phase in the domain is shown in Table A.2.

Table A.2: Phase fractions in the domain of the rising bubble simulation.

Phase volume fractions	Liquid	GasC	GasD
$t^* = 0$	0.947	0.053	0
$t^* = 4.2$	0.944	0.053	0.003
$t^* = 14$	0.934	0.049	0.017
$t^* = 22.4$	0.923	0.043	0.034
$t^* = 28$	0.906	0.001	0.093

The phase fractions show the same tendency as the fields with the continuous gas transferring into the dispersed gas phase. However, it can also be seen that the liquid phase fraction decreases as the gas phase conversion occurs, meaning less water is in the domain at the end of the simulation compared to at the start. The loss of water indicates that a possible overcompensation is done by the MultiMorph model when the continuous to disperse air conversion takes place.

A.2 MultiMorph Numerical Settings

The boundary conditions, schemes and solver settings defined in the MultiMorph model are shown in the following Tables A.3, A.4 and A.5. The symbol “ * ” following a field indicates that these boundary conditions apply to all three morphologies. The boundary conditions are described using OpenFOAM lingo.

Table A.3: Boundary conditions set for each boundary in the model.

Field	Inlet	Outlet	Plate	Bottom
p	`calculated`	`calculated`	`calculated`	`calculated`
p_{rgh}	`fixedFluxPressure`	`fixedMean`	`fixedFluxPressure`	`fixedFluxPressure`
u_{w}	`fixedValue`	`inletOutlet`	`noSlip`	`slip`
u_{airC}	`fixedValue`	`inletOutlet`	`noSlip`	`slip`
u_{airD}	`fixedValue`	`inletOutlet`	`slip`	`slip`
α^*	`fixedValue`	`zeroGradient`	`zeroGradient`	`zeroGradient`
ω^*	`Turb. inlet`	`zeroGradient`	`Wall Function`	`zeroGradient`
k^*	`Turb. inlet`	`zeroGradient`	`Wall Function`	`zeroGradient`
nut*	`calculated`	`calculated`	`Wall Function`	`calculated`

Table A.4: Overview of the schemes set in the model.

Class	Name	Scheme
`ddtSchemes`	`default`	`Euler`
`gradSchemes`	`default`	`Gauss linear`
`divSchemes`	`div(phi,u)`	`Gauss linear`
	`div(phi,alpha)`	`Gauss vanLeer`
	`div(phir,alpha,alpha)`	`Gauss vanLeer`
	`div(alphaRhoPhi,u)`	`Gauss lim. Lin.V 1`
	`div(alphaRhoPhi, k|omega)`	`Gauss upwind`
	`div(((rho*nuEff)*dev2(T(grad(u)))))`	`Gauss linear`
`Lapl. Schemes`	`default`	`Gauss lin. uncorr.`

The `Euler`, `Gauss upwind` and `Gauss lin. uncorr.` schemes are first-order order accurate, while the remaining are second-order accurate.

Table A.5: Overview of the solvers used for the different fields, and their settings.

Fields	Solver	relTol	Tol	Preconditioner	Smoother
p_{rgh}	`GAMG`	0.01	e^{-6}	-	`DICGaussSeidel`
p_{rgh}Final	`PCG`	0	e^{-6}	-	`DICGaussSeidel`
k^*	`smoothSolver`	0	e^{-7}	-	`symGaussSeidel`
ω^*	`smoothSolver`	0	e^{-7}	-	`symGaussSeidel`

A.3 Experimental Setup for Validation

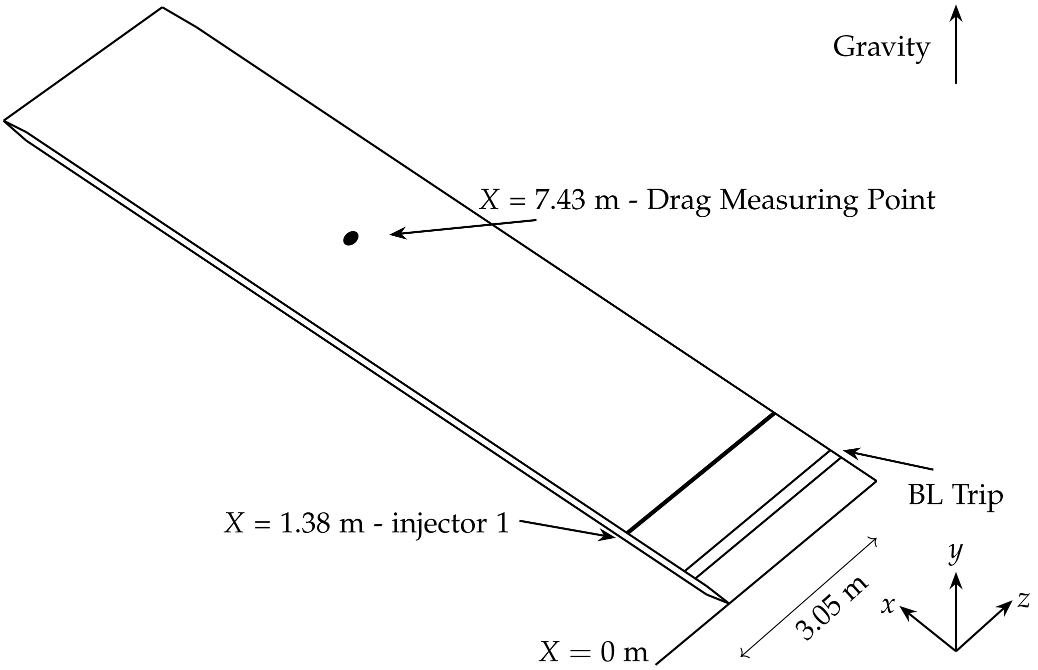

Figure A.4: Experimental setup used for Test 1a and 1b and Test 2a and 2b conducted by Elbing et al. (2008).

A.4 VOF LES Two-Point Correlation

To ensure that as few large eddies as possible cross the cyclic boundary conditions of the three-dimensional domain, the domain width will be based on the integral length scale. Davidson (2022) describes how a two-point correlation can use the instantaneous velocity component in the x-direction, u_1, in a domain to determine the integral length scale. A correlation between two points, A and C, while also being normalised using the root-mean-square of the velocity, $u_{1,\text{rms}} = (\overline{u_1'^2})^{1/2}$, can be computed as:

$$B_{11}^{\text{norm}}(x_1^A, \hat{x}_1) = \frac{\overline{u_1'(x_1^A)u_1'(x_1^A + \hat{x}_1)}}{u_{1,\text{rms}}(x_1^A)u_{1,\text{rms}}(x_1^A + \hat{x}_1))} \tag{A.1}$$

By taking the integral of equation A.1, the integral length scale, L_{int} can be found at the point where $B_{11}^{\text{norm}} = 0$, meaning no correlation beyond that length is observed,

$$L_{\text{int}} = \int_0^\infty B_{11}^{\text{norm}}(\hat{x}_1)\, \mathrm{d}\hat{x}_1 \tag{A.2}$$

The two-point correlation is computed at three different locations within the mesh to ensure that in no place in the domain eddies larger than the domain width exist. While not visualised, the correlation at the three locations is also examined at two different time steps to ensure that the two-point correlation is also accurate over time. Figure A.5 shows the two-point correlation of the three samples.

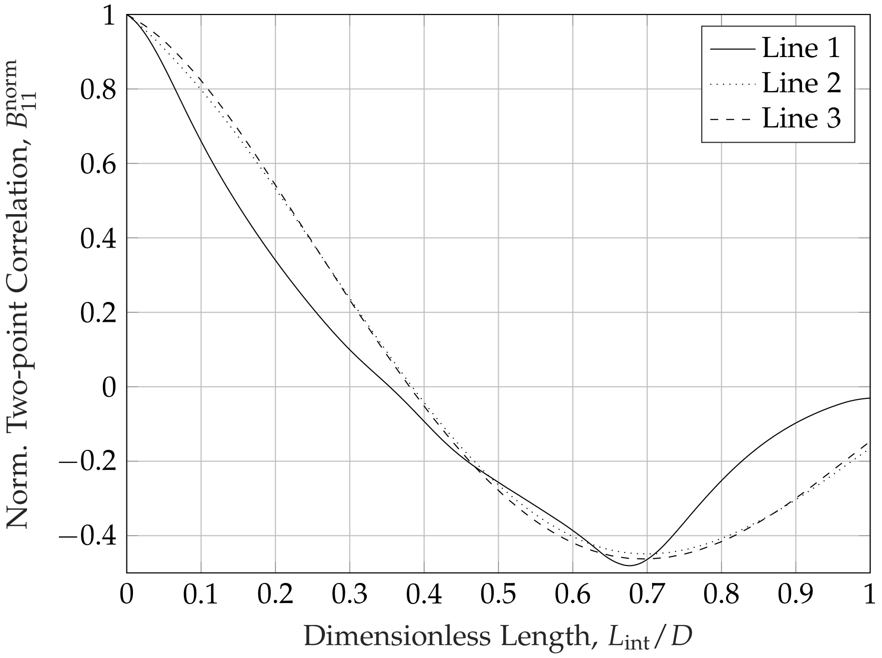

Figure A.5: Two-point correlation of the instantaneous velocity component in the x-direction. Line 1 refers to a sample taken just below the beginning of the air injection slot. Line 2 and line 3 refer to samples taken at the end of the air injector and $7D$ downstream of the air injector, respectively.

A.5 Boundary Conditions for VOF LES Model

The boundary conditions set for the VOF LES model to analyse the air injector are listed in Table A.6.

Table A.6: Boundary conditions set for each boundary in the VOF LES model.

Boundary	u	p_{rgh}	nut	α_{w}
inlet_{w}	`DFSEM`	`fixedFluxPressure`	`calculated`	`fixedValue`
inlet_{a}	`Fully dev. profile`	`fixedFluxPressure`	`calculated`	`fixedValue`
outlet	`inletOulet`	`totalPressure`	`calculated`	`inletOutlet`
hull	`noSlip`	`fixedFluxPressure`	`wallFunction`	`contactAngle`
bottom	`symmetry`	`symmetry`	`symmetry`	`symmetry`
front/back	`cyclic`	`cyclic`	`cyclic`	`cyclic`